X-RAY DIFFRACTION STUDIES OF DENSE FLUIDS

Thesis by

Wallace Irving Honeywell

In Partial Fulfillment of the Requirements

For the Degree of

Doctor of Philosophy

California Institute of Technology

Pasadena, California

1964

(Submitted May 21, 1964)

ACKNOWLEDGMENTS

I wish to express my appreciation to my research advisor, Dr. C. J. Pings, for his helpful guidance, personal interest, and continuous encouragement toward the completion of this work.

Special acknowledgment is due the many people who helped me during the research. The apparatus was constructed in part by Seichi ("Chic") Nakawatse, with many helpful suggestions by Willard M. Dewitt. Special thanks go to Dr. C. M. Knobler, without whose suggestions and assistance this research would have taken much longer to complete. Also, I wish gratefully to acknowledge the help of P. G. Mikolaj, who assisted in the laboratory measurements and contributed materially to the interpretation and reduction of the data.

During my graduate studies I have been the recipient of Institute scholarships, Teaching Assistantships, and fellowships from the Ford Foundation and the Woodrow Wilson Foundation. I wish to express my appreciation for these gifts.

Finally, I wish to thank my mother and father, mother- and father-in-law, and especially my wife, for their sacrifice and their encouragement. To them this thesis is dedicated.

ABSTRACT

Radial distribution functions supply useful information for the
investigation of the structure of liquids. An x-ray cryostat and
supporting equipment have been developed for determination of these
functions experimentally. The apparatus has been tested on confined
fluids at pressures up to 2000 psia and temperatures to 77° K. Al-
though a cylindrical beryllium sample cell is currently used in a
geometry of the Debye-Scherrer type, the equipment is adaptable
to parafocusing methods and to a wide variety of cell configurations.
Except for self-absorption in the sample and cell, absorption of the
incident and scattered x rays is less than 1%.

The cryostat and supporting equipment maintain automatic
temperature control to $\pm 0.006^{\circ}$ C. The sample temperature is
measured to $\pm 0.05^{\circ}$ C with a miniature platinum resistance element
placed directly in the sample fluid; temperature homogeniety of the
irradiated sample is better than 0.003° C.

The sample pressure is transmitted through a steel diaphragm
to an oil system where it is measured to 1:10,000 on a pressure
balance of the dead weight variety. A pressure transducer incor-
porating the diaphragm is used to balance the sample and oil pres-
sures. The transducer has a sensitivity of 3.27 volts per differential
psi.

The analysis of x-ray diffraction data from highly absorbing
samples is extended to include losses of incoherent scattering in the
sample and cell and in the detection system. Methods for treating

incident or scattered beams with nonuniform intensities are also presented. The scattering geometry represents an optimum choice for highly absorbing samples in cylindrical cells. The sample position is determined experimentally to within 0.001 in.

X-ray diffraction measurements made with molybdenum radiation are presented for liquid argon at -130.00° C for the densities 0.9098, 0.9818, and 1.0052 gm/cm^3. Scintillation detection was employed; monochromatization was effected with β filtering and pulse height selection. Radial distribution functions are derived from the intensity curves for data to $S = 9$ Å^{-1}. The coordination numbers and shell distances show good agreement with previous work at a nearby state, but suggest the possibility of systematic error in the older data.

TABLE OF CONTENTS

LIST OF TABLES

LIST OF FIGURES

NOMENCLATURE

A	cross sectional area
A_o	absolute value of the amplitude of a ray scattered from an isolated classical electron
$\mathring{A}$	Angstrom units
$A_{c,c}(S)$	cylindrical absorption factor for scattering and self-absorption in the cell
$A'_{c,c}(S)$	modified absorption factor for scattering and self-absorption in the cell
$ACC(S)$	composite beam absorption factor for scattering and self-absorption in the cell
$A_{c,sc}(S)$	cylindrical absorption factor for scattering in the cell and absorption in both the sample and the cell
$A'_{c,sc}(S)$	modified absorption factor for scattering in the cell and absorption in both the sample and the cell
$ACSC(S)$	composite beam absorption factor for scattering in the cell and absorption in both the sample and the cell
$A_{s,sc}(S)$	cylindrical absorption factor for scattering in the sample and absorption in both the sample and the cell
$A'_{s,sc}(S)$	modified absorption factor for scattering in the sample and absorption in both the sample and the cell
$ASSC(S)$	composite beam absorption factor for scattering in the sample and absorption in both the sample and the cell
b	constant coefficient in temperature interpolation equation
B	Breit-Dirac relativistic correction factor
C	normalization constant
d	differential operator
E	expected value of
E_s	potential of standard resistor

E_T	potential measured at temperature T
$f(S)$	atomic scattering factor
$f_d(S)$	atomic scattering factor corrected for dispersion effects
$\Delta f'$	real part of dispersion correction to atomic scattering factor
$\Delta f''$	imaginary part of dispersion correction to atomic scattering factor
$g(r)$	radial distribution function
$G(S)$	correction function for incoherent scattering
$i(S)$	intensity kernel for the Fourier transform
$I(S)$	theoretical intensity of scattered radiation, an extensive quantity
$I_s(S)$	unnormalized, experimentally determined intensity characteristic of a sample of volume V
$I^E(S)$	experimentally observed intensity
$I_0(S)$	"zero scattering" intensity
I^0	intensity of incident x-ray beam
I^0_{ref}	arbitrary reference intensity of incident beam
$K\alpha, K\beta$	α, β diffraction lines of K series
k	constant, characteristic of absorbing mecium
k_r	constant for r^{th} significance level
ℓ	optical path length
m_R	integer related to the radial cell dimension
MEAN	arithmetic mean
n	number of counts
N	number of atoms

$\underline{N}$ number of electrons

P   polarization factor

PAD   pulse amplitude distribution

r   radial coordinate

r_2/r_1 ratio of distances to first two peaks in distribution function

R   resistance

R_1, R_2, R_3 standard thermometer resistance at temperatures T_1, T_2, and T_3

S   scattering parameter, $\frac{4\pi}{\lambda}\sin\theta$

S_m upper limit of S in truncated Fourier integral

t   transmission factor

T   temperature

v   pulse voltage

$\bar{v}$ mean pulse voltage

V   irradiated volume

Var   variance of

W   half-height width of pulse amplitude distribution

x   dummy variable in probability integral

X_1, X_2 thermometer resistance measured at temperatures T_1, T_2

X_T interpolated resistance for thermometer at temperature T

z   atomic number

SUBSCRIPTS

a	atomic
abs	absolute
c	cell
c+s	cell plus sample
e	electronic
f	filter
j	referring to j^{th} beam strip
PHS	pulse height selector
s	sample
umbra	center section of incident beam

SUPERSCRIPTS

coh	coherent
inc	incoherent
i	incoming ray
o	outgoing ray

GREEK SYMBOLS

δ	fraction of scattered intensity consisting of coherently scattered radiation
Δ	increment
θ	half angle of diffraction
λ	radiation wavelength
μ	linear absorption coefficient
π	ratio circumference to diameter of circle = 3.14159...

SUBSCRIPTS

a	atomic
abs	absolute
c	cell
c+s	cell plus sample
e	electronic
f	filter
j	referring to j^{th} beam strip
PHS	pulse height selector
s	sample
umbra	center section of incident beam

SUPERSCRIPTS

coh	coherent
inc	incoherent
i	incoming ray
o	outgoing ray

GREEK SYMBOLS

δ	fraction of scattered intensity consisting of coherently scattered radiation
Δ	increment
θ	half angle of diffraction
λ	radiation wavelength
μ	linear absorption coefficient
π	ratio circumference to diameter of circle = 3.14159...

$\underline{N}$ number of electrons

P   polarization factor

PAD   pulse amplitude distribution

r   radial coordinate

r_2/r_1 ratio of distances to first two peaks in distribution function

R   resistance

R_1, R_2, R_3 standard thermometer resistance at temperatures T_1, T_2, and T_3

S   scattering parameter, $\frac{4\pi}{\lambda} \sin \theta$

S_m upper limit of S in truncated Fourier integral

t   transmission factor

T   temperature

v   pulse voltage

$\bar{v}$ mean pulse voltage

V   irradiated volume

Var   variance of

W   half-height width of pulse amplitude distribution

x   dummy variable in probability integral

X_1, X_2 thermometer resistance measured at temperatures T_1, T_2

X_T interpolated resistance for thermometer at temperature T

Z   atomic number

SUBSCRIPTS

a	atomic
abs	absolute
c	cell
c+s	cell plus sample
e	electronic
f	filter
j	referring to j^{th} beam strip
PHS	pulse height selector
s	sample
umbra	center section of incident beam

SUPERSCRIPTS

coh	coherent
inc	incoherent
i	incoming ray
o	outgoing ray

GREEK SYMBOLS

δ	fraction of scattered intensity consisting of coherently scattered radiation
Δ	increment
θ	half angle of diffraction
λ	radiation wavelength
μ	linear absorption coefficient
π	ratio circumference to diameter of circle = 3.14159...

Ω	ohms
$\rho(r)$	radial density
$\bar{\rho}$	average density
ρ_o	average electron density within an isolated atom
η	random variable representing number of counts
Σ	summation
τ	total counting time
ω	angular coordinate
χ	random variable representing the sample intensity

MISCELLANEOUS

#	wire gauge number
sin	sine of
cos	cosine of
∞	infinity
$^{\circ}K$	degrees Kelvin
$^{\circ}C$	degrees Centigrade
mm Hg	millimeters mercury
psig	pounds per square inch gauge
psia	pounds per square inch absolute
gm/cm^3	grams per cubic centimeter
$\int$	integral of
$\geq$	greater than or equal to
$\leq$	less than or equal to

$\simeq$	approximately equal to
$|\ |$	absolute value of
$\equiv$	is defined as
exp	exponential power with base e

I. INTRODUCTION

In comparison with the theoretical treatment of solids and gases, present theories describing the liquid state have met with only limited success. The prediction of physical properties from theoretical models is not in good agreement with the experimental data. Development of a successful theory has been inhibited by the lack of experimental data which give information about liquid structure at the molecular level. One experimental technique for obtaining such information is the diffraction of x rays with wavelengths comparable to molecular dimensions.

Debye[1] and Ehrenfest[2] were the first to show that the periodicity of a crystal structure is not required for the production of diffraction effects. Since that time (1915) much effort has been devoted to the interpretation of x-ray diffraction data from liquids. The bases for the modern theoretical treatment were laid in 1927 by Debye[3] and Zernike and Prins.[4] They related the diffraction pattern to a probability function for the distribution of intermolecular distances. Warren and Gingrich[5] furnished the most widely used modern expression of this theory. Several authors[6, 7, 8, 9] have since contributed to the refinement of this approach and to the treatment of the experimental data. The analysis of x-ray diffraction data from liquids is reviewed by Paalman and Pings.[10]

X rays which are incident upon a set of electrons cause the emission of secondary radiation from the electrons. A portion of the scattered rays of identical wavelength can interfere constructively

to produce diffraction effects. When the electrons are collected into atoms, specific restrictions are imposed on the phase relationships of the scattered wavelets. The interference effects which occur are directly related to the spatial distribution of electrons within the atoms. Such phenomena are manifest in the x-ray scattering from a rarified monatomic gas.

When a group of atoms crowds together, interaction becomes significant, and some degree of short range order is introduced. The result of this relatively fixed atomic distribution is an additional contribution to the interference effects. The diffraction patterns of monatomic liquids show varying degrees of this short range order, depending on their physical state. Studies of such simple substances provide the most useful information for the analysis of liquid structure. The spherical asymmetry of the more complex interactions in molecular systems introduces additional effects which encumber an already difficult subject.

The simplest probability function for describing liquid structure is the radial distribution function, $g_a(r)$. This function gives the distribution of pairs of atoms within the fluid. The number of atoms in a spherical shell of thickness dr at a distance r from any reference atom is given by $\bar{\rho}_a g_a(r) 4\pi r^2 dr$ where $\bar{\rho}_a$ is the average atomic density of the liquid. In other words, $g_a(r)$ is the radial atomic density normalized by $\bar{\rho}_a$. The introduction of this density into the basic diffraction equation for a group of electrons leads to an expression[10] for the scattered intensity:

to produce diffraction effects. When the electrons are collected into atoms, specific restrictions are imposed on the phase relationships of the scattered wavelets. The interference effects which occur are directly related to the spatial distribution of electrons within the atoms. Such phenomena are manifest in the x-ray scattering from a rarified monatomic gas.

When a group of atoms crowds together, interaction becomes significant, and some degree of short range order is introduced. The result of this relatively fixed atomic distribution is an additional contribution to the interference effects. The diffraction patterns of monatomic liquids show varying degrees of this short range order, depending on their physical state. Studies of such simple substances provide the most useful information for the analysis of liquid structure. The spherical asymmetry of the more complex interactions in molecular systems introduces additional effects which encumber an already difficult subject.

The simplest probability function for describing liquid structure is the radial distribution function, $g_a(r)$. This function gives the distribution of pairs of atoms within the fluid. The number of atoms in a spherical shell of thickness dr at a distance r from any reference atom is given by $\bar{\rho}_a g_a(r) 4\pi r^2 dr$ where $\bar{\rho}_a$ is the average atomic density of the liquid. In other words, $g_a(r)$ is the radial atomic density normalized by $\bar{\rho}_a$. The introduction of this density into the basic diffraction equation for a group of electrons leads to an expression[10] for the scattered intensity:

$$I^{coh}(S) = Nf^2(S)\left[1 + \int_0^{\infty} \bar{\rho}_a g_a(r) \frac{\sin Sr}{Sr} 4\pi r^2 \, dr\right] \qquad (1)$$

In this equation, $I^{coh}(S)$ is the time-averaged intensity of coherently scattered radiation* in the direction defined by the parameter $S = \frac{4\pi}{\lambda} \sin \theta$, where λ is the wavelength of the monochromatic radiation used, and θ is half the angle between the incident and scattered rays. N is the number of atoms present in the scattering volume, and f(S) is the atomic scattering factor; the latter is the sum of the amplitudes for rays scattered coherently by the electrons of any one atom. Equation (1) is strictly applicable only to a monatomic fluid composed of identical atoms; the scattering volume must also be large in comparison with interatomic distances.

Equation (1) may be rearranged into a form suitable for application of the Fourier integral theorem; the transform is

$$4\pi r^2 \bar{\rho}_a \left[g_a(r) - 1\right] = \frac{2r}{\pi} \int_0^{\infty} Si(S) \sin Sr \, dS \qquad (2)$$

where

$$i(S) = \frac{I^{coh}(S)}{Nf^2(S)} - 1$$

Evaluation of i(S) over a large range of S--in practice the measurements cannot extend to infinity--can thus lead directly to the radial

---

*Coherent radiation is often referred to as unmodified, Rayleigh, or "elastic" scattering; the wavelength of the diffracted radiation is identical to that of the incident radiation. The intensity, I(s), is that relative to the scattered intensity from an isolated classical electron under identical conditions.[11]

distribution function.

At large values of S the coherent diffracted intensity, $I^{coh}(S)$, oscillates with diminishing amplitude about $Nf^2(S)$, the scattering from N independent atoms. It is evident from equation (2) that precise measurements of $I^{coh}(S)$ are essential. The comparatively recent replacement of the photographic method by quantum detectors has improved the situation in this regard. Reviews of former studies and other new methods for reducing experimental difficulties are given by Furukawa[12] and Kruh.[13]

Previous apparatus has limited former investigations to relatively low pressures. The comprehensive testing of liquid theories is, however, dependent on the availability of data from a wide range of states. A sample cell was designed by Paalman and Pings[14] to extend the accessible pressure range. The present work was concerned with the development of apparatus and diffraction techniques compatible with this cell, and with the methods of data reduction specific to experiments with highly absorbing samples. An important objective was precise control of the thermodynamic conditions of the sample fluid; this permits access to the critical region and evaluation of the temperature and density derivatives of the radial distribution function. The present work employed only one type of cell at particular experimental conditions. However, the apparatus was designed to accommodate a wide variety of cells and to permit investigation of the liquid regions of several systems. For example, the cell designed by Rodriguez and Pings[15] is easily

interchangeable in the apparatus.

The apparatus and data reduction techniques were used to initiate a comprehensive program for the x-ray diffraction of liquid argon. Data at densities of 0.9098, 0.9818, and 1.0052 gm/cm^3 on the isotherm -130° C were obtained and processed. Argon was chosen over other simple liquids for several reasons. First, and most important, it is monatomic, and its liquid region is experimentally accessible. Further, high purity argon can be purchased at reasonable cost, and compressibility data is available over a wide range of temperatures and densities. This makes the duplication of the thermodynamic state an easy matter for other experimental investigations. Finally, it has already been the subject of a large number of experimental and theoretical investigations.

Throughout Chapters II - VI of this thesis, the experimental conditions and results of the argon investigations are used to demonstrate a specific application of the apparatus and data reduction techniques. The equipment and principles of data treatment may, however, be applied with general utility to x-ray diffraction experiments on dense fluids.

II. THE EXPERIMENTAL METHOD

A. General

The experimental method consisted of directing nearly parallel x rays onto the sample fluid and detecting and recording the diffracted radiation. For this experiment radiation from a molybdenum x-ray tube was diffracted from liquid argon confined in a cylindrical beryllium cell. A block diagram of the basic components is shown in Figure 1. A cryostat maintained the liquid at constant temperature and pressure. A scintillation counter detected the scattered radiation as a function of the scattering angle, 2θ. Electronic pulse height discrimination was used in conjunction with a $K\beta$ filter to effect monochromatization. A description of these electronic components and of the basis for their selection follows. The cell and cryostat will be discussed later.

In order to better approximate the conditions for Fourier inversion of the diffraction data, it is important to extend the range of the experimental measurements to large values of the scattering parameter $S = \frac{4\pi}{\lambda} \sin \theta$. The expression for S indicates that radiation of as short a wavelength as possible should be used. Of the x-ray tubes producing characteristic short wavelength radiation, silver ($\lambda = 0.56$ Å), molybdenum (0.71 Å), copper (1.54 Å), cobalt (1.79 Å) and iron (1.94 Å) are readily available.

A practical consideration in the selection of an x-ray tube is the inherently low scattering power of liquids. As a consequence, relatively long counting times are required to achieve high statistical

accuracy. One method for improving the situation is the use of high incident beam intensities. Although the silver radiation will give data to higher S values, the maximum output intensity of the commercial silver tube is relatively low. It was primarily for this reason that molybdenum radiation was chosen for this experiment. The higher output of the molybdenum tube permitted reasonable statistical accuracy with practical counting times. This was true in spite of the fact that molybdenum radiation was more highly absorbed in the sample and cell. Radiation of longer wavelengths (Cu, Co, and Fe) was dismissed from serious consideration because of its very high absorption in argon.

Additional factors influencing the choice of x-ray tubes were fluorescence and monochromatization. Fluorescence was not a serious problem because of the relatively high wavelengths of the characteristic emission lines for argon ($\lambda_{K\alpha}$ = 4.19 Å). This factor would have to be considered carefully for other samples. Monochromatization is discussed below.

The scattered x rays were detected with a scintillation counter. Quantum counters are preferable over film because of their superiority in evaluating relative intensities. Both the proportional counter and the scintillation counter maintain linear outputs up to very high counting rates (greater than 10^5 counts per second), and either could have been used for this experiment. However, the scintillation counter has a much higher counting efficiency and was chosen for this reason. Nearly 100% of all incident quanta between 0.3 and

2.0 Å are counted.[16]

After preamplification and linear amplification of the counter signal, the technique of pulse height discrimination was applied.[17] The signal from the scintillation counter was composed of pulses produced by x rays of many wavelengths. The pulse amplitudes are proportional to the energies of the x-ray quanta incident upon the counter. The function of the pulse height selector (often referred to as pulse height analyzer) was to attenuate pulses originating from x rays outside the narrow range of interest. In practice, some of the pulses from other x rays were transmitted. This was because pulse production in a quantum counter is a statistical phenomenon, and quanta of a single energy produce a distribution of pulses centered about that energy. The effectiveness of the pulse height selector was limited by the overlap of the distributions from the various wavelengths. In this respect, a scintillation counter is not as satisfactory for energy resolution as a proportional counter because of the former's broader pulse distributions. The effective monochromatization achieved with the scintillation counter, $K\beta$ filter, and pulse height selector is discussed in the next section.

As indicated in the diagram, the pulses from the pulse height selector were counted by the counter-timer. The output could be registered either as time accumulated for a fixed number of counts or counts in a fixed time; the fixed time strategy was used. At the end of each count an automatic step scanner advanced the counter to the next angle of observation. The accumulated counts were

printed on paper tape.

A listing of the electronic components associated with x-ray production and detection is provided in Appendix I.

2. Monochromatization

X-ray diffraction data are interpreted in terms of monochromatic radiation. In practice the experimentalist is not yet able to produce x radiation of a single wavelength. However, an x-ray tube operated at sufficiently high voltage produces several narrow bands of very intense x rays characteristic of the target element. In order to utilize the more intense Kα radiation band, other characteristic "lines" and the accompanying continuous spectrum must be attenuated. Several different methods which have been applied to x-ray diffraction experiments on liquids are reviewed by Furukawa.[16]

The method used in this experiment is similar to that used by Brady and Krause.[18] First, the intensity of the relatively strong Kβ line was reduced by approximately 99% with a sheet of 0.0038 in. zirconium foil placed before the scintillation counter. This Kβ filter diminished the Kα intensity to 35% of its original value.

Pulse height selection further monochromated the detected radiation. The pulse height selector was preset to admit only those pulses with an energy (voltage) band centered about the characteristic Kα energy. As previously noted, pulses other than those from Kα x rays were also counted. For this experiment, the pulse height selector admitted approximately 50% of the pulses from Kα radia-

tion. This was an arbitrary compromise between admitting a practical amount of the detected intensity and narrowing the band to include proportionately higher amounts of $K\alpha$ radiation.

The pulse height analyzer settings were established by first measuring the pulse amplitude distribution of the characteristic $K\alpha$ line. The intense powder diffraction lines from the beryllium sample cell were utilized for this purpose. The counter was set at the appropriate Bragg angle, and the evacuated cell was observed. An overwhelming portion of the radiation detected at this angle was confined to a very narrow band around the $K\alpha$ peaks. Window settings symmetrical about the mean voltage were then determined by trial and error; approximately 50% of the integrated intensity under the entire pulse amplitude distribution curve was admitted.

The radiation spectrum after monochromatization is illustrated in Figure 2. This spectrum was measured with a LiF analyzing crystal in place of the sample cell. For this reason it is only a qualitative representation of the spectrum observed from the cell and sample. However, a comparison of the integrated intensities from adjacent wavelength regions can be made with some confidence. A non-negligible contribution to the spectrum comes from the region of high wavelength near the $K\alpha$ line. The integrated intensity between 0.73 and 1.00 Å is about one-sixth as large as that between 0.69 and 0.73 Å. The quantitative effect of this degree of monochromatization has not yet been investigated.

III. DESCRIPTION OF APPARATUS

A. Cell Design

Sample confinement presents one of the major difficulties for the x-ray study of fluids at high pressures. Any closed container suitable for pressurizing fluids reduces the x-ray intensities by absorption in the cell walls. Since the scattering power of gases and liquids is inherently low, it is very important to minimize these absorption effects.

In addition to the absorption problem, corrections must be made for cell scattering. Any detectable scattering from the cell walls adds large amounts of undesirable background to the sample scattering. This difficulty was avoided by Gordon et al.[19] by providing that the incident and scattered x-ray beams intersect entirely within the sample. However, since the scattered x rays traversed large volumes of sample, this technique was limited to the study of samples with low absorption. Moreover, the relatively large diameter of their cell precluded studies at substantial pressure.

Minimizing the cell wall thickness reduces the effects of absorption--Beer's exponential law applies to x rays--and scattering--less scattering material is available. A cylinder provides the greatest strength to wall thickness ratio for any pressure vessel consistent with the geometry of the diffractometer.

A final consideration in cell design is that materials of low atomic number have low absorption. Thus, an optimal choice for a

cell design is a thin-walled capillary made from material of low atomic number and high tensile strength. The sample cell used in this experiment was a thin-walled cylinder made from sintered beryllium. It was designed by H. H. Paalman for his doctoral thesis under the supervision of C. J. Pings. Figures 3 and 4 show the cell. The inner diameter of the irradiated portion is 0.056 in. and the wall thickness 0.022 in. The cell shown in the photograph is the one used by Paalman; it is slightly smaller than the cell used in this experiment. The reader is referred to Pallman and Pings[14] for a more detailed description of the cell.

B. General Description of the Cryostat

The general design of the cryostat was dictated by the geometry of the cell, the geometry of the x-ray goniometer, and the selection of the sample systems to be studied. The cell was designed for use with the Norelco wide range goniometer. No attempt was made to alter the cell orientation from that employed by Paalman.[20]

The sample systems of immediate interest are simple liquids. The liquid regions of argon, nitrogen, oxygen, methane, zenon, krypton, and carbon monoxide are accessible at temperatures from 77° to 300° K and pressures up to 100 atmospheres. The cryostat was designed to maintain these conditions for long periods of time and to allow accurate measurements of the sample temperature and pressure.

Just as in cell design, the low scattering power of liquids

was an important consideration in cryostat design. Along with the requirements for temperature stability, this factor suggested the use of vacuum for thermal insulation. Not only is vacuum insulation the most desirable from the standpoint of heat transfer, it also provides the least absorption for the scattered x rays. An attendant bonus is the elimination of undesirable scattering from gases which would otherwise be present between the scattering sample and the detection system.

The beryllium sample cell was placed in the middle of a vacuum chamber which almost filled the volume between the x-ray source and the detector. A schematic illustration of the cell arrangement is shown in Figure 5. The cell was positioned horizontally; its axis was concentric with the cylindrical vacuum jacket. X rays were incident upon the cell normal to its axis. The detector scanned the cell about the angle 2θ. A thin Mylar window on the vacuum jacket transmitted the x rays in the plane defined by the x-ray source, the cell, and the detector.

On both sides of the x-ray scattering plane the cell was imbedded in a large block of brass maintained at the desired control temperature. The brass was cooled by cryogenic fluids passing through tubes around it and thermostated with the use of heaters imbedded near the tubes. The entire system was suspended in the vacuum jacket by supports of low thermal conductivity. A wooden cradle supported the vacuum jacket adjacent to the goniometer on the x-ray table.

High pressure tubing connected the sample in the cell to a pressure manifold on top of the vacuum jacket. There the sample pressure was transmitted via a steel diaphragm to a hydraulic oil system. A transducer indicated pressure equilibrium across the diaphragm. The pressure was measured by a pressure balance in an adjacent area of the laboratory.

An illustration of the cryostat and the surrounding experimental area is given in Figure 6. The large vessel in front of the x-ray generator is the coolant supply Dewar. The coolant transfer tube leads from the Dewar to the vacuum chamber. The transparent Mylar window is visible just inside the detector, and the goniometer can be seen in the background. An ion vacuum pump sits surrounded by its magnet on the near side of the vacuum jacket. The shiny circular object on top of the vacuum jacket is the housing for the pressure transmitting diaphragm. The capillary line leading away from the housing is the oil line to the pressure balance. The cryostat and diffractometer are described in detail below.

C. The Cyrostat

For descriptive purposes the cryostat may be conveniently divided into four parts: the vacuum chamber, the cell holder assembly, the temperature control annulus, and the sample filling and pressurization system. In the description which follows reference will be made to Figure 7, which gives a cross-sectional view of the vacuum chamber and cell holder assembly. Incident x rays are

normal to the plane of the drawing.

1. The Vacuum Chamber

The sample cell, H, was supported in the center of a hollow, cylindrical vacuum chamber, C. The chamber was made from brass tubing, 6-1/2 in. i. d., with a 1/4 in. wall. The flat end plate nearest the goniometer was silver soldered in place. The hub on the end of the goniometer shaft, G, was faced normal to the shaft axis. This face was used as an alignment surface against the end plate; after alignment the hub was bolted snugly to the chamber. The alignment procedure is described in Appendix II.

The other end of the vacuum chamber was closed with the flat end plate, T. This plate was removable to permit access to the cell assembly. Six bolts around the periphery clamp the plate against a neoprene O-ring to effect the vacuum seal.

During operation the chamber was evacuated through port B. The mounting flange for a Varian Associates VacIon pump, Type 911-5000, was silver soldered to the plate at this point. The pump current provided a continuous reading of the chamber vacuum at R. Two other ports, Q and one not shown, were available for rough pumping on the system.

All electrical leads were taken out of the vacuum chamber through a tube at port U to a multipin cap seal. The cap seal consisted of 24 copper rods, 1/16 in. in diameter, which were cemented with epoxy adhesive into tight-fitting holes in a 1/4 in. lucite plate.

The plate was then sealed to the tube with a neoprene O-ring. A styrofoam cover thermally insulated the outside of the multipin cap. Without insulation small drafts in the laboratory caused temperature gradients in the pin seals and subsequent instabilities in temperature measurement and control.

In order to permit passage of the incident and scattered x rays, a groove, 7/16 in. wide, was cut in the vacuum chamber. This groove extended 280 degrees around the periphery and was covered with a thin Mylar film window, A. A compression ring, B, sealed the window against a neoprene O-ring. This window acted as an effective vacuum seal while permitting very high transmission of the incident and scattered x rays. With the seal at liquid nitrogen temperatures, a Mylar window 0.00025 in. thick held a vacuum of 5×10^{-7} mm Hg (the VacIon pumping speed was 15 liters per second). At this pressure the Mylar stretched slightly into a smooth concave surface. This quarter-mil film reduced the x-ray intensity by less than 0.1% per layer with Cu Kα x rays. Thin beryllium windows with absorption of 22% and higher have been used on previous cyrostats.[21, 22] Recently Stochl and Ullman report success with a 0.002 in. Mylar window on a small cyrostat.[23] Norelco has used Mylar windows supported with nylon strands.[24]

Mylar film is slightly porous to most gases. When small leaks developed in other parts of the cyrostat, it was necessary to use a heavier window to maintain adequate vacuum. Half-mil Mylar was used during the later experimental runs. At pressures of 10^{-4}

to 10^{-5} mm Hg the window temperature dropped below the dew point in the laboratory. Whenever water vapor condensed on the window, the system vacuum failed. In order to remedy the situation the window was bathed with a stream of dry air. This procedure was not necessary when operating at the same temperatures with a quarter-mil window at the higher vacuum.

2. The Cell Holder Assembly

The beryllium sample cell, H, was held firmly in place in a cylindrical brass rod, I, one inch in diameter. This cell holder is a self-contained unit interchangeable in the apparatus. Any cell such as the one by Rodriguez and Pings[15] may be used in its place. A groove, 7/16 in. wide, was cut in this cell holder to allow passage of the x rays to and from the exposed portion of the cell. The cell was in good thermal contact with the brass on each side of the x-ray gap. At low temperatures the cell holder contracted slightly more than the cell and provided a tight mechanical fit; silicone grease aided thermal contact. An aluminized Mylar heat shield, F, reduced radiation heat transfer to the exposed portion of the cell. The quarter-mil film strip was wrapped around a recess in the cell holder and held in place with a pair of split rings. Although it reduced thermal radiation considerably, the aluminized Mylar transmitted x rays almost as well as the clear Mylar window discussed earlier. With the heat shield in place temperature gradients along the cell were caused chiefly by end effects.

The closure nut, P, and a Kel-F gasket were incorporated in

a Bridgman unsupported area pressure seal[25] on the open end of the sample cell. The nut and its extension contained the electrical leads and seals for the platinum resistance thermometer, N. This miniature resistance element was used to measure the sample temperature adjacent to the x-ray beam; the thermometer is described in IV. A. The thermometer leads were attached to two ceramic-insulated standoffs soldered into the walls of the closure nut extension. Figure 8 illustrates the thermometer and closure nut. The miniature standoffs are the pipe plug type (Type PP-MCA 6226) made by Fusite Corporation; they are rated at 20,000 psi. With careful soldering they provided excellent low temperature, high vacuum seals when the sample fluid was at high pressure.

Two #40 silk-covered copper leads were attached to the outside of each standoff. One pair provided the thermometer current, and the other pair was used to measure the potential across the thermometer. The copper leads were wrapped several times around the outside of the closure nut extension and insulated with cigarette paper and General Electric 7031 insulating varnish. Before passing out of the vacuum jacket the wires were similarly anchored to the inlet coolant tubes.

Figure 9 shows the wiring diagram for the thermometer circuit. The thermometer potential, E_T, was measured at the points where the copper leads were attached to the standoffs (the resistance of the standoffs was negligible in comparison with that of the element). The current loop included an Exide six-volt battery in

series with the thermometer, a 6,000-ohm dropping resistor, and a 10-ohm standard resistor. The one-milliamp current through the thermometer was sufficiently small to make Joule heating negligible. The current was calculated from the known resistance of the standard resistor and the potential measured across it. All potentials were measured with a Wenner microvolt potentiometer in conjunction with a Leeds & Northrup No. 2284 Galvanometer and an N.B.S. certified, unsaturated, Eppeley cadmium standard cell. Two double-pole double-throw switches were ganged together to reverse the potentiometer and thermometer currents simultaneously. Averaging the potentials for the forward and reverse currents compensated for any stray potentials in the circuits.

3.   The Temperature Control Annulus

The cell holder, I, Figure 7, was positioned by a slip fit into the brass temperature control annulus, J. A small set screw, O, fixed the cell holder so that the x-ray gaps in the two pieces were aligned. The function of the temperature control annulus was to damp out any rapid fluctuations in the temperature control conditions before they reached the cell holder and cell.

Two 1/4 in. lucite plates, M, were bolted to the annulus to support it in the vacuum chamber. Each plate contacted the chamber in only three places to reduce heat transfer to the annulus. These "feet," one inch wide and equally spaced, were lapped to the bore of the vacuum chamber to provide a close, sliding fit. Longitudinal alignment of the cell assembly was performed by positioning the

"feet" against a step in the chamber bore. Holes in the center of each lucite plate permitted easy removal of the cell holder from the temperature control annulus; the presence of the holes essentially eliminated conductive heat transfer through the ends of the cell holder. Highly polished heat shields, D and S, were attached to the lucite plates to reduce radiant heat transfer.

The annulus was cooled by liquid or gaseous nitrogen passing through two sets of 1/8 in. copper tubes, L, soldered around it. These tubes were installed to give countercurrent cooling, thereby reducing longitudinal temperature gradients. The tubes joined into common inlet and outlet lines before passing out of the vacuum jacket through the front end plate. Teflon spacers in thin-walled stainless steel tubing provided thermal standoffs for the inlet and outlet lines. The standoffs and the coolant transfer tube were designed from suggestions by Scott.[26] Powdered styrofoam was packed between the teflon spacers to inhibit ice formation. The thin-walled tubing was vacuum sealed to the front end plate with Veeco fittings employing neoprene O-rings.

Fine temperature control was accomplished with heaters, K, installed just inside the cooling coils. The #30 manganin wire heaters were wound on and cemented to the inner portion of the annulus; that section was then pressed into the shell containing the cooling tubes. The heaters on each side of the x-ray gap were operated independently to maintain control over the longitudinal temperature gradients. The signals from the two thermocouples, E, (24 gauge copper-Constantan

wires) were fed into external circuits which controlled the heaters automatically.

The heater control circuits are depicted schematically in Figure 10. The heater circuit on the left hand side of the x-ray gap (the larger side of the annulus) was controlled by an "absolute" thermocouple. The reference junction for this thermocouple was kept at room temperature. The junction was placed in the thermo-couple well of a copper block two inches in diameter and three inches long; a few drops of oil in the well assured good thermal contact. The copper block was then immersed in a Dewar of water; a large cork sealed the Dewar. The room temperature reference junction was used in preference to an ice bath junction because long term stability was preferred over temperature accuracy. Since the average temperature of the laboratory was maintained constant by an air conditioning system, no long term temperature drift occurred. The copper block and Dewar system were sufficient to protect the junction from any short term temperature fluctuations.

An adjustable D. C. reference voltage, which corresponded to the desired control temperature, opposed the thermocouple poten-tial. The difference actuated the control system. The signal was first amplified by a Leeds & Northrup stabilized D. C Microvolt Amplifier and displayed on an L & N Speedomax G Recorder. A retransmitting slidewire in the recorder then furnished a variable current input to the controller, an L & N Current Adjusting Type (C. A. T.) Control Unit. This unit contained proportional, differential,

and integral control features for loads of widely varying response characteristics. The output current was amplified by a magnetic amplifier and transmitted to the heater element.

The smaller side of the annulus was controlled by a differential thermocouple with junctions on each side of the x-ray gap. In this way, control of the small heater could be set to maintain a constant temperature difference between the two sensing points. Optimum control settings are discussed in Chapter IV. A. 5.

The combined sensitivity of the microvolt amplifier and recorder could be varied from four millivolts to five microvolts full scale on the retransmitting slidewire. The five-microvolt range permitted a control band as narrow as ± 0.01 microvolts; this would correspond to control of about 0.001° C for copper-Constantan thermocouples at -130° C. However, electrical noise in the thermocouple circuit limited the control to ± 0.02° C.

A more sensitive method of temperature control was used in the later experimental runs. In this control mode the platinum resistance thermometer in the sample was used as a control element. The potential measured across the element was substituted for the absolute thermocouple signal in the control circuit. The thermometer's larger voltage coefficient, dE/dT, and lower noise permitted temperature control to ± 0.006° C at -130°C. In addition, substitution of the Wenner potentiometer for the reference voltage permitted continuous display of the absolute sample temperature on the recorder. Even better temperature control could be achieved by placing a

second resistance element in the temperature control annulus in place of the absolute thermocouple junction. With the resistance element here the response time would be shortened considerably, and the controller would be able to operate more effectively.

4. The Sample Filling and Pressurization System

The sample fluid was loaded into the cell through a section of stainless steel capillary tubing. The low temperature end of this high pressure tubing (0.025 in. i.d., 0.042 in. o.d.) was silver soldered into the closure nut extension, P, Figure 7. The tubing was spiralled to extend the heat path, and the other end was sealed with a high pressure fitting into the pressure manifold. The sample was loaded into the manifold through port V; a high pressure valve (not shown) then sealed this inlet. A similar port and valve (not shown) were used to evacuate the cell prior to filling.

An intensifier, Z, was used to make small changes in the sample pressure during an experimental run. The intensifier rod could displace sample volume sufficient to alter the pressure ± 3 psi (0.06 psi per turn) at 40 atm sample pressure. Although the intensifier was operated manually, automatic pressure control could be adapted using the pressure transducer described below.

Sample pressure was transmitted through a flexible stainless steel diaphragm, Y, to a hydraulic oil system. An electronic detector, X, indicated the diaphragm position.

The cross-sectional drawing, Figure 11, shows some of the details of the pressure manifold assembly. The intensifier rod, L,

was soldered to the drive handle, K. The high pressure seal on the
intensifier was made with a tapered Teflon gasket, J; two bronze
followers, M, inhibited extrusion. The nut, N, compressed the
gasket and also contained the screw thread for driving the intensifier.
A safety cap, O, limited the intensifier travel. This intensifier
design is an adaptation of one used by Paalman.[20]

The pressure transmitting diaphragm, H, was a flat steel
disc, 2-3/4 in. in diameter by 0.005 in. thick, cut from stainless
steel Type 304 sheet stock. It was Heliarc-welded to the backing
plate, D, of the same type steel. The surface of the backing plate
was slightly concave to permit diaphragm movement. An identical
surface on the body of the pressure manifold, E, protected the
diaphragm from overpressure; maximum diaphragm travel between
the two backing plates was 0.010 inches. The lead gasket, C, sealed
the backing plate assembly with the compressive action of eight
machine screws on the two gasket followers. The screws were held
firmly in the nut, F, which employed a buttress thread. This sealing
technique is an adaptation of a design by Reamer and Sage.[27] Their
diaphragm and backing plate, however, were machined from a single
piece of stock. Butcher and Alsop also incorporated a diaphragm in
their pressure transducer.[28] Welding the diaphragm onto the back-
ing plate reduces the difficulty and expense of the diaphragm design
by Reamer and Sage and avoids the complicated sealing techniques
used by Butcher and Alsop. During welding, a large copper block
was placed in the center of the diaphragm to draw the heat away.

Without this block the diaphragm warped slightly. With some

practice the welder produced diaphragms which were leak tight and

visually flat.

The diaphragm position was detected by the distance detector,

A. It was sealed into the holder, B, with an annealed copper gasket.

Washers, C, were used as spacers to position the detector at the

desired distance from the diaphragm. The detector holder was

chromium plated to prevent galling of the close-fitting surfaces.

The distance detector was the Type H-3-022 model made by

the Bently Nevada Corporation. Figure 12 shows a schematic of the

detector circuit. A fifteen-volt D. C. supply energized the distance

detector electronics, Model D-152 Distance Detector System. A

high frequency alternating current through the coil in the detector

sensing head created a varying magnetic field which intersected the

steel diaphragm. Eddy currents induced in the diaphragm imposed

variable loads on the field as a function of the diaphragm position.

The rectified output signal was of the order of volts. This technique

afforded a direct method for determining the diaphragm position; it

contained no moving parts or duplicate capacitative networks used

in previous arrangements.[27, 29]

A voltage divider was used to reduce the signal to the order of

millivolts for display on a Speedomax recorder. With the 0 - 10 milli-

volt range of the recorder the smallest observable voltage change

corresponded to a differential change in pressure of 0.01 psi across

the diaphragm. This sensitivity was adequate for the present investi-

gations. Methods for achieving higher sensitivities are discussed in Appendix III.

For pressure control a constant pressure was established on the oil side of the diaphragm. The gas sample pressure was then varied until the pressures were balanced. The schematic diagram of Figure 13 indicates the components associated with pressure control. High pressure tubing connected the diaphragm oil system with the pressure balance, pressure bench, and Heise bourdon gauges. Figure 14 shows the experimental area for pressure control. The large wheel seen in the foreground of the photograph is part of the injector used to increase the oil pressure while loading the system to operating pressure. The Heise gauges were employed to monitor the pressure during loading. During an experimental run the pressure balance (seen behind the pressure bench) remained connected to the oil system, thereby providing the known reference pressure against which the sample pressure was balanced. As mentioned above, the diaphragm pressure transducer indicated the null position.

The pressure balance was the dead weight type developed by Michels.[30] It was manufactured by the Hart Engineering Company. The principle of operation is based on the equalization of the oil pressure on a differential piston with the force from calibrated weights suspended from the piston. The rope and pulley system seen in Figure 14 rotated the piston to reduce frictional effects. The absolute pressure on the sample was obtained by adding the hydrostatic pressures from the oil and gas heads to atmospheric pressure

and the pressure balance reading. The balance possessed an accuracy of one part in 10,000 and sensitivity and reproducibility of one part in 20,000. Above 200 psig the pressure transducer sensitivity exceeded that of the pressure balance.

D. The Diffractometer

1. The Goniometer

A Norelco wide-range goniometer was used to position the scintillation counter accurately with respect to the cell. This goniometer has a scanning range of $-30^{\circ} \leq 2\theta \leq 160^{\circ}$. The angle of observation was known to $\pm 0.003^{\circ}$ in 2θ. The goniometer was positioned with a target anode-to-sample distance of 6.98 inches and a sample-to-counter (receiving slit) distance of 5.63 inches. The takeoff angle of 5.8° from the horizontal was used for maximum incident beam intensity.

2. Beam Collimation

Highly collimated incident and scattered radiation was required for this experiment. The strong diffraction peaks from the beryllium cell dominated the diffraction patterns of the empty and filled cell. The difference between the two patterns gave the sample intensity after corrections were applied (see Chapter VI). Therefore, it was essential that the gross detected intensity for each angle include only the intensities characteristic of that angle from each scattering element. However, with sample in the cell the strong

absorption of the liquid caused the center of gravity of the beryllium peaks to appear slightly shifted. [31] This was not an actual shift of the peak intensities from each scattering element. Since each element was physically displaced from the goniometer zero, the apparent shift was due to a change in the relative contributions of the elements to the gross scattered intensity. The effect was further exaggerated by the horizontal and vertical divergence of the incident and scattered beams. To relate the beryllium peak intensities to their characteristic angles required a high degree of angular resolution.

Beam collimation of the Norelco goniometer was improved by introducing finer Soller slits. The arrangement used is shown pictorially in Figure 15. The vertical Soller slits, General Electric Type A 4954 AF, collimated the incident beam in the horizontal plane. The horizontal slits, GE Type A 4960 BD, limited divergence of the scattered rays in the scattering plane. Each vertical slit was 2.5 mils thick; they were spaced 18 mils apart. The horizontal slits were 2.4 mils thick and spaced 5 mils apart. The combined effect of the two sets of slits gave an angular resolution of better than one degree above $\theta = 10^o$ (see Appendix IV). With this degree of collimation the widths of the characteristic beryllium peaks were narrowed to the point where the line shift was tolerable.

3. Cell Alignment

The sample cell was positioned horizontally along the axis of

the goniometer. Careful machining of the cell holder, temperature control annulus, lucite supports, and vacuum chamber was relied upon for supporting the cell perpendicular to the vacuum jacket end plate. When this end plate was placed parallel to the faced hub on the goniometer shaft, the cell axis was approximately parallel to the goniometer axis. Alignment in the scattering plane was approximated by matching two holes in the hub with two recessed holes in the end plate; the holes in the end plate had been placed at the same relative positions (with respect to each other and to the vacuum chamber axis) as the holes in the hub. With this alignment procedure the center of the cell and the center of the goniometer shaft coincided to within 0.002 inch as determined by mechanical testing. The final, more accurate alignment was established with the cell at low temperature by the method described below.

The wooden cradle supporting the cryostat rested on runners attached to a steel base plate. The cell could be moved in the scattering plane by means of adjustment screws on the base plate. Movement of the base plate and of the wooden cradle on its runners permitted alignment in the other two degrees of freedom.

Prior to each experimental run, final alignment was established. With the evacuated cell and its supports at a stable operating temperature, the main beam was scanned with the scintillation counter. For this scan very low intensity x rays were used; the x-ray tube voltage was 12 kilovolts and the tube current, 2 milliamps. At these conditions the absorption of the main beam by the cell walls was seen

clearly in the counter scan pattern. Figure 16 shows the data from one of the scans; data points were taken every 0.02 degree in 2θ. The vertical position of the cell was then calculated from the goniometer geometry. This position was known to better than ± 0.0005 in. For a given operating temperature it was reproducible to within the accuracy of the measurement.

In order to fix the cell position in the scanning plane, two other measurements were performed. An incident x-ray beam slightly narrower than the cell inner diameter was directed through the center of the cell. The exact beam position with respect to the cell was determined by the method described above. The cell was then scanned over the range of 2θ near 90 degrees using a scattered beam of dimensions similar to the incident beam. No scattered intensity should have been observed at the angle where the beams intersected within the empty cell. However, parts of the diffuse beam edges intersected cell material and caused some scattering to be detected. The minimum was more sharply defined by taking the ratio of this scattered intensity to that observed using incident and scattered beams which bathed the entire cell. Data from one of the alignment determinations is illustrated graphically in Figure 17. The minimum appears here as a maximum because the inverse ratio of the narrow and wide beams is plotted. From the angle of minimum intensity and the goniometer geometry the horizontal cell position was calculated. Uncertainty in the angle of minimum intensity limited the determination to ± 0.001 in.

4. The Partially Exposed Cell

Only part of the cell and sample were irradiated by the inci-
dent beam during an experimental run. This section is designated
by the shaded area of the cell in Figure 18. A 1/6 degree divergence
slit (0.0066 in. wide) and 0.111 in. wide receiving slit defined the
incident and scattered beams shown. Because of the geometries of
the anode and divergence slit, the beam edges are not sharp as de-
picted in the figure. The corrections for this effect are discussed
in Chapter VI. 5.

This particular beam geometry was selected for several
reasons. First, the narrow incident beam reduced the total angular
divergence considerably, thereby reducing the line shift problem
discussed above. This advantage was more important than the
attendant loss in sample scattering intensity as a result of the re-
duction in irradiated sample volume. Secondly, self-absorption of
the scattered x rays in the sample was reduced to a minimum by
irradiating only the upper portion of the sample. Relatively higher
sample scattering intensities resulted, but even more important was
the low absorption of incoherent scattering. Considerable simplifi-
cation of the absorption corrections was thereby permitted.

Third, beryllium cell scattering was limited as much as
possible by lowering the upper edge of the incident beam. The cell
scattering could almost be eliminated by using a very narrow
scattering beam. However, the absorption corrections would be
very much more complicated. Present computational methods for

calculating absorption factors can treat cells partially irradiated by only one of the beams.

The final consideration was the position of the irradiated sample volume with respect to the goniometer axis. Because of the contraction of the cell assembly and lucite cell supports during cooling, the cell was lowered from its position at room temperature. For operating temperatures near -130° C, the cell axis was aligned with the goniometer axis at room temperature. Then, quite fortuitously, the cell dropped 0.037 in. to place the goniometer axis quite near the geometrical center of the shaded sample volume. This made any angular corrections in goniometer readings negligibly small.[*]

---

[*]The cell position was determined by the methods described in the preceding section. At -130° C the geometrical center of the sample was displaced 0.010 in. vertically and 0.008 in. horizontally from the goniometer axis. The resulting angular correction varied from -0.201 degrees at low angles to 0.089 degrees at the largest scattering angle.

IV. CALIBRATIONS

A. Temperature Measurement

The sample temperature was measured by placing a small platinum resistance element directly into the sample fluid. This element was a Type P4 hard glass resistance element manufactured by the Degussa Company of Hannau, Germany. It consisted of a single platinum wire wound on a small glass rod and covered with a very thin layer of glass. Two platinum-clad, #30 copper wires were welded to the primary element and passed through the glass casing to provide electrical leads. The overall thermometer dimensions were 2 mm diameter by 25 mm length. The nominal ice point resistance was 100 ohms, and the temperature coefficient, dR/dT, was approximately $0.4 \, \Omega/^{\circ}C$ over the temperature range 10° to 300° K.

The thermometer was calibrated at a number of temperatures between 77° and 300° K. An interpolation formula based on two of the calibration points was used to prepare an R vs. T table, and the other calibration points were utilized in a deviation plot for the table. When the thermometer was used at elevated pressures, a correction for the hydrostatic pressure was found to be necessary. Also, because of the physical displacement of the thermometer from the irradiated portion of the sample, a correction derived from the cell temperature profile had to be made. The calibration and corrections are discussed below.

1. Thermometer Calibration

The thermometer was calibrated by comparison with a Leeds
& Northrup 25-ohm, strain-free, platinum resistance thermometer
(No. 1612803). This standard thermometer had been calibrated by
the National Bureau of Standards in 1963 at the steam, oxygen, and
sulfur points. The NBS calibration table is based on the International
Practical Temperature Scale. Linear interpolation between tabulated
values introduced an error of less than 0.0001° C for temperatures
above 28° K.

The cross-sectional view showing some of the details of the
calibration apparatus is given in Figure 19.[*] It consisted principally
of the cylindrical copper block, D, suspended in the vacuum jacket,
E. During the calibration the vacuum jacket was partially immersed
in a large steel Dewar filled with liquid nitrogen. Four platinum
resistance elements, C, (only two are shown) were placed in close-
fitting wells in the copper block. Silicone oil in the wells assured
good thermal contact between the thermometers and the block. The
standard platinum thermometer, H, was mounted in a tapered copper
plug with Wood's metal. This plug was pressed firmly into a lapped
hole in the copper block; silicone grease was used for lubrication.
A thin-walled copper lid, J, served as a radiation shield for the end
of the standard thermometer. The thermometer leads were wrapped
several times around the plug and the copper block to reduce heat
flow into the thermometer.

-----

[*]The calibration apparatus was designed by Dr. C. M. Knobler.

The copper block assembly was completely enclosed within the radiation shield, G. Silk threads supported the block from the removable end plate of the shield. Three lucite rods, F, in turn supported the radiation shield beneath the brass support lid, A. The support lid rested on a brass flange which had been soldered to the inside of the vacuum jacket. All thermometer, thermocouple, and heater wires were bundled and passed through a hole in the support lid. The copper disc, B, reduced radiant heat transfer through the hole. The tubular handle on the support lid was provided for lowering and withdrawing the apparatus from the vacuum jacket. The electrical leads were anchored to the handle and copper block with GE 7031 insulating varnish.

A lucite end plate, K, with O-ring seal provided the closure for the vacuum jacket. Electrical leadouts were made by 1/8 in. copper pins sealed in the plate. Extra lengths of the wires were spiralled down the walls of the jacket to reduce heat losses. An opening, L, connected to a high vacuum system.

In Figure 20 the assembly is shown just prior to installation. Figure 21 shows the vacuum jacket with the liquid nitrogen Dewar lowered; the vacuum pump is seen in the foreground.

Initial cooling was performed with helium exchange gas in the vacuum jacket. Near the desired calibration temperature the gas was removed. Further cooling proceeded mainly by radiative heat transfer from the walls of the vacuum jacket. The final calibration temperature was reached by passing a short pulse of electric current

through a heater wound spirally around the tapered plug. This temperature was then maintained by keeping the radiation shield at the same temperature as the copper block. In order to accomplish this, a heater on the outside of the radiation shield was controlled in the same manner as the heater system for the x-ray cryostat; a difference thermocouple between the shield and the block actuated the control circuit. A vacuum of approximately 10^{-6} mm Hg was maintained during the calibrations.

The thermometer currents and voltages were measured by the methods described in Chapter III. C. 2 (see wiring diagram of Figure 9). The miniature resistance elements were wired in series in the current loop so that the same current (one milliamp) passed through each of them. The standard thermometer was maintained in a circuit separate from the calibration thermometers' circuit. All potential leads were connected to the Wenner potentiometer through a selector switch to facilitate circuit switching.

During the course of a measurement the standard thermometer was read alternately with each of the resistance elements. In cases where the temperature was slowly drifting, simple linear interpolations between the standard thermometer resistance readings were used to obtain the temperature of the resistance element at the time it was read. All interpolations were between temperatures separated by less than 0.005° C.

The thermometers were calibrated at eleven temperatures between 77° and 300° K. The results for thermometer No. 2 (the

thermometer used during the diffraction experiments) are tabulated

in Table 1. The absolute temperatures in Column 2 are those cor-

responding to the time interpolations between the standard thermom-

eter readings. Column 3 gives the resistances of the platinum re-

sistance element that were calculated from the measured values of

potential and current. Repeated temperature cycling of the ther-

mometer indicated no observable annealing effects within the

accuracy of the measurements.

In order to interpolate between the calibration points, an

interpolation table was prepared from a formula suggested by

Corruccini:[33]

$$X_T = X_1 + b(R_T - R_1)$$

where

$$b = (X_2 - X_1)/(R_2 - R_1)$$

X_T is the interpolated resistance at temperature T; X_1 and X_2

are the measured resistances at two arbitrary temperatures T_1 and

T_2; R_T, R_1, and R_2 are the resistances of the standard ther-

mometer at temperatures T, T_1 and T_2, respectively. It is based

on Mathieson's Rule that the resistance of a metal is proportional to

the element's specific resistivity. The constant b was calculated

from the calibration values at 77.715^O and 273.015^O K. A resistance

table of interpolated values for 0.1^O C temperature intervals was

calculated on an IBM 7090 computer.[*]

Since Mathieson's Rule is only an approximation, the interpolated values deviate from the measured ones. The interpolated values for each of the calibration temperatures are listed in Column 4 of Table 1. Column 5 shows the differences. These difference values were used to prepare the deviation plot shown in Figure 22. Least square lines were fitted to the upper and lower regions of the data. The two lines were used to correct the interpolated temperature values. The data points for the range 77° to 158° K (this is the temperature range of interest for liquid argon studies) show a standard deviation of 0.0029° C from the least squares line; the maximum deviation is 0.0050° C.

2. Effect of Pressure On the Thermometer

The platinum resistance thermometer was placed directly in the sample fluid and was subject to the same pressure as that exerted upon the sample. The effect of pressure on the thermometer was examined in the following manner.

Two thermometers were first placed in a pressure bomb filled with oil. The bomb was then pressurized several times to 2000 psig. There was no discernible damage to either of the thermometers.

The influence of pressure on the thermometers was measured at four temperatures: 77°, 150°, 191° and 273° K. One of the thermometers was used at the lower three temperatures and the second

---

[*]The computer program was written by A. P. Kendig.

thermometer at 273° K. For all calibrations the thermometer was installed in the cell closure nut, and the cell and cell holder were fully assembled. The pressure manifold was removed from the vacuum chamber and replaced with pressure fittings which connected the sample line to a cylinder of high pressure helium. The tests at 77°, 191° and 273° K were performed with the cell holder immersed in Dewars of liquid nitrogen, crushed dry ice, and crushed ice, respectively; procedures recommended by Scott[33] were followed for preparation of the baths. For the test at 150° K the cell assembly was installed in the temperature control annulus, and temperature control was applied just as it was during an experimental run.

The isothermal resistance of the thermometer was determined for each of the four temperatures at several pressures between 100 and 1500 psig. The data obtained at 77°, 150°, and 273° K are illustrated graphically in Figure 23. Since the resistance varied linearly with pressure for the first two calibrations at 77° and 273° K, measurements at the other two temperatures were taken only at the pressure extremes; linear behavior was assumed.

The temperature of the dry ice bath (191° K) drifted slowly with time. It was therefore necessary to use an alternative procedure for these measurements. After steady state had been established at each pressure thermometer readings were taken alternately at 100 and 1100 psig. Return of the thermometer reading to the same drift rate permitted linear interpolation between the points. The data are illustrated graphically in Figure 24. The vertical distance

between the two lines gives the instantaneous change in resistance between the two pressures. The difference remained constant over the small temperature range.

Data was taken in ascending and descending pressure increments for the ice point and the liquid nitrogen point. No hysteresis effects were observable. All the tests indicate that the pressure effect is completely reversible for repeated pressure cycling.

The data show that the effect of pressure on the thermometer is a function of temperature. The nominal temperature change with pressure is plotted as a function of the absolute temperature in Figure 25. The point for thermometer 2 fits nicely on the extrapolated curve through the values for thermometer 1. It was therefore assumed that all the thermometers of this particular type behaved similarly. Since the pressure effect introduced a very small correction to the thermometer reading, the assumption of similarity was considered suitable for the present set of experiments.

The measured values of $\frac{1}{R}(\frac{\partial R}{\partial P})_T$ agree in order of magnitude with those reported by E. Grüneisen for pure platinum.[34] Table 2 shows the comparison. It must be noted that the thermometer pressure coefficient varies with temperature in a direction opposite to that for pure platinum. It is possible that this behavior can be attributed to the interaction of the glass core and casing with the platinum thermometer element.

3. Effect of Cell Temperature Gradients on Temperature Measurement

Because of the asymmetry of the cell holder about the irradiated portion of the cell, temperature gradients occur along the length of the cell. As a result, the temperature of the fluid in the x-ray beam is not the same as that indicated by the thermometer. Several tests were made (1) to estimate the extent of the temperature variations in the vicinity of the thermometer, and (2) to determine the optimum operating conditions for minimizing the gradients over the irradiated portion of the sample.

The cell temperature profile was determined from temperature measurements at five positions in the sample extending from the x-ray gap to the closure nut extension. The thermocouples were made from five #40 Teflon-insulated copper wires and one #36 Teflon-insulated Constantan wire. The copper wires were soldered to the Constantan wire at the five positions of interest. The Constantan lead was then connected to a #40 copper wire in an external ice bath. In this manner the potentials could be determined across any two junctions in the sample or across any sample junction and the reference ice bath junction.

The thermocouple leads passed out of the sample area through a small hole in the sealing plug of the closure nut extension. The leads were sealed in the hole with epoxy cement. They were then anchored around the closure nut extension and inlet coolant tube in the manner described above (see Chapter III. A. 2).

Temperature profiles were measured at 131° and 143° K with liquid ethane in the cell. Ethane was chosen for its low vapor pressure at these temperatures; this avoided the need for high pressure seals for the small thermocouple leads.

Measurements of the temperature profiles at these temperatures were made for a wide variety of temperature control conditions. The coolant flow rate and temperature control difference across the x-ray gap were varied independently until "optimum" temperature profiles were obtained. Two such curves for $T = 143^{\circ}$ K are illustrated in Figure 26. The outlines of the thermometer position in the cell assembly are shown to indicate the relative positions of the thermocouple junctions. The temperature profiles have been normalized to the center of the irradiated portion of the cell. The temperature referred to as the coolant temperature is a measure of the coolant flow rate; it is the sample temperature in the absence of control heating. During control the smaller side of the temperature control annulus was controlled at the higher temperature.

In curve A the temperature gradients across the irradiated sample are less than 0.003° C. However, the temperature curve rises more sharply over the region including the thermometer than it does in Curve B. Because the thermometer indicates an average temperature over its length, the more sharply rising curve introduces more uncertainty in the accuracy of the temperature measurement. Curve B is flatter over the thermometer region but has a larger gradient, about 0.015° C, over the irradiated portion of the

sample. In the selection of the "optimum" operating conditions, it must be noted that these temperature profiles were measured with thermocouples in liquid ethane; the gradients were different when the platinum thermometer was in the liquid sample. The presence of the thermometer should flatten the temperature profiles over the region of measurement.

On the basis of the above remarks, an estimation of the accuracy of temperature measurement was made from the temperature profiles. It was estimated that, with the operating conditions of curve B, the thermometer indicated an average temperature which was $0.050^\circ \pm 0.050^\circ$ C higher than that across the irradiated portion of the sample. This estimate was considered to be conservative.

B. Pressure Measurement

The use of the Hart pressure balance for sample pressure measurement is described in Chapter III.C.4. The Hart balance has an accuracy of 1:10,000 and sensitivity of 1:20,000. The sensitivity of the diaphragm pressure transducer was evaluated in order to determine whether or not it limited the pressure balance specifications.

1. Distance Detector Calibration

The sensitivity of the Bently distance detector was determined by measuring its voltage output as a function of the distance between it and a flat steel diaphragm. Both were immersed in hydraulic oil

at atmospheric pressure. The detector was attached to a microme-
ter screw to position it precisely. The electrical connections were
the same as those in Figure 12.

At each detector position the potentiometer screw on the
Bently electronics was varied over its entire sensitivity range. The
calibration curves in Figure 27 were constructed from the data.
The detector voltage is plotted against the distance between the
detector and the diaphragm. Each curve corresponds to a particular
potentiometer setting. These curves resemble those supplied by the
manufacturer for calibration in air.

2. Diaphragm Sensitivity

With the diaphragm and detector installed in the pressure
manifold, small overpressures were applied to the diaphragm to force
it up against the backing plates. The detector output at those dia-
phragm positions permitted determination of the diaphragm position
from the calibration curves of Figure 27. The null position, defined
as the position of zero pressure differential across the diaphragm,
was estimated to occur at a distance of 0.055 in. from the detector.
At this position of the diaphragm a transducer potentiometer setting
of eight turns gave the maximum sensitivity over a linear operating
range. The sensitivity of the Bently detector is approximately 460
volts per inch in this interval.

The diaphragm was calibrated by applying small pressure
differences across it at system pressures of 1, 30, 50, and 70

atmospheres. The pressures were established by injecting oil with
the pressure bench intensifier while simultaneously increasing the
gas pressure from a supply cylinder. The null position output was
measured first at each pressure by equalizing the oil and gas pres-
sures. This was done by shunting the two pressure lines into a large
pressure bomb; the large volume of the bomb kept the gas-oil inter-
face at a constant position during the measurements. Then, the
pressure bomb was isolated and the pressure balance connected to
the oil system. While a constant gas pressure was maintained from
the supply cylinder, small weights were added to the pressure balance
to alter the oil pressure by known amounts. The change in the distance
detector output as the oil pressure was varied gave the transducer
sensitivity.

The calibration data are illustrated graphically in Figure 28.
No hysteresis of the diaphragm was observed. For all pressures the
transducer sensitivity at the diaphragm null position was approxi-
mately 3.27 volts per psi pressure differential. As mentioned above,
a potential divider reduced the detector output to the millivolt range
for display on the recorder. On the 0-10 millivolt range a differential
pressure of 0.01 psi was easily observable. For system pressures
above 200 psig this sensitivity exceeded that of the pressure balance.
Even smaller pressure differentials could be detected by utilizing
a greater fraction of the output. Methods for increasing the sensitivity
are discussed in Appendix III.

An interesting feature of the calibration curves is their shape. Although the distance detector was operated over a linear output range, the curves are markedly non-linear. This effect is most probably due to radial stresses induced in the diaphragm during welding to the backing plate.

The null position output increased slightly with an increase in system pressure. The change was linear and reproducible. Figure 29 illustrates the magnitude of the effect. Changes in the null position introduced only a very small uncertainty into the determination of the absolute sample pressure. During the experimental runs, fluctuations in pressure control were quite large compared to uncertainties in pressure measurement. Chapter V. B describes pressure measurement and control during one of the runs.

V. EXPERIMENTAL CRYOSTAT OPERATION

A. Operating Procedure

The sequence of operations performed during an experimental run is described briefly below. The reader is referred to Appendix II for a detailed account of the operating procedure.

Before cooling the cell, the vacuum chamber and sample cell were evacuated. A rough pumping system was used to pump the two systems down from atmospheric pressure. At times when the vacuum chamber system was leak tight, it was left under vacuum continuously with just the ion pump in operation.

As soon as the chamber pressure was below 1 micron Hg, cooling was begun. When operating at control temperatures from 77° to $120^{\circ}K$, liquid nitrogen was circulated through the cooling coils. At higher temperatures gas cooling was used. Consumption using liquid nitrogen was approximately six liters per hour. Gas coolant consumption as a function of the steady state temperature in the absence of heating is shown in Figure 30. Illustrated on the same graph is the power input necessary to transfer the coolant. The appropriate voltage was applied to a heater placed in the supply Dewar.

When gas cooling was used for control, liquid cooling was employed to cool the apparatus more efficiently. The coolant transfer tube was inserted in the supply Dewar until the end of the tube extended a short distance below the liquid nitrogen surface. Then, by the time the desired temperature was reached, the liquid level fell below

the end of the tube; and gas cooling commenced. Cooling from room temperature to 90° K required approximately one hour.

During the initial cooling period the absolute control thermocouple output was displayed on the Speedomax recorder. When the temperature record indicated that the coolant flow had reached steady state, automatic temperature control was applied. The reference voltages for heater control circuits were selected to establish the "optimum" cell temperature profiles. Then the heater currents were increased manually with the Series 60 control units. When the control temperatures were reached, the controllers were switched to automatic operation.

Now, with the cell still evacuated, the 50% transmission window was set on the pulse height selector. First, the pulse amplitude distribution of the Mo $K\alpha$ radiation was determined with the counter set at the characteristic Bragg angle for the beryllium cell. Then the window settings were established by trial and error to admit approximately 50% of the integrated $K\alpha$ intensity. Several empty cell check points (see Chapter VII. A. 3) were taken.

A small amount of sample gas was then loaded into the cell. The oil pressure on the diaphragm was increased to just over one atmosphere gauge pressure. Next, the sample was bled into the cell until the pressure transducer indicated the oil and gas pressures were balanced. When the platinum resistance thermometer was used for

temperature control, automatic control was transferred at this time from the absolute control thermocouple to the resistance element.

For low sample pressures the sample gas was loaded directly from the sample supply cylinder. If higher pressures were desired, the sample was distilled into the sample loading bomb and then into the cell. During the filling operation the oil pressure was increased concurrently with the gas pressure to avoid overpressurizing the diaphragm. By maintaining fine control on the pressure manifold bleed valve the filling operation proceeded smoothly and without difficulty.

As liquid began to condense in the cell, it was necessary to operate the temperature controller manually. After condensation had slowed to the point where somewhat steady conditions were reached, automatic control was resumed.

Additional sample was bled into the cell to pressurize the liquid to the desired value. When the Heise gauges indicated that the control pressure had been reached, the pressure balance was connected to the system. Gas pressure was adjusted with the trimmer injector on the manifold until the pressure transducer indicated the diaphragm null position. It was often found necessary to add more sample to maintain the control pressure until all parts of the system had reached steady state.

The filling operation required about one hour. Before beginning the diffraction scan, x rays were counted at the check point angle to insure that conditions were constant. During the scan the check

points were taken every half hour. The pressure balance was adjusted hourly to account for changes in atmospheric pressure. When using the platinum thermometer method of temperature control, the potentiometer was standardized regularly.

The diffracted intensities were measured for 100 seconds at every half degree over the range 3° to 150°. When the automatic step scanner was used, a complete scan required eighteen hours. The counting time could be reduced to twelve hours by advancing the counter manually.

At the conclusion of a diffraction scan the sample was transferred back to the supply cylinder. When the sample pressure was reduced to one atmosphere, temperature control was transferred to the control thermocouple method; and the cell was evacuated. Empty cell check points were taken as quickly as possible after the end of the diffraction scan. The cell could normally be unloaded and evacuated in less than one hour.

When the vacuum chamber was leak tight, the evacuated cell was maintained at low temperature between runs. If the chamber pressure was above 10^{-5} mm Hg, however, condensable vapors accumulated on the interior of the apparatus after two days of operation. The cell assembly then had to be warmed to room temperature to pump out the vapors.

B. Summary of Performance Characteristics

The performance of the cryostat can best be described by a review of the control records during one of the diffraction runs on

argon.

Temperature measurement and control is summarized in the following table for Run VI-14.

Temperature observed (Chart recording for platinum thermometer)	$143.214 \pm 0.006^\circ$ K
Interpolation correction (Figure 22)	$- 0.067 \pm 0.002$
Pressure Effect correction (Figure 25)	$+ 0.053 \pm 0.002$
Temperature Gradient correction (Figure 26)	$- 0.050 \pm 0.050$
Average Control Temperature	$143.15 \pm 0.06^\circ$ K

Pressure measurements and control is summarized in the following table for the same run.

Pressure Balance reading (Calibrations accompanying balance)	1142.741 ± 0.077 psi
Atmospheric Pressure (Barometer reading)	$+ 14.303 \pm 0.077$
Oil Head correction (Calculated)	$- 0.600 \pm 0.010$
Gas Head correction (Calculated)	$+ 0.100 \pm 0.050$
Diaphragm Average Control position (from chart recording and Figure 29)	$+ 0.100 \pm 0.030$
Limits of pressure control (from chart recording and Figure 28)	0.00 ± 0.20
Average Control Pressure	1156.65 ± 0.36 psi

During this run the pressure in the vacuum jacket was maintained at about 7×10^{-5} mm Hg. The heater in the coolant supply Dewar was held at 68 volts (46 watts). Heater control current during automatic temperature control of the cell assembly averaged 165 milliamps (0.5 watts). The 150-liter coolant supply Dewar of liquid nitrogen provided continuous cooling for approximately 36 hours.

VI. GENERAL TREATMENT OF DIFFRACTION DATA

A. Electrical Noise

A small amount of electrical noise accompanied the diffraction signal in the registered output from the detection circuit. This background consisted of pulses accumulated from sources other than the scattered x rays. For this experiment it was measured by closing the shutter for the incident x-ray beam; the noise was independent of the position of the counter. With an 11.4-volt window centered at 47 volts on the pulse height analyzer, the average noise level varied from 0.07 to 0.22 counts per second. This level was so small in comparison with other background corrections (16 counts per second minimum) that statistical fluctuations were ignored. The noise background was measured at regular intervals during the experimental runs, however, and the average value was subtracted from the raw data. In the discussion which follows it is assumed that all the intensities have been corrected for the electrical noise.

B. Polarization

Since the incident beam was unpolarized and polarization occurred in the scattering process, a correction had to be applied to the experimental intensities. The theoretical intensity, $I(S)$, was reduced on scattering to[11]

$$I^E(S) = PI(S) \qquad (3)$$

where

$$P \equiv \frac{1}{2} (1 + \cos^2 2\theta)$$

and $I^E(S)$ is the experimentally observed intensity.

C. Cell Scattering and Self-absorption in the Sample and Cell

In diffraction experiments utilizing a sample container of small diameter, detection of the scattering from the cell walls is unavoidable. With partially irradiated cells of the type described in Chapter III. D. 4, scattering from the cell contributes heavily to the diffracted intensity. In order to recover the signal from the sample alone, the diffraction pattern of the empty cell must be measured and subtracted from the intensity of the cell with sample in it (hereafter referred to as cell plus sample intensity). The absorption of the incident and scattered beams is intimately connected with this subtraction process and must be considered coincidentally to obtain the proper correction. A brief review of the treatment by Blake,[35] Ritter,[36] and Paalman and Pings[37] is presented below.

The total experimental intensity leaving the cell with sample in it may be written as

$$I_{c+s}{}^E(S) = P \left[A_{c, sc}(S)I_c(S) + A_{s, sc}(S)I_s(S) \right] \qquad (4)$$

$I_c(S)$ and $I_s(S)$ are the cell and sample intensities which would be observed if each scattering element were irradiated with the same incident intensity and if the scattered rays were not absorbed. The coefficients $A_{i, j}(S)$ account for the diminution of the scattered intensity which occurs as a result of absorption of both the incident

and scattered beams. $A_{c,sc}(S)$ is the absorption factor for absorption of scattering from the cell in both the sample and cell. P is the polarization factor described previously. Diffraction effects arising from the intercorrelation of the cell and sample structure have been neglected in this treatment; justification of this assumption is given by Paalman and Pings.[37]

The cell and sample intensities are inseparable in the experimental intensity, $I_{c+s}{}^{E}(S)$. Therefore, the scattered intensity from the empty cell must be measured; it can be described by the equation

$$I_c{}^{E}(S) = PA_{c,c}(S)I_c(S) \qquad (5)$$

Analogous to the absorption factors defined above, $A_{c,c}(S)$ is the absorption factor for scattering and self-absorption in the cell.

Combining equations (4) and (5) and solving for the sample intensity gives

$$I_s(S) = \frac{1/P}{A_{s,sc}(S)}\left[I_{c+s}{}^{E}(S) - \frac{A_{c,sc}(S)}{A_{c,c}(S)}I_c{}^{E}(S)\right] \qquad (6)$$

Thus, the sample intensity may be obtained by evaluating the absorption factors and measuring the diffracted intensities from the empty cell and the cell plus sample.

For cylindrical cells of the type used in this experiment, the absorption factors take the form

$$A_{s,sc}(S) = \frac{1}{A_s}\int_{A_s} e^{-\mu_s \ell_s(r,\omega;S)-\mu_c \ell_c(r,\omega;S)} dA_s \qquad (7)$$

In this equation A_s is the cross-sectional area of the irradiated

sample; μ_s and μ_c are the linear absorption coefficients for the

sample and cell, respectively (absorption coefficients are usually

reported as $\mu/\bar{\rho}$ and are therefore dependent on the physical state

of the material); ℓ_s and ℓ_c are the optical path lengths through

sample and cell of a ray incident upon a scattering point at (r, ω)

and scattered in the direction $S = (4\pi/\lambda)\sin\theta$; and r and ω are the

radial and angular coordinates of the scattering element with respect

to the center of the cell. The integral may be evaluated numerically

as described by Paalman and Pings.[37] A computer program written

for this purpose correctly evaluated the factors for annular cells

given by Ritter. These treatments, however, only considered cells

fully exposed to the incident and scattered beams. Absorption

factors for partially exposed cells, such as the one shown in Figure

18, are discussed by Kendig and Pings.[38] A computer program

written by Mr. Kendig was used to evaluate the absorption factors

for the present case.

D. Incoherent Scattering Losses[*]

The experimentally observed intensities include both the

coherent and incoherent, or Compton modified, radiation. For

monochromated incident radiation, the wavelength of the incoherent

scattering is related to the wavelength of the coherently scattered

---

[*]Except where noted otherwise the equations in this section were
derived jointly by the author and P. G. Mikolaj.

radiation by[39]

$$\lambda^{inc} = \lambda^{coh} + 0.0243(1 - \cos \theta) \tag{8}$$

The intensities of the modified radiation are obtained from quantum mechanical calculations.

For sample materials of low atomic number, the incoherent scattering forms an appreciable part of the detected radiation. In the case of beryllium, the incoherent contribution rises rapidly from zero to 82% of the continuum at $\theta = 20^{o}$; and at higher angles it forms greater than 95% of the total scattered intensity. The relative amounts are not so high for argon, but at 75° amount to a 62% contribution.

Two assumptions about incoherent scattering are implicit in the treatment of diffraction data described previously. The first is that the absorption of incoherent scattering from the sample and the cell is adequately accounted for by the absorption factors calculated for coherent radiation. The second assumption is that the incoherent scattering is transmitted through the detection system with the same efficiency as the coherently scattered radiation.

With respect to the first assumption, the absorption factors illustrated by equation 7 are functions of the linear absorption coefficients, μ. The coefficients are, however, functions of the wavelength of the transmitted radiation according to the relation[40]

$$\frac{\mu^{inc}}{\mu^{coh}} = \left[\frac{\lambda^{inc}}{\lambda^{coh}} \right]^{k} \tag{9}$$

The exponent k is characteristic of the absorbing medium; for most

materials it has a value near 3. If the presence of incoherent radiation is neglected in the calculation of the absorption factors, the theoretical intensities will be in error. The error will be angular dependent; it will be most serious for measurements at large scattering angles on materials with appreciable amounts of incoherent scattering.

The second assumption deals with the incoherent scattering between the time that it leaves the scattering material and the time that it is viewed by the experimentalist as part of the scattered intensity. The previous data treatment assumes that the coherent and incoherent intensities are transmitted in equal proportions through the detection circuit to the registered output. For reasons discussed below, this is not necessarily the case. Since the normalization of the data to absolute intensity units is dependent on having the correct relative amounts of coherent and incoherent radiation, it is important to consider the magnitude of this effect.

The corrections for losses in the incoherent intensity occurring in these two areas, i. e. within the sample and cell and in the detection circuit, are discussed in the following sections.

1. Absorption in the Cell and Sample

Equations (4) and (5) for the experimentally observed intensities can be modified to include explicitly the incoherent scattering contributions from both the sample and the cell:

$$I_{c+s}{}^{E}(S) = P\left[A_{c,sc}^{coh}(S)I_{c}^{coh}(S) + t_{c}^{inc}(S)A_{c,sc}^{inc}(S)I_{c}^{inc}(S)\right.$$

$$\left. + A_{s,sc}^{coh}(S)I_{s}^{coh}(S) + t_{s}^{inc}(S)A_{s,sc}^{inc}(S)I_{s}^{inc}(S)\right] \qquad (10)$$

$$I_{c}{}^{E}(S) = P\left[A_{c,c}^{coh}(S)I_{c}^{coh}(S) + t_{c}^{inc}(S)A_{c,c}^{inc}(S)I_{c}^{inc}(S)\right] \qquad (11)$$

The coefficients $t_{c}^{inc}(S)$ and $t_{s}^{inc}(S)$ are defined as transmission factors for the cell and sample; they account for the relative losses in the incoherent intensities occurring by processes other than cell and sample absorption. The transmission factors are discussed in the next section.

Before these two equations are combined to obtain an expression for the sample intensity, it is convenient to introduce the quantity δ, which is defined as the fraction of the total scattered intensity consisting of coherent radiation. When this quantity is introduced into equations (10) and (11), the sample intensity may be solved as before:

$$I_{s}(S) = \frac{1/P}{A'_{s,sc}(S)}\left[I_{c+s}{}^{E}(S) - \frac{A'_{c,sc}(S)}{A'_{c,c}(S)}I_{c}{}^{E}(S)\right] \qquad (12)$$

where now the modified absorption factors are defined by

$$A'_{s,sc}(S) \equiv \delta_{s}A_{s,sc}^{coh}(S) + (1-\delta_{s})t_{s}^{inc}(S)A_{s,sc}^{inc}(S)$$

$$A'_{c,sc}(S) = \delta_{c}A_{c,sc}^{coh}(S) + (1-\delta_{c})t_{c}^{inc}(S)A_{c,sc}^{inc}(S)$$

$$A'_{c,c}(S) = \delta_{c}A_{c,c}^{coh}(S) + (1-\delta_{c})t_{c}^{inc}(S)A_{c,c}^{inc}(S)$$

Estimations for δ_s and δ_c may be obtained by noting that, at large scattering angles, the scattering from either a liquid or a powder approaches the scattering for a collection of independent scattering particles (Klug and Alexander[41] give an example of the powder treatment). In other words, the relative amounts of coherent and incoherent scattering may be estimated by comparing the theoretical calculations for $f^2(S)$ and $I^{inc}(S)$. In the high angular region where the incoherent correction is significant, this approximation is valid.

Calculation of the incoherent factors, $A_{i,j}^{inc}(S)$ is quite complex. The linear absorption coefficient for the scattered ray is not only different from that for the incident ray, but it also varies as a function of angle according to equations (8) and (9). For example, the absorption factor $A_{s,sc}^{inc}(S)$ for a single scattering element m becomes (cf. equation (7))

$$(A_{s,sc}^{inc})_m = \exp\left[-\mu_c^{coh}(\ell_c^{\,i})_m - \mu_c^{inc}(\ell_c^{\,o})_m \right.$$
$$\left. - \mu_s^{coh}(\ell_s^{\,i})_m - \mu_s^{inc}(\ell_s^{\,o})_m \right] \qquad (13)$$

where the superscripts "i" and "o" refer to the incoming and outgoing rays.

As an approximation to the summation of the exponentials over all the elements, the absorption factors, $A_{s,sc}^{inc}(S)$, $A_{c,sc}^{inc}(S)$, and $A_{c,c}^{inc}(S)$, may be expressed in the same form as that for a single

scattering element.[*] The optical path lengths for each element are replaced by a single effective path length for the entire cell; the effective path lengths are characteristic of the scattering angle and the cell geometry. The resulting absorption factors then take the form

$$A_{s,sc}^{inc}(S) - exp\left[-\mu_c^{coh} \left\langle \ell_c \right\rangle^i - \mu_c^{inc} \left\langle \ell_c \right\rangle^o \right.$$
$$\left. - \mu_s^{coh} \left\langle \ell_s \right\rangle^i - \mu_s^{inc} \left\langle \ell_s \right\rangle^o \right] \tag{14}$$

This equation may be put into a more convenient form by introducing the quantity $\Delta\mu = \mu^{inc} - \mu^{coh}$ and factoring out the terms containing coherent contributions. The result is

$$A_{s,sc}^{inc}(S) = A_{s,sc}^{coh}(S) \, exp\left[- \Delta\mu_c \left\langle \ell_c \right\rangle^o - \Delta\mu_s \left\langle \ell_s \right\rangle^o \right]$$
$$= A_{s,sc}^{coh}(S) \, exp\left[- \Delta\mu_s \left\langle\!\left\langle \ell_s \right\rangle\!\right\rangle^o \right] \tag{15}$$

In this last expression, $\left\langle\!\left\langle \ell_s \right\rangle\!\right\rangle^o = \left\langle \ell_s \right\rangle^o + \dfrac{\Delta\mu_c}{\Delta\mu_s} \left\langle \ell_c \right\rangle^o$, is defined as the average effective path length of the scattered x-ray beam. This quantity was calculated by graphical methods.

The validity of this method for estimating the incoherent absorption factors was tested for the sample and cell geometry used in the liquid argon experiment; the linear absorption coefficients for the

---

[*]The following treatment for evaluation of the incoherent absorption factors was derived by P. G. Mikolaj. The detailed derivation and calculations may be found in his thesis.[42]

sample density 1.0052 gm/cm^3 were used. Although the estimated

effective path lengths differed from the true values by as much as 10

to 15%, the resulting error in the modified absorption factor of

equation (12) was less than 0.2% for all angles.

When this method was used to estimate $A_{c,sc}^{inc}(S)$ and

$A_{c,c}^{inc}(S)$, it was found that the maximum deviation of the ratio,

$A'_{c,sc}(S)/A'_{c,c}(S)$, from the coherent absorption factor ratio,

$A_{c,sc}^{coh}(S)/A_{c,c}^{coh}(S)$, was less than 0.1%. On this basis the ratio of

modified absorption coefficients was replaced with the coherent

factor ratio. With this simplification, equation (12) may be expressed

in the same form as equation (6); a coefficient, G(S), takes into

account all the corrections necessitated by the presence of incoherent

radiation.

$$I_s(S) = \frac{1/P}{G(S)A_{s,sc}^{coh}(S)} \left[I_{c+s}^{E}(S) - \frac{A_{c,sc}^{coh}(S)}{A_{c,c}^{coh}(S)} I_c^{E}(S) \right] \tag{16}$$

where

$$G(S) = \delta_s + (1-\delta_s)t_s^{inc}(S) \frac{A_{s,sc}^{inc}(S)}{A_{s,sc}^{coh}(S)}$$

It must be emphasized that this simplification is possible only

with certain scattering geometries. In particular, the ratio

$A'_{c,sc}(S)/A'_{c,c}(S)$ will be considerably different for experiments

with large amounts of incoherent scattering passing through greater

volumes of highly absorbing materials. The geometry described in

Chapter III. D. 4 is especially favorable in this respect.

2. Other Losses

The second assumption implicit in previous treatments of diffraction data is that both coherent and incoherent radiation are detected in proportion to their relative intensities leaving the sample and cell. Because of the differences in wavelength, however, incoherent scattering is not transmitted to the registered output in the same proportion as the coherent radiation. The transmission factors, $t_s^{inc}(S)$ and $t_c^{inc}(S)$, account for the relative reduction in incoherent scattering which occurs by processes other than cell and sample absorption.

The discussion below only considers losses in the $K\beta$ filter and the pulse height selector. Experiments with serious reduction of scattered intensities in other components can be considered by similar methods. With the apparatus used in this experiment, relative losses due to absorption in the Mylar window and in the air outside the vacuum chamber were insignificant because of the low total absorption. Losses due to the wavelength dependence of the detector counting efficiency were also negligible. The counting efficiency was essentially constant over the range of wavelengths of the incoherent radiation. If a proportional counter had been used, the correction would have been significant.

Relative reduction of the scattered intensities in the $K\beta$ filter can be expressed in the exponential function

$$t_f^{inc} = e^{-\Delta\mu_f^\ell f} \tag{17}$$

where $\Delta\mu_f$ is the difference between the linear absorption coefficients for the incoherent and coherent radiation, and ℓ_f is the filter thickness. The difference in absorption coefficients may be calculated from equations (8) and (9). The exponent, $k = 2.75$, was determined for the zirconium Kβ filter from the mass absorption coefficients given by Cullity.[43] The filter thickness was 0.0039 in.

The estimation of relative losses in the pulse height selector requires knowledge of the pulse amplitude distributions (PAD) of the coherent and incoherent radiation. As a result of the difference in wavelengths, the PAD for incoherent scattering is shifted with respect to that for coherent radiation. Since the window voltage settings remain fixed, the relative amounts of incoherent radiation transmitted through the pulse height selector change as a function of the scattering angle.

A comparison of the transmitted intensities may be made by calculating the relative integrated intensities admitted through the upper and lower window settings, v_2 and v_1.[*] The transmission coefficient is given by the equation

$$t_{PHS}^{inc} = \frac{\int_{v_1}^{v_2} PAD(\lambda^{inc}, v)\, dv}{\int_{v_1}^{v_2} PAD(\lambda^{coh}, v)\, dv} \tag{18}$$

---

[*]Equations 18 and 19 were derived by P. G. Mikolaj.[42] This author also wishes to acknowledge that the calculations for this section were performed by him.

where PAD(λ, v) is the properly normalized pulse amplitude distribution for radiation of wavelength λ.

Several experimental measurements showed that the PAD may be closely approximated by a normal, or Gaussian, distribution:

$$PAD(\lambda, v) = \frac{2.354}{W \sqrt{2\pi}} e^{-\frac{1}{2}\left[2.354\left(\frac{v-\bar{v}}{W}\right)\right]^2} \tag{19}$$

Here $\bar{v}$ is the mean pulse voltage corresponding to λ, and W is the width of the PAD at one half the maximum height. According to Parrish,[8] $\bar{v}$ and W are proportional to $(\lambda)^{-1}$ and $(\lambda)^{-1/2}$, respectively. They may be calculated for the incoherent PAD by using the experimentally determined values of $\bar{v}^{coh}$ and W^{coh} and equation (8) for the incoherent wavelength.

If the change of variable $x \equiv 2.354\left(\frac{v-\bar{v}}{W}\right)$, is made in equation (19), the integrals of equation (18) may be evaluated by using normal probability tables. When this calculation was performed for the experimental conditions used to obtain the argon diffraction data, i.e., $\bar{v}^{coh}$ = 47.0 volts and W^{coh} = 19.7 volts, the calculated window voltages for 50% transmission were 41.36 and 52.64 volts. The corresponding window settings determined experimentally were 41.3 and 52.7 volts. For these same experimental conditions, the values $\bar{v}^{inc}$ = 44.19 volts and W^{inc} = 19.10 volts were calculated for θ = 75°; the corresponding transmission coefficient was $t_{PHS}^{inc}(75°)$ = 0.9755.

3. Results of Incoherent Scattering Corrections

The angular dependence of the correction coefficient, $G(S)$ of equation (16), is given in Table 3. These correction factors were calculated for the experimental conditions under which the argon data was obtained. The factor $t_s^{inc}(S)$ in $G(S)$ is the product of the filter transmission coefficient, t_f^{inc}, and the transmission coefficient for the pulse height selector, t_{PHS}^{inc}. The fact that the total correction to $I_s(S)$ given by $G(S)$ amounts to less than 1% below θ of $25°$ justifies the approximation that δ could be represented by the theoretical ratio, $\left[f^2(S)/\left[f^2(S) + I^{inc}(S)\right]\right]$.

E. The Composite Incident Beam

Scattering geometries requiring the use of very narrow incident or scattered beams in a partially exposed cell have a unique absorption problem. In many cases, the divergence or scatter slits are of necessity positioned so far from the sample that the beam intersecting the scattering material is not well defined; i.e., the beam edges are quite diffuse. When these diffuse edges form an appreciable part of the beam width, as is the case with narrow beams, a single beam of uniform intensity cannot represent the actual beam realistically. Since the calculation of absorption corrections depends on an exact knowledge of the scattering geometry, it is important to attempt a more accurate definition of the beam shape. The discussion below describes a method for evaluating the absorption factors for cylindrical cells exposed to incident beams of

nonuniform intensity. The general approach is to decompose the beam into individual beam strips of different intensities. The strips may be made as narrow as is necessary to represent satisfactorily the actual beam shape. It is assumed that all the scattered rays are detected.

Consider an incident beam divided in the scattering plane into j individual beam strips of the same or different intensities. The unnormalized experimental intensity can then be written in absolute units as the sum of the contributions from the scattering volumes irradiated by the individual beams:

$$\left[I_{c+s}^{E}(S)\right]_{abs} = P \sum_{j} \left[A_o^2 A_{c,sc}(S)I_c(S) + A_o^2 A_{s,sc}(S)I_s(S)\right]_j$$

(20)

In this equation A_{oj} is the absolute value of the amplitude of the ray scattered from an isolated classical electron when irradiated by the incident intensity of beam j. For simplicity the incoherent scattering corrections are omitted; they may be included without affecting the general treatment.

The quantities $I_c(S)/\underline{N}_c$ and $I_s(S)/\underline{N}_s$ -- $\underline{N}_c$ and $\underline{N}_s$ are the number of irradiated electrons in the cell and sample scattering volumes V_c and V_s -- are intensive properties of the scattering material. They are therefore not dependent on the incident intensity and may be removed from the summation:

$$\left[I_{c+s}{}^{E}(S) \right]_{abs} = \frac{PI_c(S)}{\underline{N}_c} \sum_j \left[A_o^2 A_{c, sc}(S)\underline{N}_c \right]_j$$

$$+ \frac{PI_s(S)}{\underline{N}_s} \sum_j \left[A_o^2 A_{s, sc}(S)\underline{N}_s \right]_j \qquad (21)$$

Next, the experimental intensity is normalized to an arbitrary reference intensity, $(A_o^2)_{ref}$. Equation (21) may then be put into the desired form by utilizing the fact that the scattered intensities, A_o^2, are directly proportional to the incident intensity I^o. After rearrangement, the resulting expression is

$$I_{c+s}{}^{E}(S) = P \left[ACSC(S, I^o_{ref})I_c(S) + ASSC(S, I^o_{ref})I_s(S) \right] \qquad (22)$$

where the composite beam absorption factors are defined by

$$ASSC(S, I^o_{ref}) \equiv \sum_j \left(\frac{I_j^o}{I^o_{ref}} \right) \left(\frac{V_{sj}}{V_s} \right) \left[A_{s, sc}(S) \right]_j$$

$$ACSC(S, I^o_{ref}) \equiv \sum_j \left(\frac{I_j^o}{I^o_{ref}} \right) \left(\frac{V_{cj}}{V_c} \right) \left[A_{c, sc}(S) \right]_j$$

$$ACC(S, I^o_{ref}) \equiv \sum_j \left(\frac{I_j^o}{I^o_{ref}} \right) \left(\frac{V_{cj}}{V_c} \right) \left[A_{c, c}(S) \right]_j$$

The last absorption factor, $ACC(S, I^o_{ref})$ results from a similar treatment of $I_c{}^{E}(S)$. Thus, by knowing the relative incident intensities and scattering volumes irradiated by the individual beams, the

absorption factors for each strip can be combined into composite

absorption factors. These composite beam absorption factors may

be included in the scattering equations derived previously with no

complications.

The calculation of absorption factors by the composite beam

method was tested for the scattering geometry described in Chapter

III. D. 4. The geometry of the anode and divergence slit defined a

trapezoidal beam which intersected the cell with dimensions 0.0086 in.

for the umbra and 0.0189 in. for the penumbra; the calculations for the

beam dimensions agreed with experimental measurements. Each

beam edge was divided into three strips of equal width with intensities

1/6, 1/2, and 5/6 the umbra intensity $(I^o_{umbra} = I^o_{ref} = 1.00)$. For

the argon density $\bar{\rho} = 0.9098$ gm/cm^3 the composite absorption

factors were compared with those from three beams of uniform

intensity; the beams were 0.0116 in., 0.0136 in., and 0.0156 in. wide.

The differences between the composite factors and the uniform beam

factors ranged from 2.7 - 2.9% for ASSC, from 4 - 10% for ACSC,

and from 0.1 - 0.4% for ACC.

A comparison was also made of composite absorption factors

with the beam edges divided into three and six strips. In this case,

the maximum deviations between the two sets were only 0.1%, 0.4%,

and 0.2% for ASSC, ACSC, and ACC, respectively.

Finally, a comparison with grids[37] of m_R = 20 and 30[*] was

[*] A grid of m_R = 20 divided the sample cross sectional area into 1260
elements and the cell annulus into 5400 elements, each of approxi-
mately the same area. The grid of 30 divided the areas into 50%
more elements.

made for the top strip of the 6-strip beam to determine the adequacy
of the grid size for such narrow beams. The maximum difference
between the two sets for any of the absorption factors was less than
1%.

The calculation of an individual set of $A_{s,sc}(S)$, $A_{c,sc}(S)$,
and $A_{c,c}(S)$ with a grid of 20 for one-quarter-degree intervals
between θ of 0 and 75° would require approximately one hour exe-
cution time on the IBM 7090 computer. For this reason, the beam
strip absorption factors were computed at 2.5^{O} intervals and combined
into the composite factors. An interpolation program based on
Aitken's Method[44] was then used to secure the intermediate values.

Incorporation of the composite absorption factors into the data
treatment for incoherent scattering losses leads to the final equation
for the sample intensity:

$$I_s(S) = \frac{1/P}{G(S)ASSC(S, I^{o}_{ref})} \left[I_{c+s}^{E}(S) - \frac{ACSC(S, I^{o}_{ref})}{ACC(S, I^{o}_{ref})} I_{c}^{E}(S) \right]$$

(23)

The argon diffraction data given in Chapter VII was processed in
this manner. The composite absorption factors for the argon densities
0.9098, 0.9818 and 1.0052 gm/cm^3 are listed for 5° intervals in
Table 4. The correction factors, G(S), of Table 3 have been com-
bined with ASSC to provide coefficients compatible with the form of
equation (6). The linear absorption coefficients used in the calcula-
tions were 11.46, 12.37, and 12.66 cm^{-1} for argon (in order of

increasing density) and 0. 5448 cm^{-1} for beryllium;[43] the density of

beryllium was taken as 1. 82 gm/cm^3.

F. Normalization to Absolute Scattering Units

The experimental intensities, and therefore $I_s(S)$, are meas-ured in arbitrary, but internally consistent, laboratory units. In order to evaluate the radial distribution function by equation (2), the intensities must be normalized to electron units; these are the absolute intensity units in which $f^2(S)$ and $I^{inc}(S)$ are expressed. When $I_s(S)$ is determined from equation (23), the kernal for the Fourier transform of equation (2) becomes

$$i(S) = \frac{C\left[I_s(S) - I_o(S)\right] - NI_s^{inc}(S)}{Nf_s^2(S)} - 1 \qquad (24)$$

where C is the normalization constant and $I_o(S)$ is the zero-angle scattering.[10] Zero-angle scattering is appreciable only for a few minutes of arc above $\theta = 0^o$; in practice its presence is masked by the main beam.

Several methods for normalization have been suggested. One is based on the assumption that the observed liquid scattering ap-proaches the independent atomic scattering, $f_s^2(S) + I_s^{inc}(S)$, at high angles. A graphical fit of $I_s(S)$ to the theoretical curve is, however, subject to error because of the prevailing oscillations of the sample intensity. A variation of this method, in which the ratio

$I_s(S)/\left[f_s^2(S) - I_s^{inc}(S)\right]$, is plotted, provides a more sensitive test of

the stability of the normalization factor out to the limits of the ex-
perimental data. This procedure was applied to the argon data to
get preliminary values for the normalization constant. The best
normalization was then chosen by trial and error to minimize the
normalization effect on the radial distribution function.[10]

An alternative method is the integral normalization method
developed by Krogh-Moe[45] and Norman.[46] As the radial distance
from a reference atom approaches zero, the radial distribution
function approaches zero, and equation (2) may be written

$$-2\pi^2\bar{\rho} = \int_0^{S_m} S^2 I^{coh}(S)\,dS \qquad (25)$$

The normalization constant, C, may be chosen by trial and error to
satisfy this relation. The upper integration limit, S_m, can safely
replace the infinite limit of equation (2) because the value of the
integral is quite constant for data extending to reasonable values of
S.

Normalization constants calculated by this latter method were
not as satisfactory for the argon data as those obtained by the graphi-
cal method. Failure of the two methods to give exact agreement
could be traced to the general behavior of the corrected intensity
data; this point is discussed in Chapter VII. C.

The values for the atomic scattering factors used in the
normalization process were those computed by Berghius.[47] These
values agree to better than 1/2 % with those measured experimentally
out to $S = 5\,Å^{-1}$.[48] A correction for dispersion was applied using

the formula[49]

$$f_d^2 = (f_s + \Delta f')^2 + (\Delta f'')^2 \tag{26}$$

In this equation, f_s is the uncorrected value and $\Delta f'$ and $\Delta f''$ are the real and imaginary parts of the dispersion correction. The values $\Delta f' = 0.10$ and $\Delta f'' = 0.20$ were used.[48] The correction varied from 1.12% at $S = 0$ to 7.13% at $S = 16.3 \ \overset{\circ}{A}^{-1}$. Interpolation between the corrected values was performed by fitting a fifth order polynomial to the data.

Incoherent scattering factors which included exchange effects were not available for argon. Values were interpolated from those for Ca^{++}, K^+, and Cl^-, which did include exchange effects.[50] This method of interpolation was used by Chipman and Jennings[48] and by Furumoto.[51] Furumoto compared similarly interpolated values for neon with calculated values including exchange effects. The discrepancy was of the order of one per cent.

As a further check on the validity of the interpolation, the differences between the incoherent scattering calculations with and without exchange effects were plotted for Ca^{++}, K^+, and Cl^-. The older calculations without exchange[52] differed from the latest values by 15% at large values of S. The difference curve was interpolated graphically to get an estimate of the effect of including exchange in the argon calculations. The estimate was then added to the argon incoherent scattering calculated without exchange.[52] The results agreed to better than one per cent with those from the first method.

A relativistic correction, the Breit-Dirac factor,[53] must be applied to the incoherent scattering data. Since power is measured in photons per second with a scintillation detector, the correction factor appears as $1/B^2$ instead of the usual inverse third power.[54]

The data used to estimate the incoherent scattering for argon were given only up to $S = 13.8$ $\mathring{A}^{-1}$. The estimated argon points were extrapolated graphically to $S = 17$ $\mathring{A}^{-1}$. Since the data were changing very smoothly in this region, the error introduced by the extrapolation should be very small. A fifth order polynomial was fitted to all the data points to obtain the intermediate values.

VII. ARGON DIFFRACTION DATA

A. The Experimental Conditions

1. Selection of States

Experimental measurements were made on liquid argon at the densities 0.9098, 0.9818, and 1.0052 gm/cm^3 on the isotherm, -130° C;[*] the corresponding pressures were 586.60, 964.53, and 1156.48 psia. These states were selected as the first in a program for a systematic study of the liquid state of argon. Eventually, a temperature and density grid will be built up over the liquid region. The - 130° C isotherm was chosen because a reasonable variation in density (10.5%) could be achieved without going to extreme pressures. Also, a complete and authoritative set of volumetric data was available for this and eleven other isotherms between - 70° and - 150° C; this data was measured by J. M. H. Levelt at Amsterdam.[55]

The volumetric data are illustrated graphically in Figure 31. Also shown are the points at which Eisenstein and Gingrich[56] made their measurements. The lowest density state for the present study was chosen just inside the liquid region near one of the states measured by Eisenstein. An isochore through this point and the temperatures - 125° and - 122.5° C provides a convenient pressure range for succeeding measurements. The remaining two states along the - 130° C isotherm were selected at the pressures corresponding to

---

[*]The corresponding molar densities are 0.02278, 0.02458, and 0.02516 gm mole/cm^3.

the intersections of that isochore with the two higher isotherms;
this selection will permit the data grid to be expanded isobarically,
if desired.

Interpretation between the density data points which had been
measured was performed by solving a fifth order virial expansion in
the density.* This polynomial had been fitted to the data by Levelt.
Deviation of the original data points from the polynomial was of the
order of one part in 10^5; a corresponding polynomial at -100° C fit
data by Holborn and Otto[51] to better than 0.05%.

Within the liquid region, the specification of the temperature
and pressure established the state; measurement of these quantities
was sufficiently good to permit the determination of the sample
density to the precision (one part in 10^4) that it was reported in the
literature. The purity of the sample as measured by the Linde Rare
Gas Department, Union Carbide, exceeded the reported purity of the
sample used in the compressibility measurements. The maximum
impurity was one part per million of H_2O; traces of O_2, N_2, CO_2,
and hydrocarbons (no CH_4) were also reported.

2. Operating Conditions for the X-ray Equipment

The molybdenum x-ray tube was operated at its maximum
ratings in order to get the highest possible output intensity. The
voltage and current were set as close as possible to 55 kilovolts and
20 milliamps for each of the experimental runs. Since the coarse

*The computer program for solution of the polynomial was written
by R. H. Bigelow.

adjustments of control knobs prevented exact duplication of the tube settings, the experimental runs had to be normalized to one another. The check point intensities described below were used for this purpose. Also, the long term stability of the x-ray tube current and voltage were monitored indirectly by this same check point method.

The operating voltage on the photomultiplier tube of the scintillation detector was 850 volts. When the linear amplifier gain was at 50,000, the nominal $K\alpha$ pulse was approximately 47 volts. An 11.4-volt window centered about this value transmitted 50% of the $K\alpha$ pulses. The average noise level at these conditions varied from 0.07 to 0.22 counts per second during the experimental runs. It was reduced to this level only after the inclusion of a Sola voltage-regulating transformer between the a.c. line supply and the linear amplifier and scaling equipment; careful shielding and grounding of the signal lines were also required.

The diffractometer geometry is described in Chapter III. D. The $1/6^{\circ}$-divergence slit was used in all the experimental runs.

3. Counting Strategy

The fixed-time counting strategy was employed in each of the experimental runs. Each diffraction scan consisted of 100 second counts at the following angles of measurement (in 2θ): every 1/2 degree between 3 and 110 degrees, whole degree intervals between 110 and 150 degrees, and 1/8-degree intervals over selected ranges surrounding strong beryllium diffraction peaks. The fine grid near

the peaks was required because of the absorption-induced shift in the beryllium peaks with sample in the cell (see Chapter III. D. 2). At large angles the measurements were taken at the larger intervals in the interest of conserving time; since little diffraction structure was present, the coarse grid was sufficient to define the scattering curves. The intervals in each case were taken in equal angular incre- ments rather than equal S increments (normally done for conven- ience in integrating the Fourier transform) because the automatic stepping device for advancing the detector could only operate in this manner. For this same reason all the computer programs for processing the data were written for data taken in equal angular increments. As a result of this procedure and of the fixed-time strategy, the relative error of the diffraction scans was a function of angle. Error evaluation and the method used for obtaining a final diffraction pattern are discussed in Chapter VII. C.

The accumulated counts from several diffraction scans were combined to obtain an average intensity for each diffraction angle. The use of several independent scans of short duration permitted a check on the reproducibility of the data. This method compensated for instabilities in the electronic equipment which were otherwise not detectable.

The stability of the electronic components associated with x-ray production and detection was checked at regular time intervals during each experimental run. This was done by recording the scattered intensities at a prescribed angle. The check point angle,

$2\theta = 74^O$, was selected because of the absence of any pronounced structural features in either the beryllium powder or the liquid diffraction patterns. During the 30-hour runs, ten consecutive 100-second counts were taken every three to four hours. Average intensities for the check point angle were approximately 16 and 17 counts per second for the evacuated cell and cell plus sample, respectively. The ratio of the empty and full cell intensities was used to normalize the individual runs to each other according to the procedure described in the next section.

Even under the most stable operating conditions the check point intensities fluctuated about an average value. This behavior was due primarily to the statistical fluctuations occurring in the production of the x rays in the x-ray tube. This process can be described by a Poisson distribution.[58] Since the counting times in this experiment were sufficiently long, the Poisson distribution could be approximated by a normal distribution for convenience in calculations. Confidence intervals of the data about the estimated mean could then be calculated. For each run the check point intensities exhibited statistical behavior which conformed closely to the expectations for a normal distribution. The following example is illustrative of the check point behavior.

In order to assure that the sampling technique described above did not conceal any short-term instabilities in the electronic equipment, consecutive 100-second check point measurements were made for a period of seven hours. Of the 270 measurements, 86% fell within the 90% confidence interval about the mean. There were no

discernible short-term periodic fluctuations of the data. Out of the

three 1000-second samplings at the beginning, middle, and end of

that data, 83% of the points were within the 90% confidence interval.

On this basis, the sampling technique used during the experimental

runs was considered adequate and the stability of the electronic

components was assumed uniform and constant. The check point

data consistently showed slightly more random behavior than was

expected. This was probably due to statistical instabilities and

noise in the detection equipment and to the finite resolving time of

the circuits.

B. The Raw Intensity Data

X-ray diffraction data from liquid argon at $T = -130°$ C were

measured using molybdenum radiation. The angles of measurement

ranged from $2°$ to $150°$ in 2θ; the upper limit corresponds to a maxi-

mum S of 17.1 Å^{-1}. Two complete diffraction scans (see Chapter

VII. A. 3) were made for each of the three densities: 0.9098, 0.9818,

and 1.0052 gm/cm^3. The data from each scan are given as a function

of θ in Table 5. The empty cell data, listed under the heading

ICELL, are the average of four scans between $1°$ and $60°$ and three

scans between $60°$ and $75°$. Table 6 gives the average intensities for

two diffraction scans at one-eighth-degree intervals near strong

beryllium diffraction peaks. Figure 32 shows a graphical illustra-

tion of the average intensities for the density 0.9098 gm/cm^3; data

for the other densities are quite similar. The dashed line was drawn

between the empty cell data points to demonstrate the magnitude of the beryllium powder diffraction pattern. As mentioned in Chapter III. D. 4, the scattering geometry for this data minimized the cell background contribution.

The data in Tables 5 and 6 have been corrected for electrical noise background. In addition, each run has been normalized to a reference intensity for the empty cell. The normalization was necessary because the exact incident beam intensity could not be reproduced for each run. The reference intensity was 18.00 counts per second at the check point angle, $\theta = 37^{\circ}$. The argon runs were normalized from the average empty cell check point intensities taken at the beginning and end of each scan. Full cell check point intensities were taken regularly during the run to monitor the behavior of the electronics. The ratio of the empty to full cell check point intensities was constant from run to run at each density and the ratio also exhibited a monotonic increase with density.

C. The Corrected and Smoothed Sample Intensities

The raw data of Table 5 were corrected[*] according to equation (23) to obtain the diffracted intensities attributed to the sample. Figure 33 illustrates the corrected intensity data for the density, 1.0052 gm/cm^3. The scatter in the corrected data was caused by two different processes: (1) the absorption-induced shift

---

[*] The calculations were performed on the IBM 7090 computer with a program written by R. H. Bigelow.

of the beryllium powder diffraction peaks when sample was present in the cell, and (2) the statistical scatter of the experimental intensities, $I_{c+s}^E(S)$ and $I_c^E(S)$. Correspondingly, two different methods were used to smooth the sample intensity curves. A description of the smoothing procedures follows.

The corrected intensities on and near the strong beryllium powder diffraction peaks lie far outside the statistical spread of the bulk of the data. The anomalous points were reproducible and showed the same general behavior at every strong beryllium peak. This behavior can be attributed to the absorption effect described in Chapter III. D. 2. With sample in the cell the beryllium peak intensities shifted to higher angles. The net effect on the corrected intensities was that the values were too small on the low-angle side of each peak and too large on the high-angle side. The points on the second argon peak in Figure 33 illustrate this behavior; this region corresponds to the angles of the largest beryllium peaks. The fine grid of data taken near the peaks permitted graphical interpolation through this particularly troublesome spot. The points directly on the peaks had to be rejected. The use of fine Soller slits sufficiently reduced the width of the peaks so that very few points were discarded on this basis.

Below θ of 15° the corrected intensities were reproducible, and the resolution of the beryllium peaks was good; this permitted graphical interpolation through spurious points. At higher angles the data were smoothed by a statistical method. After obviously bad

points corresponding to beryllium peaks were rejected, a second order polynomial in θ was fitted by a least square technique to short sections of the data. At any angle the smoothed point is the result of applying the polynomial to a prescribed number of previously smoothed values behind the point (i.e., to intensities at smaller angles) and to the same number of unsmoothed points ahead of the point. At the conclusion of the calculation for a particular angle, the range was shifted by one interval and the process repeated. The range was selected to include features of the curve which a second-order polynomial could adequately represent. On this basis the sample intensity curve above 15° was divided into two sections. The first, between 15° and 40°, was smoothed by a polynomial fitted to twenty data points $(\theta \pm 2.5^{\circ})$ at a time. The remainder was smoothed with a forty-point range $(\theta \pm 5.0^{\circ})$. The dotted curve through the data points of Figure 33 is the result of the preliminary smoothing.

The final estimate of the intensity curve was obtained by constructing a confidence interval about the dotted curve and replacing the data points outside the interval with preliminary smoothed points. This was done because the inclusion of the badly scattered points in the smoothing process unduly influenced the position of the resultant curve. The remaining points were then smoothed by the same polynomial method just described. The calculation of the confidence interval is described below.

With the assumption that the sample intensities at any angle

are normally distributed, the confidence interval may be calculated from the formula [59]

$$\Delta I_s(S) = \pm k_r \left[Var (\chi_s) \right]^{1/2} \qquad (27)$$

where $Var(\chi_s)$ is the variance of χ_s, a random variable representing the sample intensity; and k_r is a constant determined by the significance level chosen for the particular application. This equation states that for a sufficiently large number of observations of the random variable, χ_s, r % of them will lie within the range $\pm \Delta I_s$ about the true mean of the sample intensity, $I_s(S)$.

The experimentally observed quantities are the total number of counts from the cell, n_c, and from the cell plus sample, n_{c+s}. Therefore, the variance of χ_s must be expressed in terms of the random variables η_c and η_{c+s}, which represent the experimentally observed counts. Introduction of these variables into equation (23) with the definition, $Var (\chi_s) = E\{\chi_s - I_s\}^2$, leads to the result[*]

$$Var (\chi_s) = \frac{(1/PGASSC)^2}{\tau_{c+s}^2} Var (\eta_{c+s})$$

$$+ \frac{(1/PGASSC)^2(ACSC/ACC)^2}{\tau_c^2} Var (\eta_c) \qquad (28)$$

where τ is the total counting time at the particular observation angle. The random variables η_c and η_{c+s} conform to a Poisson

---

[*]Equations (28) and (29) were derived by P. G. Mikolaj. His thesis[42] may be consulted for the details.

distribution;[60] and, for this type of distribution, the variance is equivalent to the mean. Finally, introducing the experimental quantities, $\tau_{c+s}I_{c+s}{}^{E}$ and $\tau_{c}I_{c}{}^{E}$, as the best estimates of the means of η_{c+s} and η_{c} gives

$$\text{Var } (\chi_{s}) = \frac{(1/\text{PGASSC})^{2}}{\tau_{c+s}}\left[I_{c+s}{}^{E}(S) + \frac{\tau_{c+s}}{\tau_{c}}\left(\frac{\text{ACSC}}{\text{ACC}}\right)^{2}I_{c}{}^{E}(S)\right]$$

(29)

This equation may then be combined with equation (27) for the calculation of the confidence interval.

The confidence interval at the 90 % significance level ($k_{r}=1.645$) was calculated at several values of θ and placed around the dotted line of Figure 33; the dashed lines represent the limits of the interval above and below the curve. For this set of corrected intensities, 84% of the points fell within the interval; 85% and 87% fell within similar bands for the other two densities. Data points outside the bands were discarded and replaced with points from the preliminary smoothed curve.

The final estimate of the sample intensity curve was then obtained by smoothing the points by the polynomial method. Figure 34 shows the smoothed intensity curve as a function of θ for the data of Figure 33. The curve has been normalized to the independent scattering curve, $f_{d}^{2}(S) + I^{inc}(S)$, at $S = 10 \text{ Å}^{-1}$.

A more sensitive method of illustrating the sample intensity curves is a plot of the ratio of the sample scattering to the indepen-

dent scattering. The smoothed intensity curves for each of the three

states are given in this form in Figure 35. The apparently smooth

features of the previous figure now appear in a magnified form,

especially at large values of S. This permits the identification of

spurious intensity peaks which would introduce error into the radial

distribution function.

The first four peaks appear in regular positions for each

state. However, beyond $S = 10 \text{ Å}^{-1}$, there is no correlation of the

peak positions or magnitudes from state to state. Coupled with the

fact that liquid scattering curves generally have monotonically

decreasing peak heights with S, the validity of the recognizable peaks

at larger S values is questionable. The high relative error of the

corrected intensity data in this region lends support to this assertion.

For the three states, the average relative error (given by

$\Delta I_s/\text{Mean } I_s$) was 5% at $\theta = 15°$, 9% at $30°$, 16% at $50°$, and 17% at

$75°$ at the 90% significance level. No attempt was made to evaluate

the relative error of the smoothed curve through the data points.

Table 7 gives a summary of the characteristic features of the

sample intensity curves. The positions of the peaks agree reasonably

well with those given by Eisenstein and Gingrich[56] for argon at

$- 129°$ C and $\bar{\rho} = 0.87 \text{ gm/cm}^3$. The ratios of the first peaks to the

continuum intensity at $S = 8.8 \text{ Å}^{-1}$ also show fair agreement. The

position of the first peak was determined from the $I_s(S)$ vs. θ curves;

all others were taken from Figure 35.

Each intensity ratio curve in Figure 35 appears to oscillate

about a line with negative slope. Since this ratio is a sensitive method of testing the normalization fit of the intensity data, the line should have zero slope. The slopes were more nearly linear when the intensity ratio was plotted as a function of θ. The best estimated straight lines gave negative slopes of 0.0024, 0.0034, and 0.0036 (counts per second per electron unit per degree) with increasing density. Because of these slopes the integral normalization method (Chapter VI. F) failed to give satisfactory normalization factors. The integral method factors oscillated with rapidly damping amplitude about a line that was roughly parallel to, but slightly higher than, the line through the ratio curves.

The monotonic change in slope of the ratio curves with density suggests that there may be a systematic error in the data reduction process. However, a thorough examination of all the corrections failed to disclose anything of the magnitude corresponding to this effect. The effect of this phenomenon on the Fourier transforms is examined in the next Chapter.

VIII. ARGON RADIAL DISTRIBUTION FUNCTIONS

A. Electronic and Atomic Radial Densities

When written in terms of the radial atomic density $\rho_a(r)$, equation (2) takes the form

$$4\pi r^2 \left(\rho_a(r) - \overline{\rho}_a\right) = \frac{2r}{\pi} \int_0^{S_m} Si(S) \sin Sr \, dS \qquad (30)$$

where the kernel of the integral is given by equation (24),

$$i(S) = \frac{C\left[I_s(S) - I_o(S)\right] - NI_s^{inc}(S)}{Nf_s^2(S)} - 1 \qquad (24)$$

The substitution of S_m, the maximum experimental value of S, for the infinite upper limit of the integral introduces a truncation error. This error will be discussed below.

Although derived independently, an equation for the electronic radial density $\rho_e(r)$ may be written in the similar form[10]

$$4\pi r^2 \left[\rho_e(r) - \overline{\rho}_e - \rho_o(r)\right]$$

$$= \frac{2r}{Z\pi} \int_0^{S_m} Si(S) f_s^2(S) \sin Sr \, dS \qquad (31)$$

where Z is the atomic number of the sample. The quantity $\overline{\rho}_e$ is the average electronic density of the system, and $\rho_o(r)$ is the average electron density within the reference atom. This latter quantity was arbitrarily included to strengthen the convergence of the transform; its influence is confined to radii less than a nominal atomic radius.

Equations (30) and (31) are in effect two different ways of

illustrating the transform of the sample intensity data. They are more useful than the conventional displays of $4\pi r^2 \rho(r)$ in that they clearly show the ghost peaks or ripples superimposed on the density curve. The effect of having the term $f_s^2(S)$ in the integral for the radial electronic density is to decrease the relative importance of sample intensity values at large S. Therefore, a comparison of the electronic with the atomic density distributions is useful in interpreting the reliability of the data.

The transforms were evaluated at one-tenth Angstrom intervals out to $r = 15 \overset{\circ}{A}$. [*] The electronic and atomic radial densities are shown in Figures 36 and 37, respectively. The three curves in each figure correspond to integration of the intensities illustrated in Figure 35. The integrals were truncated at $S_m = 9 \overset{\circ}{A}^{-1}$; this is believed to be near the limit of the validity of the experimental data. Truncations at larger values of S introduced such large ripples on the general shape of the atomic distribution curves that their identity began to disappear.

The ripples are most obvious in the atomic distributions of Figure 37. The period of the oscillations is approximately the same for each state; this suggests that a general feature of each intensity curve, rather than discrete errors, is responsible for the effect. Truncations of the transform at several values of S between 2π and 15 showed similar features. At each truncation limit the curves

---

[*] The calculations were performed on an IBM 7090 computer with a program written by R. H. Bigelow.

for all three states had oscillations imposed on curves of the same general shape. The periods were roughly constant at $2\pi/S_m$, and the amplitudes increased with increasing S. Figure 38 shows the atomic radial distributions for the argon density 0.9098 gm/cm^3 with truncation limits of 2π, $5/2\ \pi$, and 9Å^{-1}.

First estimates for the normalization factors were chosen for each truncation limit by examination of the intensity ratio curves of Figure 35. The normalization factors were then altered by a trial and error iteration until one was found which produced oscillations of minimum amplitude on the atomic distribution curves. The first estimates were usually good to within 2%.

The most likely cause of the ripples common to all the density distributions is the general slope of the intensity ratio curves of Figure 35. Until the intensity data is corrected to the point that the normalization factors are constant with S and agree reasonably well when estimated by different methods, the isolation of specific errors in the intensity patterns cannot be performed. Several attempts to do this with empirical correction functions were not successful.

B. Atomic Radial Distribution Functions

The atomic radial distribution function is given by rearrangement of equation (30):

$$g_a(r) \equiv \frac{\rho_a(r)}{\overline{\rho}_a} = 1 + \frac{1}{2\pi^2 r \overline{\rho}_a} \int_0^{S_{max}} Si(S) \sin Sr \, dS \qquad (32)$$

As before, i(S) is given by equation (24).

The best estimates of the atomic radial distribution functions were obtained by superposition of the transforms with truncations of S_{max} = 2π, $5/2\pi$, and 9 Å^{-1}. An envelope was then drawn about the amplitudes of the oscillations resulting from the various truncations. The results are shown in Figure 39. The true radial distribution function for each state is believed to lie within the band shown.

Only two well defined peaks occur in each of the distribution functions at this temperature. The peaks increase in sharpness with increasing density and are located at successively smaller values of r. In spite of the diffuse band defining the limits of the function, it can be said that the short-range order of liquid argon at these conditions does not extend significantly beyond 15 Å.

C. Coordination Numbers and Shell Distances

The coordination numbers, often referred to as nearest-neighbor shells, are the average number of particles included under the peaks in the distribution curve. Shells containing atoms which are located at successively larger radii are designated as the first, second, third, etc. Since individual shells are not necessarily separated and distinct, they will generally overlap. If the radial density is defined with sufficient accuracy, the consecutive shells can be obtained by subtracting the inner shells. In order to do this, each shell is assumed symmetrical about its maximum. Considerable controversy exists in the method of symmetrizing the shells. While some authors simply symmetrize the peaks in the $4\pi r^2 \rho(r)$ vs. r

curve and integrate to obtain the coordination numbers, Coulson and Rushbrooke[61] present arguments favoring a symmetrical reflection about the maxima of the curve $r\rho(r)$. In this latter method, the symmetrical curve in $r\rho(r)$ is replotted and integrated in $4\pi r^2\rho(r)$. The results from both of these methods were obtained.

Except for the region near the maxima, the small r-side of the first peaks in the distribution functions of Figure 39 are all well defined. Coordination numbers beyond the first were not attempted because of the uncertainties in the functions. The results of the calculations are given in Table 8. As the radius of the first shell becomes smaller with increasing density, the first coordination number decreases. The discrepancy of the coordination numbers calculated by the two methods varies from 8 to 18%. The positions of the peaks were estimated from curves of the type shown in Figure 38.

The first shell positions and coordination numbers are slightly larger than would be expected in comparison with those reported by Eisenstein and Gingrich[56] for liquid argon at $-129°$ C and 0.87 gm/cm^3. The positions of the second shells differ quite markedly. Finbak[8] has suggested that the second peak reported by Eisenstein and Gingrich is a spurious peak resulting from experimental error. Finbak recalculated the atomic distribution curve after empirically correcting Eisenstein's intensity data; the result contained a second maximum in good agreement with the present work. The comparison is given in Table 8.

Also listed in the table under r_2/r_1 are the ratios of the

positions of the first two shells. The values for the three states of

the present work are quite close to that obtained from Finbak's

recalculation. In fact, Finbak showed that this ratio is constant to

within 6% for argon and eight other monatomic liquids at various

densities and temperatures. This apparently general feature of liquid

structure has been reproduced from models by Furukawa, [62] Wood

and Parker, [63] and Bernal. [64] In this connection it is significant

that the same approximate magnitude for this ratio is obtained both

from neutron diffraction of argon[65] at 84° K and 1. 40 gm/cm^3 and

also from Finbak's recalculation of Eisenstein's x-ray data for the

same state. The comparison is given in Table 8 also. The fact that

r_2/r_1 from both of Eisenstein's results is internally consistent, yet

different from these other estimations, suggests the presence of a

systematic error in the experiment. The validity of the second peaks

is even more doubtful since the nominal position of the third peak

agrees well with the second peak position from the neutron diffraction

data. While this is not conclusive proof of experimental error in the

earlier x-ray work on argon--the spurious second peak fits within

the estimated band for $g_a(r)$ at 0. 9098 gm/cm^3 of the present work--

it is at least suggestive that the matter should be investigated further.

IX. DISCUSSION AND RECOMMENDATIONS

The supporting equipment designed and developed for the present work has performed satisfactorily. The cryostat can be used with a variety of sample cells in either the parafocusing or Debye-Scherrer geometries. Because of the low x-ray scattering power characteristic of fluids, the low absorption of incident and scattered radiation is a particular asset. Similarly, high angular resolution is obtained without the severe losses in intensity accompanying large sample-to-counter distances. If the flexibility of having the diffraction geometry adaptable to parafocusing experiments could be sacrificed, the vacuum chamber and cell assembly could be made smaller; this would permit the detector to be positioned more closely to the sample. Since the diffracted intensities are inversely proportional to the square of the sample-to-counter distance, the advantage would be considerable. With such an arrangement the beam collimation would have to be improved even further. An improved design for Soller slits which could accomplish this is presented in Proposition II.

The positioning of the incident beam is an important factor in optimizing the scattering efficiency from the partially exposed cell. The arrangement used in this experiment represents an optimum choice in many respects. However, the presence of the large amounts of cell scattering is quite undesirable. This problem could be eliminated by confining the intersection of the incident and scattered

beams to within the sample volume. This is difficult with high
pressure cells of the present diameter because of the very narrow
beams required. Even if sufficiently narrow beams could be well
defined, the scattered intensities would become impracticably small.
On the other hand, a beryllium cell large enough to permit a large
irradiated sample volume could not accommodate high pressures.
A stronger cell material such as diamond or laminated plastic might
be considered. One interesting possibility would be the use of a
plastic sheath on a thin-walled beryllium cell of larger diameter.
With proper selection of the plastic according to its thermal expan-
sion, a sheath could be designed that would form a prestressed cell
at low temperatures. Such a cell would stand higher pressures than
one of beryllium with comparable wall thickness; yet the total absorp-
tion of x rays in the cell walls would remain small.

The present temperature and pressure instrumentation are
adequate for experiments not too close to the critical state. Tem-
perature control could be improved by installation of a second
platinum resistance element in the temperature control annulus.
Since the change in resistance with temperature is large for this
element, its use in place of the absolute control thermocouple would
permit more rapid control response and provide an order of magni-
tude greater temperature sensitivity. The sample temperature can
be measured accurately by careful determination and control of the
cell temperature gradients at the desired control temperature.

For experiments at the critical state better pressure control

would be necessary. Finer control could be achieved with an automatic system in which the output voltage from the pressure transducer would drive a servomechanism attached to the existing injector. With automatic control the pressure fluctuations should be able to be reduced to as low as ± 0.001 psi. Methods for utilizing the sensitivity of the pressure transducer more efficiently are discussed in Appendix III. With better control, the limitation in pressure measurement would then be that of the Michel pressure balance, about 1:10,000.

The high counting efficiency of the scintillation counter makes it desirable for achieving a large signal to noise ratio and shortened operating times for experiments. However, the relatively poor energy resolution of this type of counter is a characteristic which should not be lightly disregarded. A comparison should be made between crystal-monochromated radiation and the arrangement used in the present work. Poor monochromatization, however, is not believed to be the spectre behind the anomalous slope of the argon diffraction data. The scintillation counter used with the pulse height analyzer and Kβ filter has yielded good results in other experiments in our laboratory. However, experience with this technique is not yet extensive enough to verify that it provides sufficient monochromatization at very large values of S.

Several corrections to the experimentally observed intensity data have been discussed in the text. The largest correction, that due to the absorption of incoherent scattering in the Kβ filter, can be eliminated by repositioning the filter in the incident beam. With

the present scattering geometry, the remaining corrections related to incoherent scattering are relatively small. The techniques developed for treating them can be applied to all experiments with highly absorbing samples.

Sample or cell absorption of the incoherent scattering could be very significant in many cases, and the presence of this phenomenon should not be ignored. The optimum geometry for minimizing this effect is a narrow beam positioned near the top of the sample, but for small cells this often requires an incident beam of nonuniform intensity. The composite beam technique was developed for the solution of this particular problem, but the method can be extended to other experiments involving beams of nonuniform intensity.

A recent experiment in the laboratory has demonstrated the validity of the smoothing technique which was applied to the argon sample intensities. The fine structure of the intensity curve for silica was recovered by using the same methods.[*] The silica data had less scatter in the region of large S, however. The relative error of the argon data in this region should be reduced before attempting to include it in the Fourier transform.

The corrected sample intensity data for argon did not normalize satisfactorily to the independent scattering curve. As a result, the radial distribution functions contain spurious ripples and

---

[*]The details of the silica analysis will be given in the thesis of P. G. Mikolaj.[42]

can only be estimated within the limits of those oscillations. Before greater resolution can be obtained, the normalization criteria must be more nearly satisfied.

The normalization constants for the argon data appear to be a linear function of the scattering angle. A definitely linear fit has been observed in the silica experiment; the scattering from an exposed silica rod was compared with the corrected intensities for the rod contained in the beryllium cell. The most likely cause of the slope induced by the presence of the cell is non-isotropic scattering power of the beryllium powder. Combined with the strong sample absorption, this could account for the monotonic change in slope of the argon data with increasing density. Further studies should be made with a reference such as silica to establish criteria for suitable normalization functions. Application of this correction to the argon data would result in radial distribution functions of greater resolution.

A check on the hypothesis that cell anisotropy is the source of error could be made by performing the experiment with silica in a single crystal beryllium cell--a single crystal cell for use at low pressures is available in the laboratory. Reproduction of the pattern from the exposed rod would validate the scattering and absorption corrections. If the hypothesis is confirmed, an alternative to the normalization correction for the powdered beryllium cell would be the development of an isotropic cell. Single crystals of beryllium or amorphous materials such as high strength plastics offer the most promising qualities.

The common features of the argon distribution functions
suggest the possibility that previous work on argon contains spurious
sub-peaks which are the result of systematic error. The results
from neutron diffraction of argon near the triple point support this
possibility with even stronger evidence. Since the previous x-ray
work is widely referred to, a check on its general validity should
be made by conducting studies near the states previously done. The
same states should not, however, be repeated for their own sake.
Future work should expand along the grid of isotherms and isochores
initiated with the present study. The radial distribution functions
from such a grid will provide the most useful information for investi-
gation of the structure of liquids.

TABLE 1

CALIBRATION FOR THERMOMETER NO. 2

Run Number	Calibration Temperature $T_C(^oK)$	Measured Resistance R_C(ohms)	Interpolated Resistance X_T(ohms)	Temperature Difference* $\triangle T(^oC)$
(1)	(2)	(3)	(4)	(5)
7	77.715	20.291	......	0.000
6	78.890	20.792	20.7892	0.007
12a	128.282	41.693	41.6712	0.053
12b	138.238	45.828	45.8012	0.065
12c	153.598	52.157	52.1263	0.075
9	201.435	71.536	71.5166	0.048
10	206.907	73.730	73.7090	0.053
11	217.076	77.790	77.7712	0.048
8	273.015	99.871	......	0.000
4b	273.285	99.976	99.9729	0.008
13	298.789	109.921	109.9219	-0.002

* $\triangle T = T_C$ (measured) $- T_T$ (interpolated)

TABLE 2

COMPARISON OF PRESSURE COEFFICIENT
FOR THERMOMETER AND PURE PLATINUM

T (°K)	$\frac{1}{R} \frac{dR}{dP} \times 10^6 \left(\frac{cm^2}{kg} \right)$	
	Thermometer	Pure Platinum
77	10.3	....
90	....	2.34
150	5.8	....
191	6.3	....
195	....	1.97
273	8.4	1.93

TABLE 3

CORRECTIONS FOR LOSSES OF INCOHERENT SCATTERING,
ARGON CONFINED IN PARTIALLY IRRADIATED BERYLLIUM CELL

Theta	δ_s (Eq.15)	t_f^{inc} (Eq.17)	t_{PHS}^{inc} (Eq.18)	$A_{s,sc}^{inc} / A_{s,sc}^{coh}$ (Eq.15)			G(s) (Eq.16)		
				0.9098 (gm/cm³)	0.9818 (gm/cm³)	1.0052 (gm/cm³)	0.9098 (gm/cm³)	0.9818 (gm/cm³)	1.0052 (gm/cm³)
0.0	1.0000	1.0000	1.0000	1.00000	1.00000	1.00000	1.0000	1.0000	1.0000
5.0	0.98864	0.9969	1.0000	0.99936	0.99907	0.99896	1.0000	1.0000	1.0000
10.0	0.9958	0.9936	1.0010	0.99685	0.99639	0.99625	1.0000	1.0000	1.0000
15.0	0.9069	0.9861	1.0017	0.99423	0.99377	0.99363	0.9983	0.9982	0.9982
20.0	0.8601	0.9758	1.0026	0.99161	0.99096	0.99074	0.9957	0.9956	0.9956
25.0	0.8185	0.9631	1.0033	0.98908	0.98822	0.98794	0.9918	0.9918	0.9917
30.0	0.7750	0.9482	1.0035	0.98649	0.98452	0.98508	0.9860	0.9859	0.9858
35.0	0.7262	0.9325	1.0028	0.98403	0.98277	0.98237	0.9780	0.9776	0.9776
40.0	0.6733	0.9154	1.0015	0.98142	0.97996	0.97948	0.9761	0.9666	0.9664
45.0	0.6181	0.8982	0.9993	0.97849	0.97680	0.97625	0.9533	0.9527	0.9525
50.0	0.5639	0.8812	0.9960	0.97509	0.97313	0.97250	0.9369	0.9361	0.9358

TABLE 3 (Cont'd)

Theta	δ_s (Eq.15)	t_f^{ino} (Eq.17)	t_{PHS}^{ino} (Eq.18)	$A_{s,so}^{ino} / A_{s,so}^{coh}$ (Eq.15)			$G(s)$ (Eq.16)		
				0.9098 (gm/cm3)	0.9818 (gm/cm3)	1.0052 (gm/cm3)	0.9098 (gm/cm3)	0.9818 (gm/cm3)	1.0052 (gm/cm3)
55.0	0.5133	0.8645	0.9921	0.97096	0.96369	0.96795	0.9183	0.9174	0.9171
60.0	0.4686	0.8489	0.9878	0.96615	0.96350	0.96265	0.8990	0.8978	0.8974
65.0	0.4317	0.8357	0.9834	0.96071	0.95766	0.95667	0.8803	0.8789	0.8784
70.0	0.4054	0.8237	0.9791	0.95417	0.95062	0.94947	0.8626	0.8609	0.8603
75.0	0.3837	0.8146	0.9755	0.94679	0.94269	0.94136	0.8475	0.8455	0.8449

TABLE 4

COMPOSITE BEAM ABSORPTION FACTORS

FOR ARGON CONFINED IN A PARTIALLY IRRADIATED BERYLLIUM CELL

Theta	Argon Density (gm/cm³)								
	0.9098			0.9818			1.0052		
	GASSC	ACC	ACSC	GASSC	ACC	ACSC	GASSC	ACC	ACSC
0.0	0.21265	0.65987	0.21934	0.19386	0.65987	0.20170	0.18813	0.65987	0.19630
5.0	0.23326	0.65607	0.29040	0.21431	0.65607	0.27480	0.20852	0.65607	0.27000
10.0	0.25429	0.65325	0.37228	0.23540	0.65325	0.36027	0.22960	0.65325	0.35657
15.0	0.27451	0.65429	0.41582	0.25587	0.65429	0.40598	0.25011	0.65429	0.40295
20.0	0.29256	0.65745	0.43258	0.27431	0.65745	0.42348	0.26866	0.65745	0.42069
25.0	0.30714	0.66108	0.44003	0.28935	0.66108	0.43117	0.28384	0.66108	0.42845
30.0	0.31725	0.66440	0.44401	0.29992	0.66440	0.43519	0.29454	0.66440	0.43248
35.0	0.32274	0.66686	0.44678	0.30581	0.66686	0.43796	0.30061	0.66686	0.43527
40.0	0.32418	0.66828	0.44864	0.30761	0.66828	0.43984	0.30247	0.66828	0.43715
45.0	0.32224	0.66875	0.44975	0.30601	0.66875	0.44098	0.30098	0.66875	0.43829
50.0	0.31739	0.66836	0.45030	0.30151	0.66836	0.44157	0.29658	0.66836	0.43889

TABLE 4 (Cont'd)

Theta	Argon Density (gm/cm^5)								
	0.9098			0.9818			1.0052		
	GASSC	ACC	ACSC	GASSC	ACC	ACSC	GASSC	ACC	ACSC
55.0	0.30996	0.66704	0.45036	0.29447	0.66704	0.44167	0.28944	0.66704	0.43901
60.0	0.30042	0.66471	0.44993	0.28529	0.66471	0.44133	0.28060	0.66471	0.43869
65.0	0.28919	0.66155	0.44901	0.27445	0.66155	0.44049	0.26988	0.66155	0.43789
70.0	0.27635	0.65809	0.44706	0.26198	0.65809	0.43870	0.25752	0.65809	0.43613
75.0	0.26259	0.65509	0.44263	0.24858	0.65509	0.43452	0.24428	0.65509	0.43204

TABLE 5

SUMMARY OF DIFFRACTION DATA,
INTENSITIES (counts/second) FOR EVACUATED BERYLLIUM CELL
AND BERYLLIUM CELL CONTAINING LIQUID ARGON[*]

Molybdenum Radiation, 55 KV, 20 ma,

Zirconium Filter, 50% PHA Transmission

All Intensities Corrected to 18.00 cps for θ = 37.00 Degrees

[*]ICELL designates evacuated beryllium cell intensity.

A, B designate individual diffraction scans.

Note: This page is a dense numerical data table (rotated 90°) consisting of two side‑by‑side blocks. The columns in each block are: THETA, ICELL, and CELL PLUS SAMPLE INTENSITY (reported at three densities — 0.9098 GM/CM³, 0.9818 GM/CM³, and 1.0052 GM/CM³ — each with sub‑columns A and B).

Left block (THETA 1.00 – 13.25)

THETA	ICELL	0.9098 A	0.9098 B	0.9818 A	0.9818 B	1.0052 A	1.0052 B
1.00	4.350	30.900	30.710	23.290	22.070	21.440	22.240
1.25	4.150	27.810	27.590	21.200	20.700	19.870	19.690
1.50	4.710	25.980	25.080	20.830	19.730	19.870	18.780
1.75	5.000	25.000	24.190	20.360	19.810	19.490	19.710
2.00	5.490	24.980	24.050	20.820	19.190	20.210	19.240
2.25	5.520	24.090	23.930	20.210	20.330	20.530	20.990
2.50	6.270	24.660	23.890	21.210	19.650	20.830	20.520
2.75	7.030	25.340	24.570	20.920	21.020	20.530	21.250
3.00	7.400	26.230	26.090	22.780	22.170	21.940	21.550
3.25	8.130	26.950	28.810	24.600	23.770	23.630	23.630
3.50	9.570	29.920	29.950	26.630	26.370	25.740	24.610
3.75	10.000	33.560	33.660	28.930	29.850	28.710	28.370
4.00	10.760	38.560	37.260	32.970	33.460	33.680	33.350
4.25	11.160	41.830	43.930	38.570	37.050	36.000	37.170
4.50	11.950	48.810	48.900	44.540	44.500	42.700	42.890
4.75	11.880	55.420	54.520	52.940	51.510	47.940	50.360
5.00	12.630	63.500	63.880	59.300	58.540	58.710	58.520
5.25	14.890	72.840	74.950	69.910	68.900	68.560	69.190
5.50	17.650	84.680	84.380	81.510	79.340	80.340	81.360
5.75	14.420	89.880	89.880	91.710	89.370	89.370	91.210
6.00	14.640	93.790	92.900	93.850	90.770	95.340	94.310
6.25	15.490	90.300	91.580	91.580	88.570	92.340	91.930
6.50	15.480	86.500	87.710	85.370	82.450	86.920	87.470
6.75	16.500	77.860	78.490	78.740	75.520	79.820	80.730
7.00	16.430	72.150	71.800	70.580	68.250	71.910	70.240
7.25	17.640	66.040	65.160	62.290	60.760	63.110	65.420
7.50	17.840	59.150	59.080	58.460	57.510	58.800	58.100
7.75	19.330	54.900	56.690	55.390	52.460	54.520	53.030
8.00	19.030	51.900	53.250	51.640	49.160	0.280	49.360
8.25	21.060	49.220	47.780	48.310	47.550	46.570	46.180
8.50	22.360	49.060	49.780	46.550	46.220	45.350	47.570
8.75	21.070	47.680	48.590	46.650	46.190	45.390	47.390
9.00	28.320	45.730	46.240	43.110	43.780	43.850	44.120
9.25	25.700	50.050	48.840	47.650	47.230	45.770	46.260
9.50	28.260	48.840	48.430	47.250	45.500	47.040	45.900
9.75	29.440	49.660	50.040	47.260	46.890	46.380	45.770
10.00	127.310	104.580	103.060	101.240	102.780	90.220	93.150
10.25	27.470	51.610	50.450	48.150	48.540	47.300	47.590
10.50	25.970	49.200	49.200	47.910	48.610	47.050	47.600
10.75	35.490	55.620	52.920	51.970	52.820	52.100	52.550
11.00	138.360	106.940	106.670	110.370	100.130	3.510	83.450
11.25	64.240	75.330	74.500	70.050	72.090	73.750	74.130
11.50	461.060	317.660	317.870	300.520	308.030	272.020	274.780
11.75	43.930	60.390	61.110	59.110	57.230	57.890	56.620
12.00	40.070	56.510	54.880	55.160	54.260	52.830	54.360
12.25	38.970	54.040	53.380	53.450	52.510	52.130	52.650
12.50	38.710	52.630	51.410	51.410	51.350	50.650	50.800
12.75	35.460	51.630	49.930	47.260	47.000	47.820	48.360
13.00	34.950	48.460	49.930	46.640	44.680	46.150	45.560

Right block (THETA 13.50 – 25.75)

THETA	ICELL	0.9098 A	0.9098 B	0.9818 A	0.9818 B	1.0052 A	1.0052 B
13.50	32.330	46.540	46.180	44.110	44.150	43.810	45.320
13.75	30.400	44.370	46.180	43.700	42.830	43.100	43.430
14.00	29.400	42.060	40.630	40.630	39.750	41.450	39.650
14.25	28.410	41.850	42.310	41.500	39.160	40.420	38.400
14.50	28.130	41.620	40.780	40.510	39.110	38.590	38.010
14.75	27.950	40.590	40.780	40.590	38.140	38.850	38.390
15.00	28.700	40.810	40.310	39.670	38.400	40.730	38.420
15.25	36.490	43.930	44.250	42.230	41.510	69.210	41.170
15.50	75.640	73.360	73.360	70.440	70.610	36.810	69.170
15.75	27.100	39.170	39.170	37.510	37.890	36.920	36.710
16.00	27.110	38.560	38.440	37.870	36.310	36.600	38.010
16.25	26.610	39.770	38.440	37.080	37.110	37.780	35.940
16.50	29.090	40.590	40.790	38.820	37.530	36.060	39.070
16.75	27.240	39.730	40.790	36.990	37.450	35.450	36.910
17.00	25.820	36.590	37.460	36.070	35.200	35.310	35.850
17.25	25.490	37.550	37.460	36.100	35.260	35.870	34.920
17.50	27.050	37.920	37.630	36.500	35.900	36.150	35.980
17.75	28.990	39.550	38.860	37.890	36.760	64.470	35.830
18.00	88.710	79.600	79.600	76.380	72.300	37.940	63.150
18.25	29.170	39.410	38.760	38.860	36.370	35.050	38.640
18.50	26.290	37.810	35.980	35.580	34.120	33.610	36.380
18.75	25.690	35.560	35.980	34.730	34.140	33.950	34.420
19.00	26.070	35.480	35.380	34.380	33.390	33.810	33.060
19.25	26.560	35.690	35.980	34.570	33.810	31.480	34.610
19.50	25.630	34.270	34.250	33.470	33.670	34.210	34.040
19.75	28.000	34.330	34.250	35.680	33.710	93.450	34.860
20.00	30.040	36.560	36.870	36.190	34.310	34.950	96.930
20.25	121.480	105.490	36.870	95.930	97.840	35.570	35.060
20.50	29.130	35.380	35.620	34.760	33.850	33.900	32.170
20.75	27.430	34.330	35.620	33.190	33.130	29.620	38.090
21.00	34.830	39.410	38.390	36.630	37.250	61.400	34.450
21.25	30.720	35.530	35.970	34.490	33.660	35.790	60.570
21.50	76.560	70.560	70.240	70.260	59.830	30.470	62.110
21.75	100.740	69.700	69.700	64.000	62.550	31.620	36.450
22.00	31.880	38.370	36.680	37.250	35.410	32.000	31.520
22.25	26.260	34.110	36.680	32.950	33.440	39.270	32.300
22.50	28.230	32.850	33.570	33.050	31.930	33.020	32.040
22.75	28.020	33.090	33.570	33.700	31.620	29.620	41.770
23.00	27.150	32.800	33.440	32.250	32.000	32.150	41.130
23.25	41.420	41.970	33.440	40.080	42.440	28.770	33.060
23.50	28.320	31.900	32.890	32.180	32.360	29.110	30.810
23.75	26.290	31.730	32.890	31.580	30.380	27.700	30.690
24.00	28.690	30.890	32.670	30.890	31.070	28.690	32.210
24.25	30.520	35.420	32.670	33.090	32.640	27.990	29.390
24.50	25.720	29.820	30.120	29.900	29.300	29.670	29.110
24.75	25.250	29.490	30.120	30.260	28.980	29.150	29.670
25.00	25.280	28.980	28.440	28.810	29.150	29.290	27.860
25.25	24.420	29.470	28.440	28.570	29.290	28.110	27.870
25.50	24.790	30.260	29.990	28.570	28.110	27.990	27.990
25.75	33.070	35.140	29.990	34.280	33.220	33.360	35.140

CELL PLUS SAMPLE INTENSITY (left table)

THETA	ICELL	0.9098 GM/CM³ A	B	0.9818 GM/CM³ A	B	1.0052 GM/CM³ A	B
26.00	24.720	30.350	28.300	28.150	28.180	27.610	28.680
26.25	24.150	28.510	28.300	27.400	27.530	26.080	27.470
26.50	24.020	28.140	28.500	26.920	26.500	27.180	26.510
26.75	23.510	28.010	28.500	26.330	26.800	26.560	26.540
27.00	23.500	27.310	27.880	27.000	25.890	26.140	26.090
27.25	23.010	26.940	28.170	26.730	26.980	26.160	25.540
27.50	23.520	27.440	28.170	26.680	26.670	24.610	27.010
27.75	32.470	34.950	34.950	32.480	33.300	32.890	33.140
28.00	23.850	26.860	27.610	27.160	25.770	27.150	26.340
28.25	26.460	28.860	27.610	28.370	28.380	27.190	27.610
28.50	24.100	26.510	26.670	26.080	27.560	25.380	26.260
28.75	23.870	26.420	27.240	25.820	26.680	25.350	25.130
29.00	33.410	32.790	32.790	33.450	32.270	33.460	33.790
29.25	23.370	26.400	27.240	25.850	24.670	24.030	25.080
29.50	21.960	25.130	24.890	24.390	24.590	24.590	24.500
29.75	22.400	25.680	24.890	23.900	24.220	23.690	24.140
30.00	24.920	25.950	26.050	24.530	26.110	24.880	24.880
30.25	28.690	29.450	26.050	29.390	28.010	27.680	28.900
30.50	22.170	25.010	25.170	24.560	23.690	23.910	24.650
30.75	23.590	26.510	25.170	24.340	24.060	23.250	23.170
31.00	23.670	25.680	24.680	24.820	24.500	24.080	25.160
31.25	21.160	23.730	24.680	23.200	22.760	22.720	22.670
31.50	21.260	23.090	24.270	22.820	23.110	22.350	22.870
31.75	28.790	29.460	24.270	29.110	28.750	29.130	28.450
32.00	21.980	25.060	25.230	23.360	24.900	25.110	25.200
32.25	22.460	25.170	25.210	23.550	23.630	24.220	24.150
32.50	24.080	25.630	25.990	24.580	24.230	23.570	24.580
32.75	20.440	22.220	25.990	22.120	22.540	21.840	22.410
33.00	20.210	22.100	22.020	22.250	21.590	21.450	22.090
33.25	19.740	22.470	22.270	21.070	21.210	20.740	20.920
33.50	19.900	21.480	21.810	21.410	21.930	21.790	21.030
33.75	27.040	22.950	21.810	20.660	21.930	21.450	21.340
34.00	20.000	21.020	20.490	20.340	20.540	20.120	20.920
34.25	20.870	22.420	21.360	20.800	20.680	20.740	21.030
34.50	19.440	21.330	21.360	20.340	20.440	20.120	21.340
34.75	27.040	26.910	26.220	25.130	25.430	25.610	25.780
35.00	22.000	22.960	26.220	22.440	23.520	22.510	22.990
35.25	20.870	22.420	21.360	20.800	20.680	21.790	21.940
35.50	19.440	21.330	21.360	21.390	20.440	20.440	20.330
35.75	18.670	20.770	19.860	19.260	19.640	19.230	18.470
36.00	18.350	19.970	19.860	19.490	19.180	19.230	19.340
36.25	18.030	18.920	19.210	19.860	19.410	18.290	19.130
36.50	18.490	19.830	19.210	18.830	19.300	18.440	18.810
36.75	17.800	19.760	20.110	19.010	19.140	18.670	18.980
37.00	17.930	20.300	20.110	19.400	18.530	18.030	19.090
37.25	17.480	19.060	19.020	18.030	18.250	18.080	18.740
37.50	17.620	19.950	19.020	17.930	18.320	18.510	18.500
37.75	18.580	20.140	19.890	17.960	18.970	18.260	18.600
38.00	17.940	18.380	19.890	18.430	18.220	18.080	18.520
38.25	18.570	19.480	19.590	18.850	19.480	17.960	18.800
38.25	20.310	19.080	19.590	19.090	19.280	18.850	19.010

CELL PLUS SAMPLE INTENSITY (right table)

THETA	ICELL	0.9098 GM/CM³ A	B	0.9818 GM/CM³ A	B	1.0052 GM/CM³ A	B
38.50	18.250	18.860	18.720	18.020	18.370	17.410	18.490
38.75	16.630	19.080	18.720	17.600	17.690	16.930	17.940
39.00	16.710	17.570	17.790	16.970	16.880	17.130	16.440
39.25	16.560	17.940	17.790	16.850	16.660	17.380	16.840
39.50	16.830	17.570	17.130	16.930	17.170	16.240	16.550
39.75	16.200	18.020	17.130	17.020	17.480	17.090	17.010
40.00	16.650	17.570	17.310	16.850	16.730	16.450	16.710
40.25	17.230	17.410	17.310	16.960	16.910	17.420	16.740
40.50	17.620	17.090	17.340	16.560	18.020	18.190	16.980
40.75	19.960	19.180	17.340	18.780	19.270	18.780	17.910
41.00	17.860	18.580	17.810	17.420	17.820	17.430	17.270
41.25	16.450	16.860	17.810	16.670	17.110	15.680	16.480
41.50	16.120	17.950	16.400	16.040	16.400	16.890	16.410
41.75	17.420	17.880	16.400	16.930	17.130	16.280	16.820
42.00	20.220	18.560	18.530	18.700	19.260	17.390	18.100
42.25	17.590	17.830	18.530	17.230	16.280	16.670	16.670
42.50	16.280	17.390	16.600	17.160	16.330	16.450	16.290
42.75	16.390	17.970	16.600	16.060	15.700	15.710	15.790
43.00	16.320	17.210	16.560	15.090	16.010	15.240	15.790
43.25	18.630	18.620	16.560	17.510	18.500	17.930	18.280
43.50	17.550	17.210	17.060	16.960	16.690	16.310	16.280
43.75	15.930	16.060	17.060	16.010	16.770	16.200	15.610
44.00	15.910	15.940	16.220	15.830	15.440	14.740	16.270
44.25	16.810	16.120	16.120	16.430	15.080	15.840	16.550
44.50	15.810	15.970	16.430	15.170	15.730	13.870	15.420
44.75	15.390	16.240	16.430	15.000	15.320	14.290	14.930
45.00	16.100	16.310	15.820	15.240	15.840	15.260	15.070
45.25	17.730	16.310	15.820	15.240	14.840	15.240	15.070
45.50	15.230	16.820	16.430	15.280	15.060	14.770	15.840
45.75	16.130	16.820	16.430	15.280	15.060	14.770	15.840
46.00	16.380	16.770	16.050	14.880	15.760	14.770	15.320
46.25	15.880	15.220	16.430	14.880	15.260	15.570	15.060
46.50	15.700	15.220	15.390	15.300	15.500	15.510	15.060
46.75	16.010	15.670	16.050	14.770	15.500	15.510	14.980
47.00	15.310	15.810	16.430	15.350	15.260	15.330	14.490
47.25	15.810	15.070	16.430	14.870	14.910	14.540	14.490
47.50	15.790	15.070	15.400	14.850	14.910	14.540	14.210
47.75	15.520	15.510	15.400	14.850	15.180	14.880	14.210
48.00	15.930	15.510	15.400	15.250	15.180	14.880	14.650
48.25	15.670	14.860	15.140	15.250	15.180	14.880	14.650
48.50	15.270	14.860	15.140	15.250	15.180	14.880	14.650
49.00	15.690	15.410	15.290	14.820	15.020	14.650	15.190
49.25	16.340	15.410	15.290	14.820	15.020	14.650	15.190
49.50	15.980	15.670	15.590	15.610	15.070	15.280	15.400
49.75	15.590	15.670	15.590	15.610	15.070	15.280	15.400
50.00	15.550	15.370	14.840	13.920	14.510	14.110	14.460
50.25	15.950	15.370	14.840	13.920	14.510	14.110	14.460
50.50	15.670	15.160	15.250	15.390	14.710	14.560	15.030
50.75	16.780	15.160	15.250	15.390	14.710	14.560	15.020

| THETA | ICELL | CELL PLUS SAMPLE INTENSITY | | | | | |
| | | 0.9098 GM/CM³ | | 0.9818 GM/CM³ | | 1.0052 GM/CM³ | |
		A	B	A	B	A	B
51.00	16.340	15.700	15.600	14.560	14.940	14.850	15.020
51.25	17.340	15.700	15.600	14.560	14.940	14.850	15.020
51.50	16.330	15.850	15.630	15.270	15.060	14.570	14.510
51.75	16.370	15.850	15.630	15.270	15.060	14.570	14.510
52.00	17.030	15.900	16.470	15.940	15.150	15.440	15.330
52.25	16.550	15.900	16.470	15.940	15.150	15.440	15.330
52.50	16.460	16.200	15.740	14.870	15.360	14.670	14.860
52.75	16.180	16.200	15.740	14.870	15.360	14.670	14.860
53.00	17.240	15.840	15.740	14.320	14.580	15.490	15.560
53.25	17.350	15.840	15.740	14.320	14.580	15.490	15.560
53.50	16.850	16.160	16.410	15.120	15.340	15.090	15.380
53.75	16.560	16.160	16.410	15.120	15.340	15.090	15.380
54.00	16.850	14.920	16.110	15.270	15.320	14.880	15.140
54.25	16.850	14.920	16.110	15.270	15.320	14.880	15.140
54.50	18.120	16.530	16.560	15.460	15.630	15.610	16.010
54.75	18.120	16.530	16.560	15.460	15.630	15.610	16.010
55.00	17.260	16.330	16.350	15.060	15.630	15.500	14.750
55.25	17.260	16.330	16.350	15.060	15.630	15.500	14.750
55.50	16.600	16.220	16.110	14.280	15.630	15.860	15.350
55.75	16.600	16.220	16.110	14.280	15.630	15.860	15.350
56.00	16.800	16.190	16.500	15.070	15.980	15.470	15.350
56.25	16.800	16.190	16.500	15.070	15.980	15.470	15.350
56.50	17.490	16.520	16.040	15.440	15.850	15.660	15.850
56.75	17.490	16.520	16.040	15.440	15.850	15.660	15.850
57.00	18.760	17.040	17.130	16.230	15.860	15.600	15.620
57.25	18.760	17.040	17.130	16.230	15.860	15.600	15.620
57.50	18.200	17.590	17.590	15.250	16.160	16.910	15.720
57.75	18.200	16.330	17.590	15.250	16.160	16.910	15.720
58.00	18.160	17.250	17.140	15.910	16.530	15.770	16.220
58.25	18.160	17.250	17.140	15.910	16.530	15.770	16.220
58.50	18.360	16.690	16.810	16.380	15.820	15.650	16.480
58.75	18.360	16.690	16.810	16.380	15.820	15.650	16.480
59.00	18.330	16.860	17.590	16.250	16.250	15.990	15.990
59.25	18.330	16.860	17.590	16.940	16.250	16.380	15.990
59.50	18.280	16.240	17.600	16.630	16.370	16.770	16.210
59.75	18.280	16.240	17.600	16.630	16.370	16.770	16.210
60.00	18.990	16.860	17.510	16.700	16.780	16.320	17.680
60.25	18.990	16.970	17.510	16.700	16.780	16.320	17.680
60.50	19.010	17.060	17.380	17.370	16.780	16.640	17.130
60.75	19.010	17.060	17.380	17.370	16.780	16.640	17.130
61.00	18.620	18.030	17.140	17.800	16.910	16.860	17.880
61.25	18.620	18.030	17.140	17.800	16.910	16.860	17.880
61.50	19.900	18.420	18.270	17.800	18.270	16.810	17.400
61.75	19.900	18.420	18.270	17.800	18.270	16.810	17.400
62.00	19.650	18.300	18.440	17.590	17.440	16.750	17.590
62.25	19.650	18.390	18.500	18.290	18.190	17.000	17.610
62.50	19.910	18.390	18.820	18.290	18.190	17.000	17.610
62.75	19.910	19.130	18.820	18.420	18.640	17.970	18.160
63.00	19.980	19.130	18.820	18.420	18.640	17.970	18.160
63.25	19.980	19.110	18.820	18.420	18.640	17.970	18.160

| THETA | ICELL | CELL PLUS SAMPLE INTENSITY | | | | | |
| | | 0.9098 GM/CM³ | | 0.9818 GM/CM³ | | 1.0052 GM/CM³ | |
		A	B	A	B	A	B
63.50	19.710	17.880	19.390	18.200	19.050	16.860	17.390
63.75	19.110	17.880	19.390	18.200	19.050	16.860	17.390
64.00	20.470	18.660	18.930	18.700	17.180	17.790	17.710
64.25	20.470	18.660	18.930	18.700	17.180	17.790	17.710
64.50	21.220	18.910	19.690	18.260	18.510	17.320	13.950
64.75	21.220	18.910	19.690	18.260	18.510	17.320	13.950
65.00	21.620	18.770	19.350	19.420	18.570	18.560	18.360
65.25	21.620	18.770	19.350	19.420	18.570	18.560	18.360
65.50	21.920	20.000	19.450	18.880	18.710	18.040	13.920
65.75	21.920	20.000	19.450	18.880	18.710	18.040	13.920
66.00	21.210	19.690	19.290	19.050	18.850	19.540	19.250
66.25	21.210	19.690	19.290	19.050	18.850	19.540	13.230
66.50	21.960	19.810	21.010	19.620	20.330	19.280	13.230
66.75	21.960	19.810	21.010	19.620	20.330	19.280	13.470
67.00	21.740	20.700	19.880	19.730	19.470	19.310	13.470
67.25	21.740	20.700	19.880	19.730	19.470	19.310	13.470
67.50	22.140	20.760	19.770	19.500	19.280	17.870	20.290
67.75	22.140	20.760	19.770	19.500	19.280	17.870	20.290
68.00	23.010	20.120	19.970	19.500	20.160	19.250	19.680
68.25	23.010	20.120	19.970	19.890	20.160	19.250	19.840
68.50	23.690	20.060	20.700	20.060	19.470	19.350	19.440
68.75	23.690	20.060	20.700	20.180	19.470	19.350	19.440
69.00	23.500	21.070	21.410	20.760	20.120	19.120	20.240
69.25	23.500	21.070	21.410	20.760	20.120	19.120	20.240
69.50	22.460	21.060	20.450	20.250	20.480	19.210	20.240
69.75	22.460	21.060	20.450	20.110	20.480	19.210	20.240
70.00	23.820	21.190	20.990	20.820	19.860	20.400	20.770
70.25	23.820	21.190	20.990	20.820	19.860	20.400	20.770
70.50	23.870	21.060	21.660	21.010	20.160	19.680	20.860
70.75	23.870	21.060	21.660	21.010	20.160	19.680	20.860
71.00	24.440	22.130	22.010	20.820	21.650	20.350	20.980
71.25	24.440	22.130	22.010	20.820	21.650	20.350	21.160
71.50	24.320	22.010	22.200	22.300	20.330	21.330	21.160
71.75	24.320	22.010	22.200	22.300	20.330	21.330	21.160
72.00	24.550	22.350	21.630	21.890	21.030	20.230	20.750
72.25	24.550	22.350	21.630	21.890	21.030	20.230	20.750
72.50	25.190	22.730	22.530	21.320	21.610	21.410	20.100
72.75	25.190	22.730	22.530	21.320	21.610	21.410	21.270
73.00	25.620	21.930	21.740	21.940	21.730	20.840	21.270
73.25	25.620	21.930	21.740	21.940	21.730	20.840	21.940
73.50	25.190	22.290	22.690	21.740	20.130	21.380	21.940
73.75	25.190	22.290	22.690	21.740	20.130	21.380	21.970
74.00	25.290	22.880	23.010	22.450	20.800	20.980	21.970
74.25	25.290	22.880	23.010	22.450	20.800	20.980	21.970
74.50	25.240	22.670	22.520	21.220	21.550	21.750	21.930
74.75	25.240	22.670	22.520	21.220	21.550	21.750	21.930
75.00	25.310	23.090	23.490	22.720	21.240	21.730	22.100

TABLE 6

INTENSITIES (counts/second) FOR EVACUATED BERYLLIUM CELL

AND BERYLLIUM CELL CONTAINING LIQUID ARGON

DATA NEAR SELECTED BERYLLIUM PEAKS

THETA	ICELL	AVG. CELL PLUS SAMPLE INTENSITY		
		0.9098 (GM/CM3)	0.9818 (GM/CM3)	1.0052 (GM/CM3)
9.0625	22.19	46.43	45.03	44.15
9.1250	23.30	46.85	45.84	43.61
9.1875	25.35	48.50	47.35	44.45
9.3125	27.36	49.02	47.22	45.68
9.3750	26.68	48.55	47.76	45.93
9.4375	27.22	51.16	47.99	45.63
9.5625	23.92	46.28	44.85	44.36
9.6250	22.94	47.36	45.29	43.26
9.6875	24.92	47.16	46.59	44.27
9.8125	32.52	52.93	49.43	48.50
9.8750	32.15	51.75	49.97	49.93
9.9375	29.04	50.58	47.68	47.31
10.5625	27.00	49.86	48.26	48.38
10.6250	26.08	49.92	50.22	48.24
10.6875	26.12	51.81	49.53	47.31
10.8125	26.68	49.96	49.20	48.36
10.8750	27.05	50.52	49.72	49.51
10.9375	29.55	52.72	51.41	50.10
11.0625	39.10	57.70	54.94	53.77
11.1250	43.40	60.85	58.24	56.06
11.1875	59.66	66.79	67.88	61.58
12.0625	41.15	57.02	57.20	56.68
12.1250	40.75	56.26	55.48	54.28
12.1875	41.08	56.06	57.63	52.89
12.3125	39.72	56.14	54.40	53.11
12.3750	40.42	55.71	54.55	52.05
12.4375	39.92	53.58	54.06	53.54

TABLE 7

CHARACTERISTICS OF INTENSITY CURVES FOR ARGON

Temp. (°C)	Density (gm/cm³)	Positions of Peaks ($\mathring{A}^{-1}$)					Ratio of Main Peak Intensity to Intensity at S = 8.8 $\mathring{A}^{-1}$
		First	Second	Third	Fourth	Fifth	
-130	0.9098	1.85	3.61	5.4	8.0	9.2	6.97
	0.9818	1.85	3.63	5.5	7.3	8.6	7.55
	1.0052	1.85	3.63	5.5	7.5	9.4	7.93
-129[*]	0.87	1.87	3.5	5.0	...	...	7.7

[*]Eisenstein and Gingrich [56]

TABLE 8

FEATURES OF RADIAL DISTRIBUTION FUNCTIONS OF LIQUID ARGON

Density (gm/cm³)	First Coordination Number		Shell Positions (Å)				r_2/r_1
	$r\rho(r)$Method	$r^2\rho(r)$Method	1	2	3	4	
T = -130°C							
0.9098	5.1 ± .1	6.0 ± .1	4.02+.05	7.5+.1	11.0+.3	....	1.86
0.9198	4.6 ± .1	4.9 ± .1	3.88+.04	7.42+.08	10.9+.3	14.2+.3	1.91
1.0052	3.8 ± .1	4.2 ± .1	3.83+.04	7.35+.06	10.8+.3	14.3+.5	1.92
T = -129°C							
0.87[a]	3.9 - 4.6		3.8	5.4	7.2	....	1.4
0.87[b]			3.90	7.2	10.3	....	1.85
T = 84°K (-189°C)							
1.40							1.4[a] 1.98[b] 1.9[c]

[a] Eisenstein and Gingrich 56
[b] Finbak 8
[c] Henshaw 65
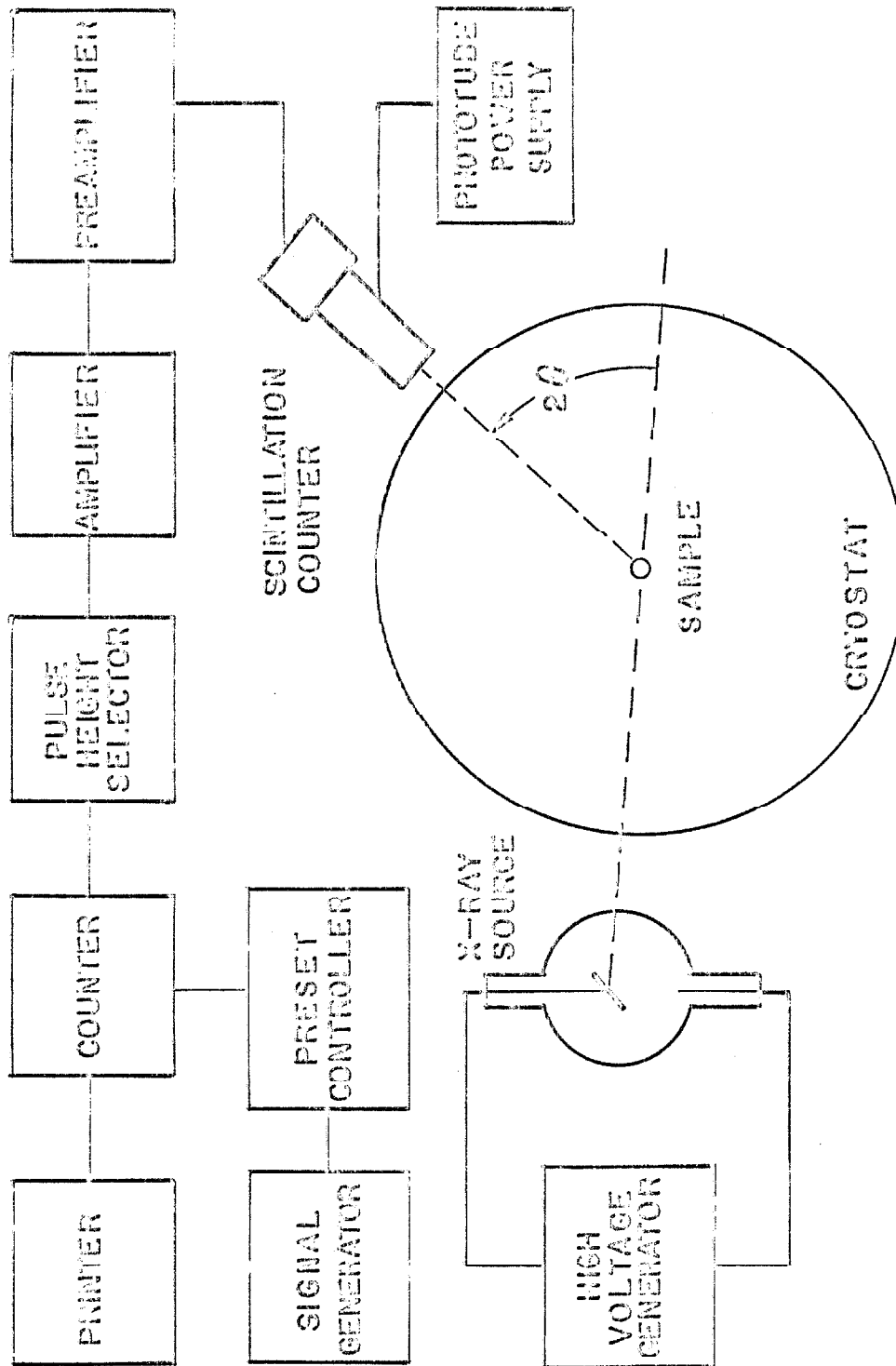
Figure 1. Block Diagram of X-Ray Detection System
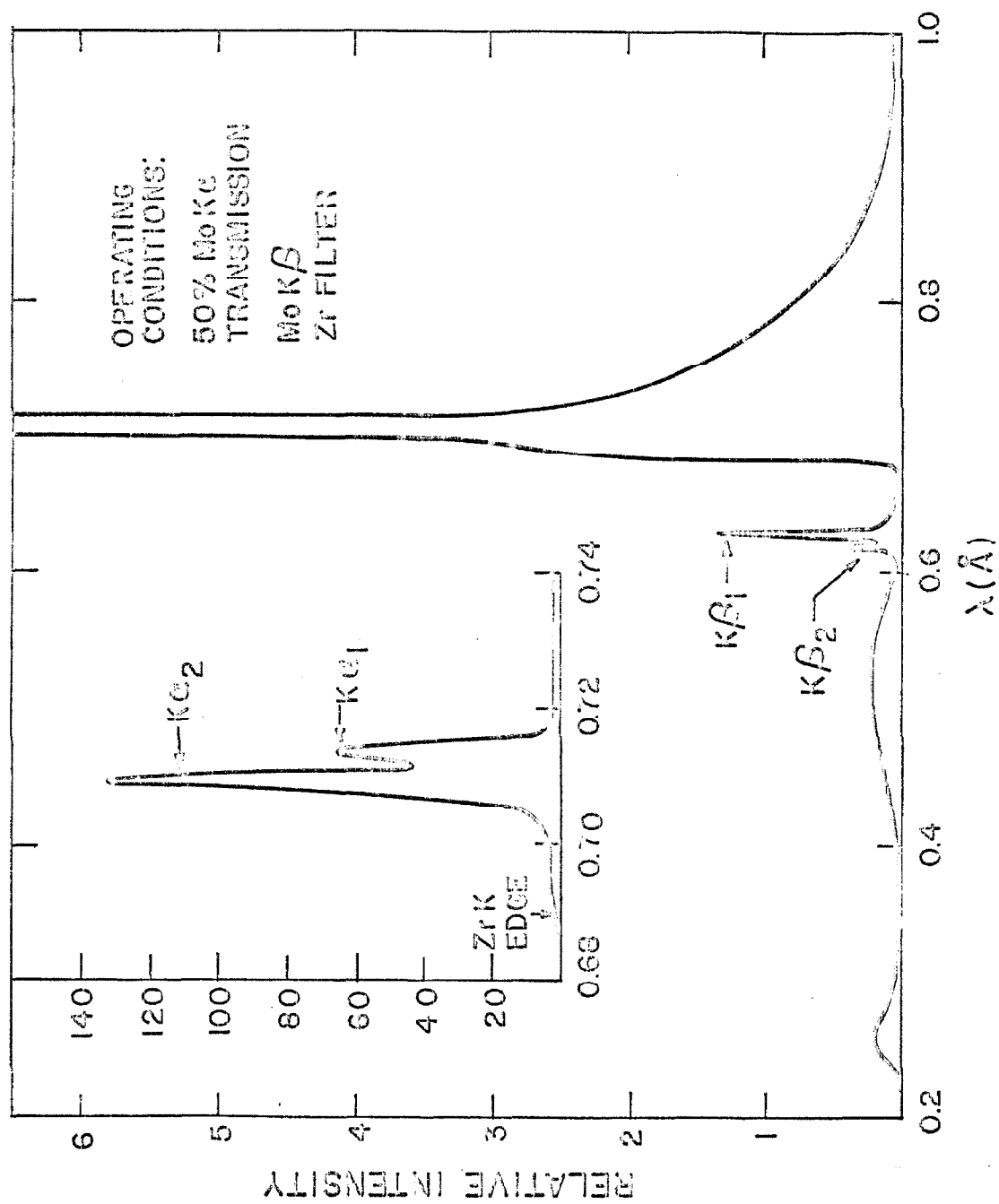
Figure 2. Molybdenum X-Ray Spectrum after Monochromatization
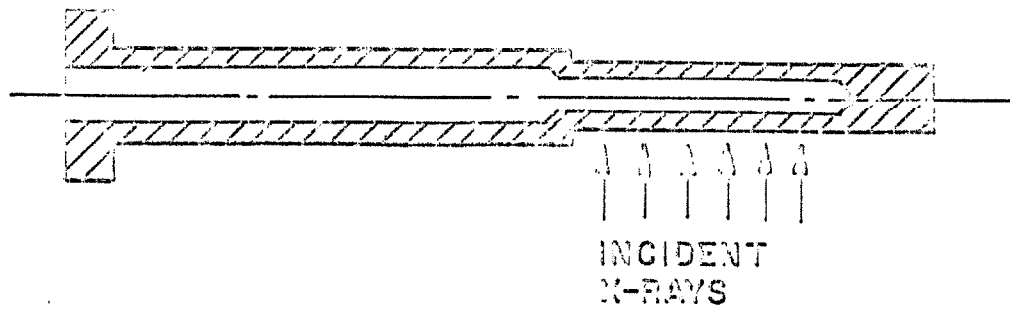
DIMENSIONS OF IRRADIATED
CELL VOLUME

LENGTH: 0.375 IN.
INSIDE DIA.: 0.056 IN.
OUTSIDE DIA.: 0.100 IN.

Figure 3. Cross Section of Beryllium Sample Cell
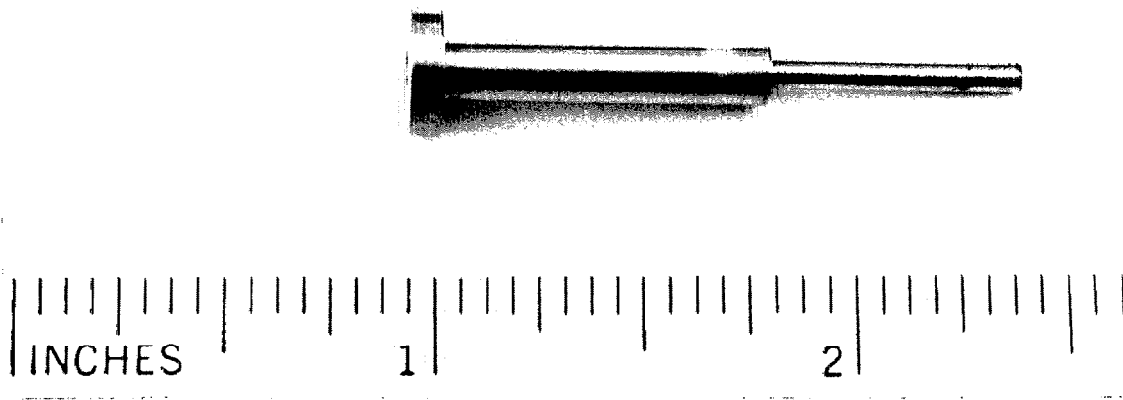
Figure 4. Illustration of Beryllium Sample Cell
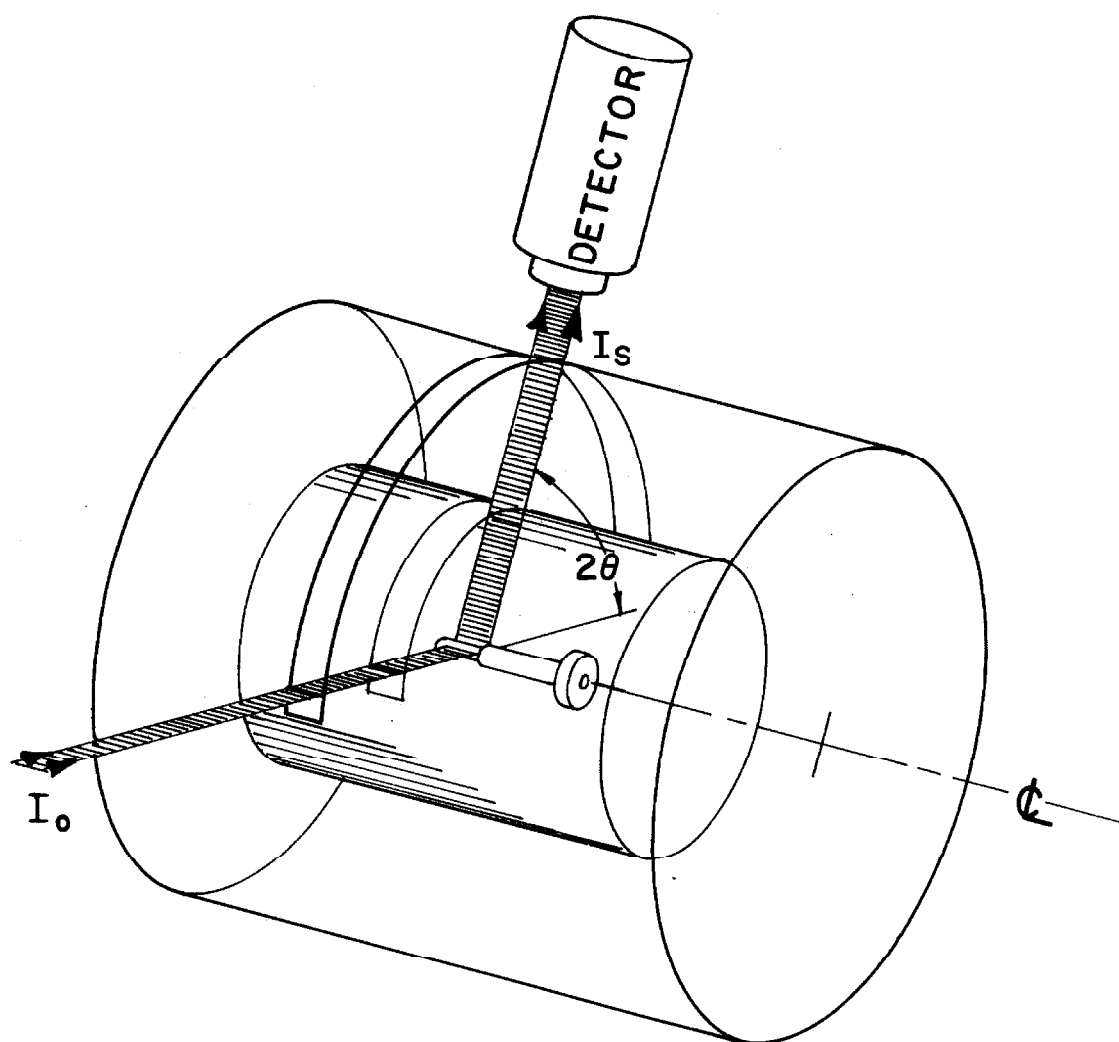
Figure 5. Pictorial Illustration of Cyrostat Geometry
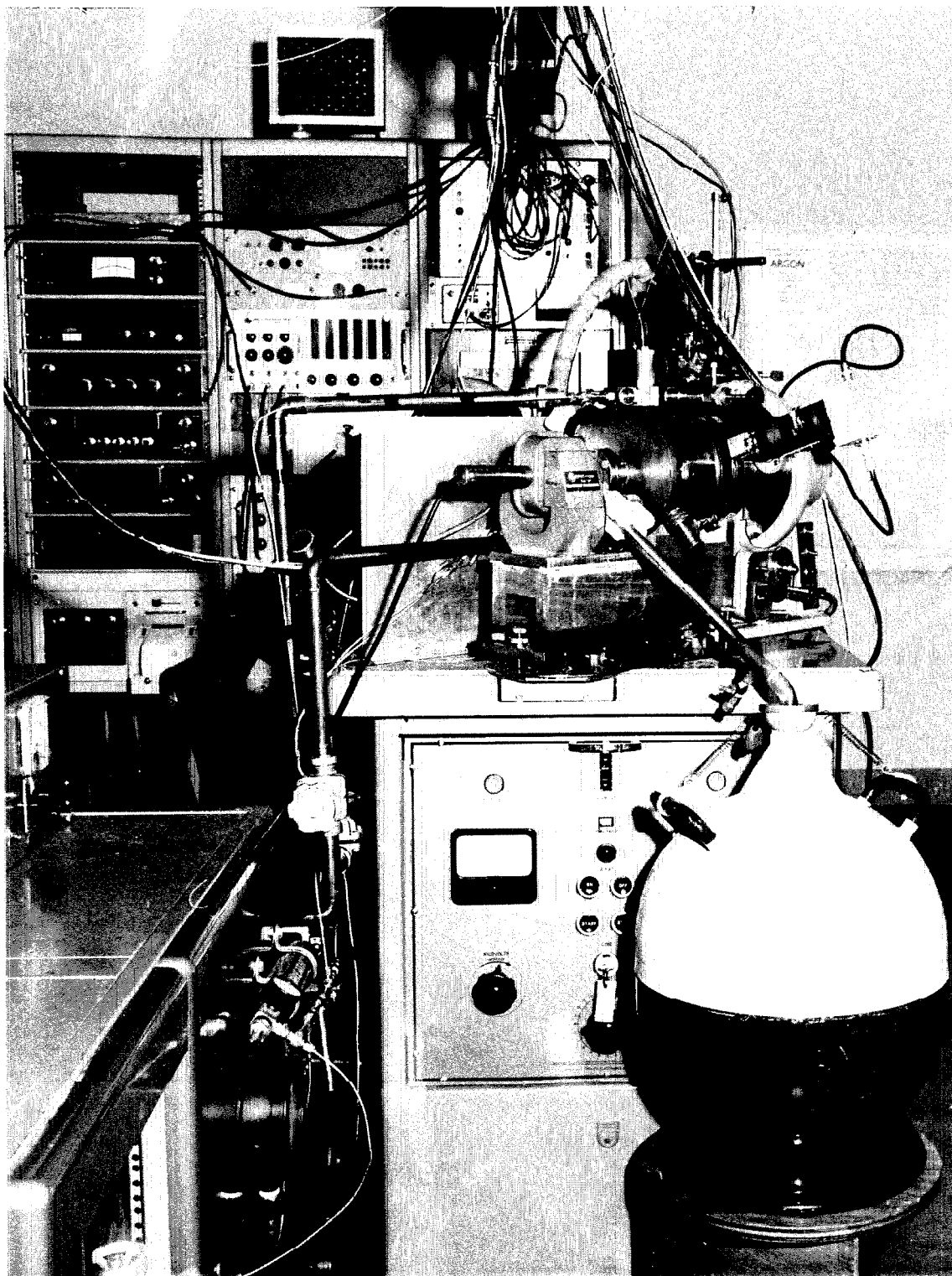
Figure 6. Illustration of Experimental Area and Cryostat
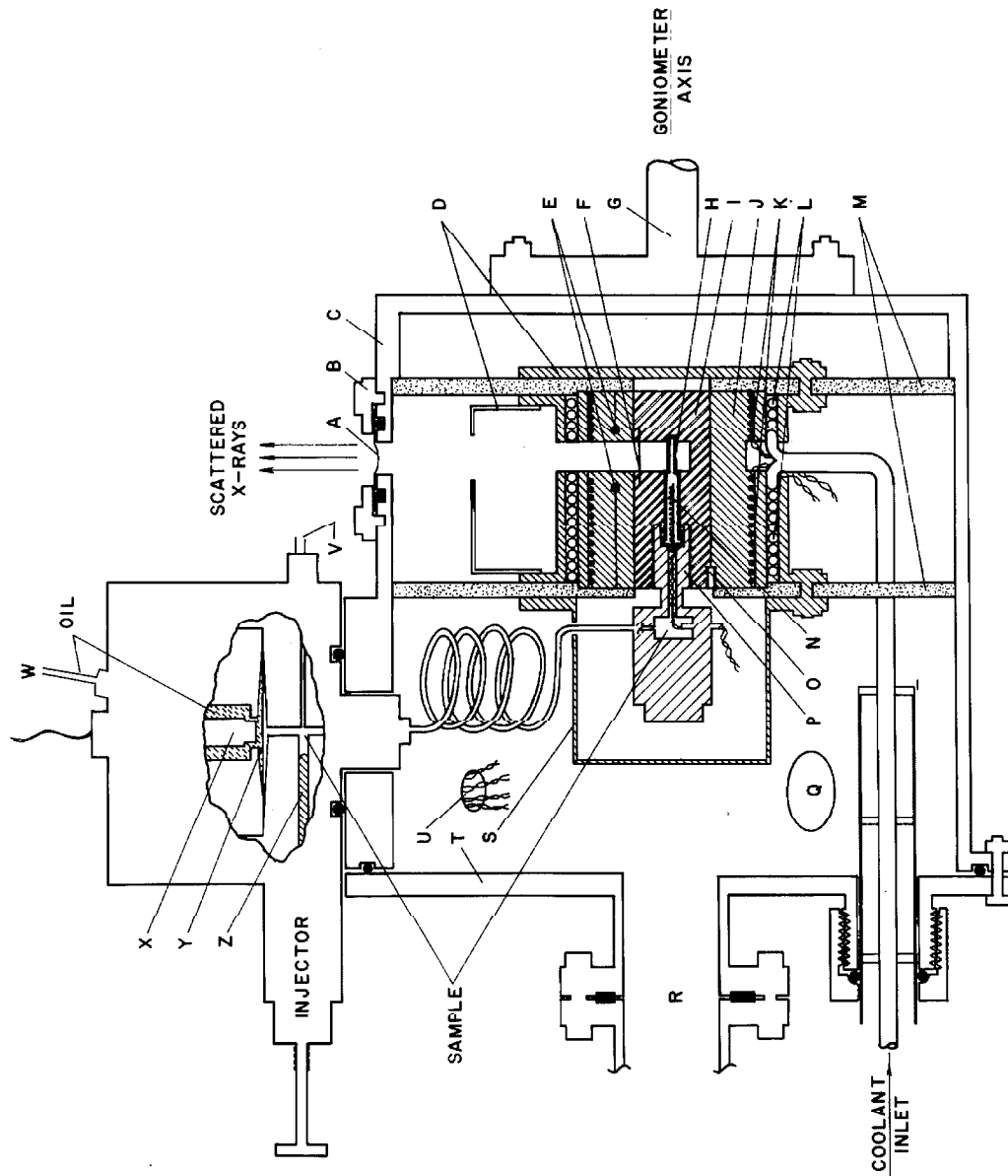
Figure 7. Cross Section of Cryostat
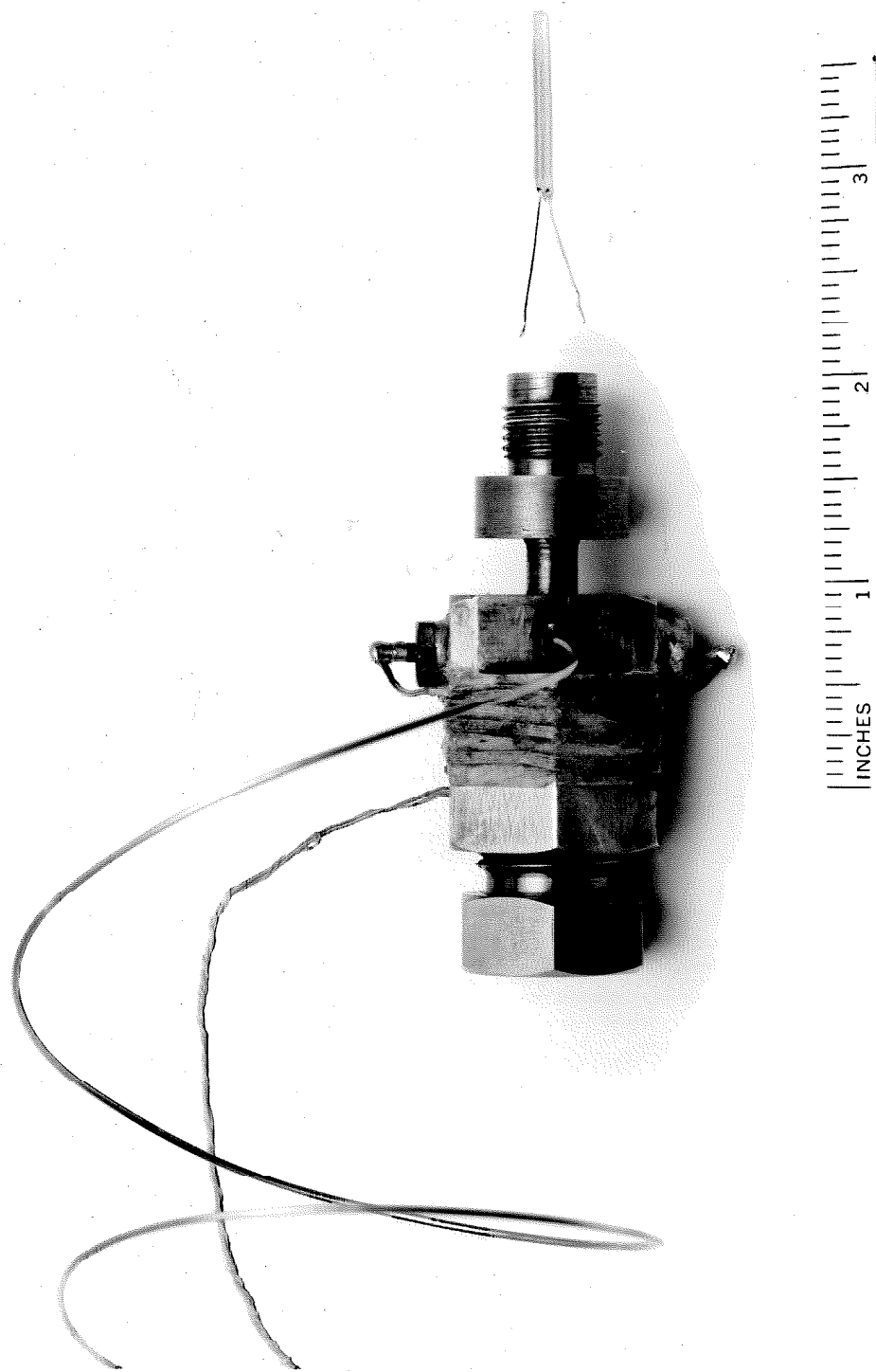
Figure 8.   Illustration of Thermometer and Cell Closure Nut
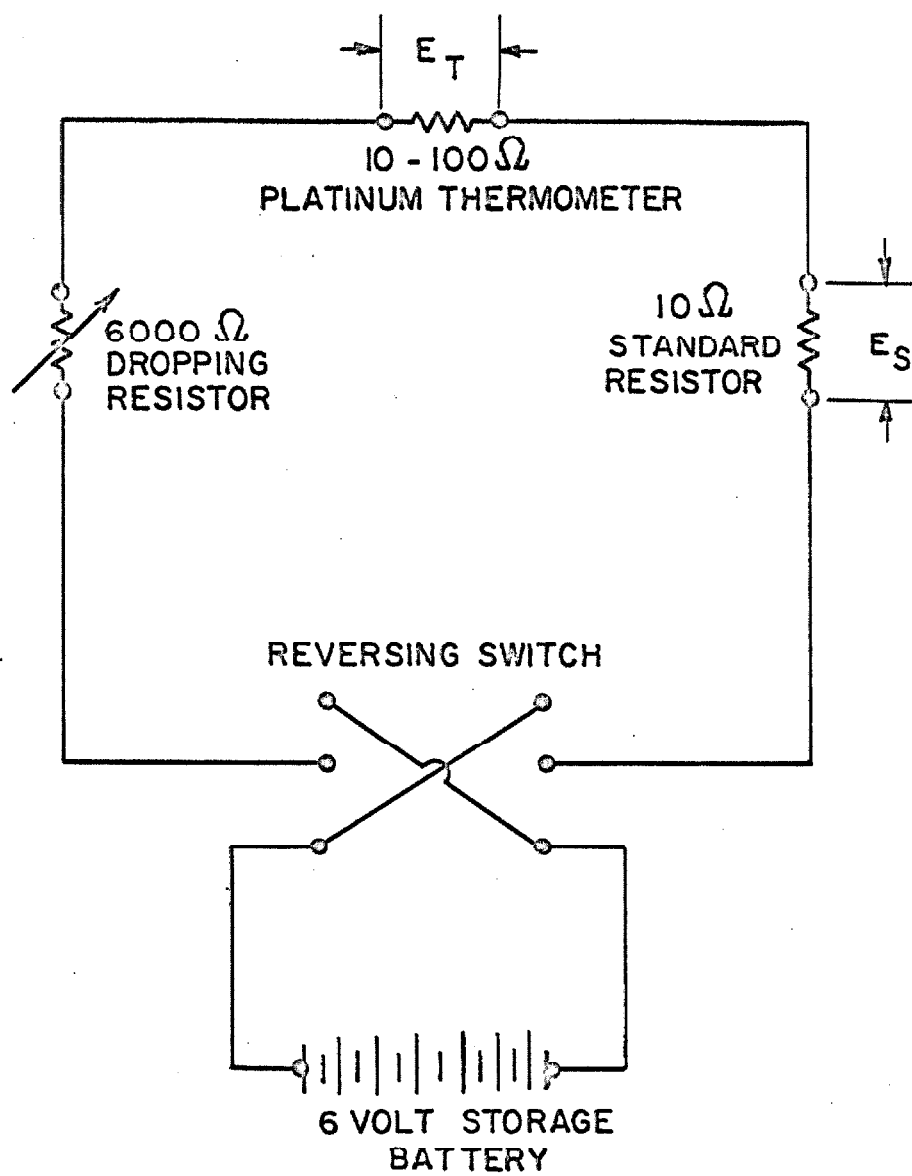
Figure 9. Schematic Wiring Diagram for Platinum Resistance
    Thermometer
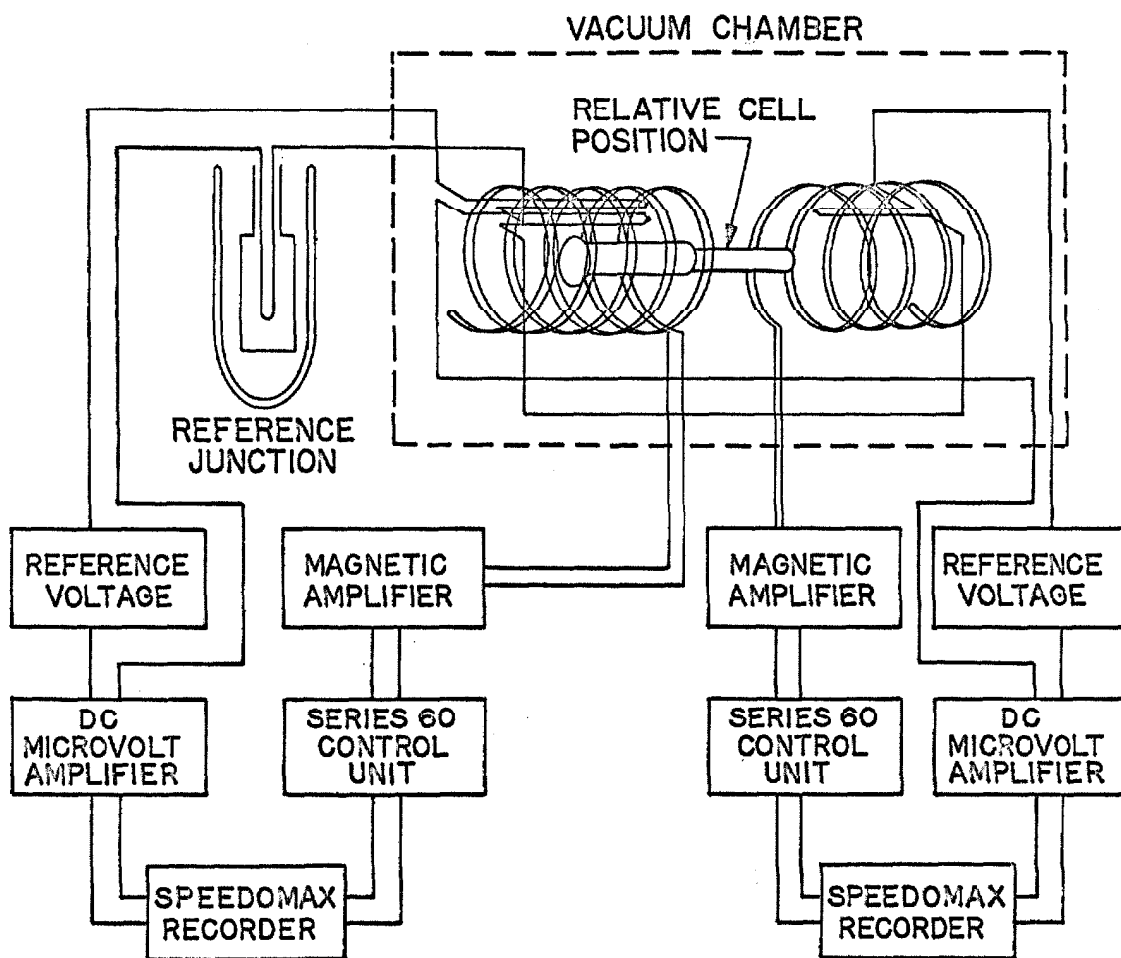
Figure 10. Pictorial Illustration of Temperature Control System
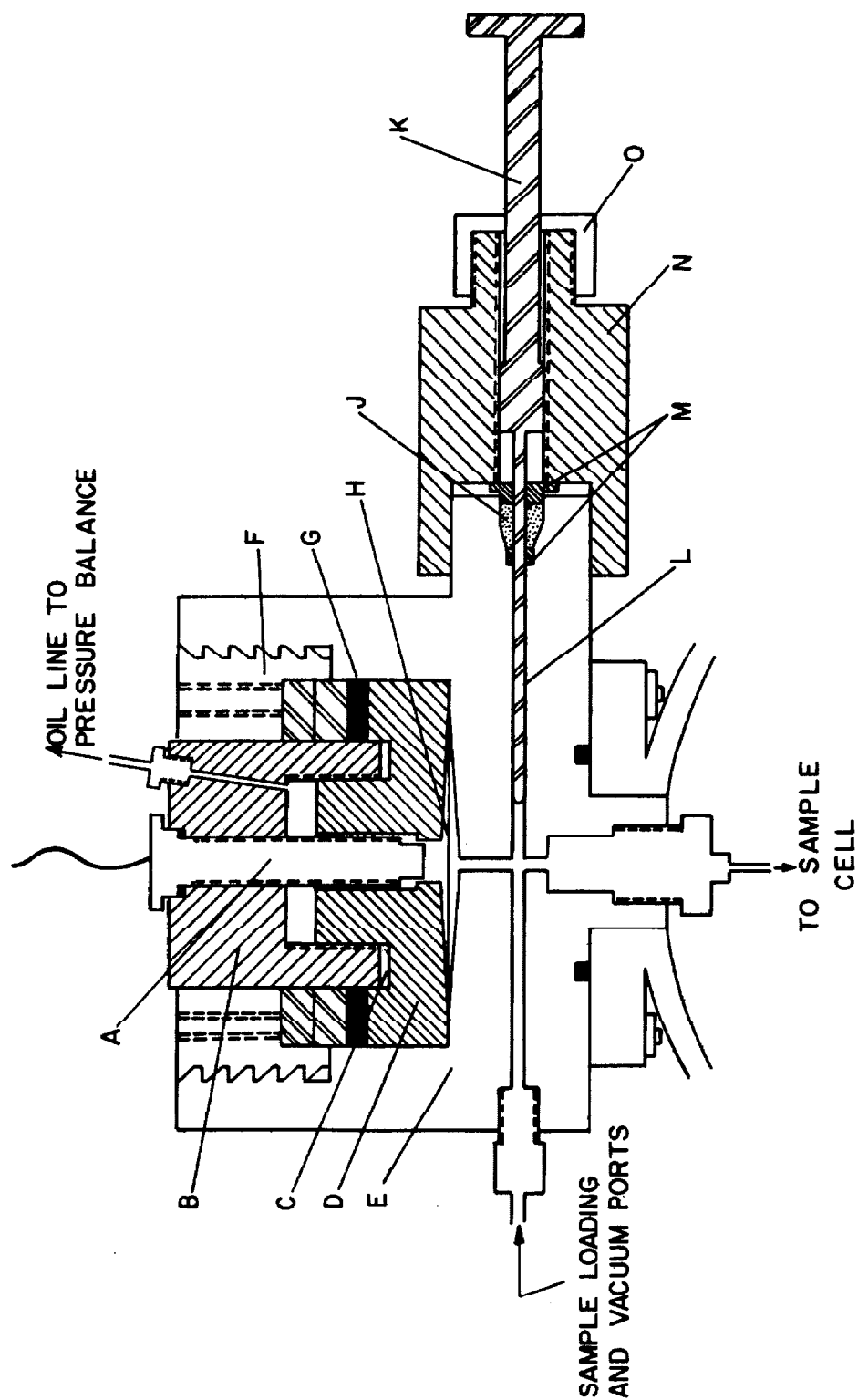
Figure 11. Cross Section of Diaphragm Transducer and Pressure Manifold
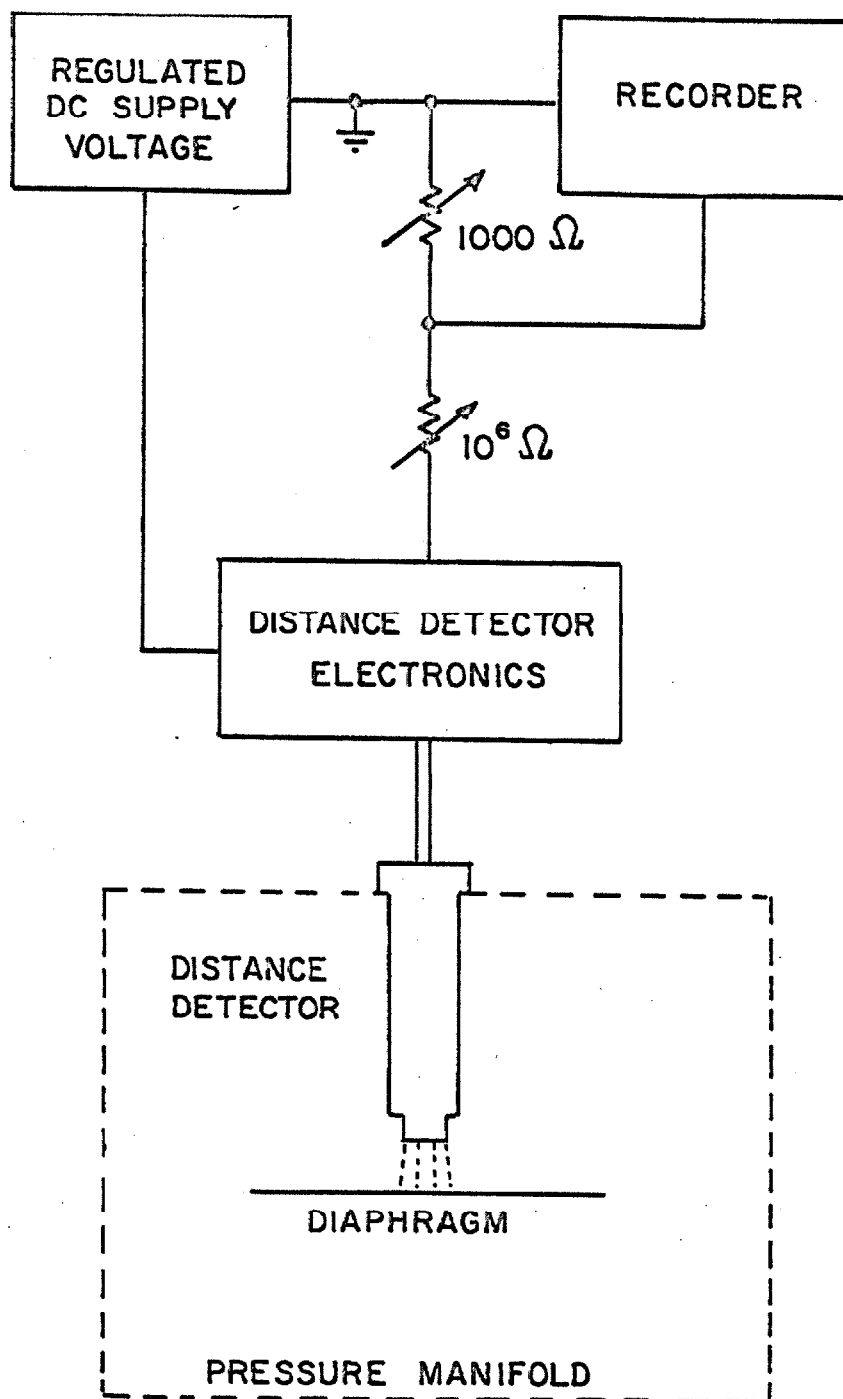
Figure 12. Block Diagram of Pressure Transducer

HEISE GAUGES
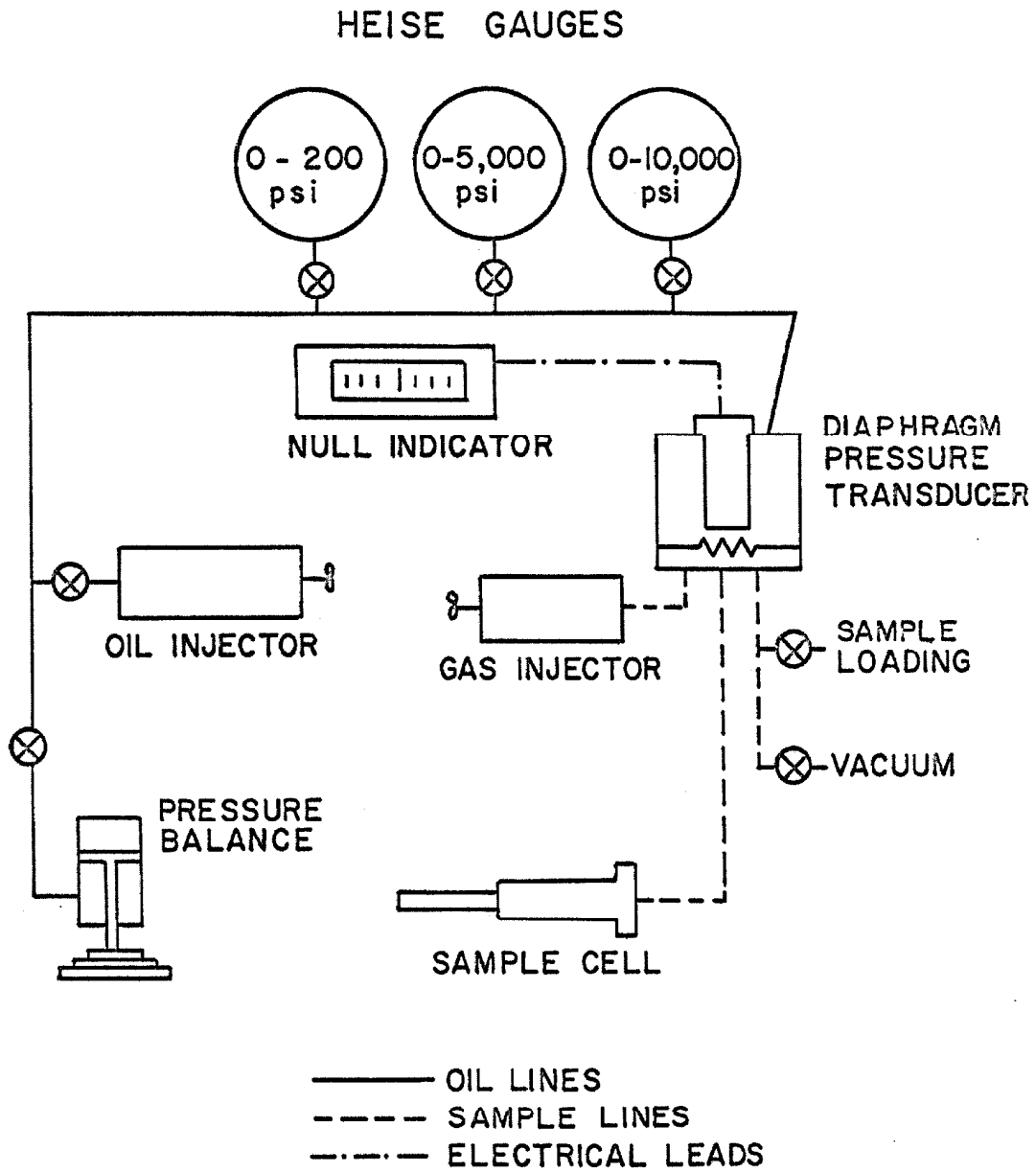
Figure 13. Block Diagram of Pressure Control System
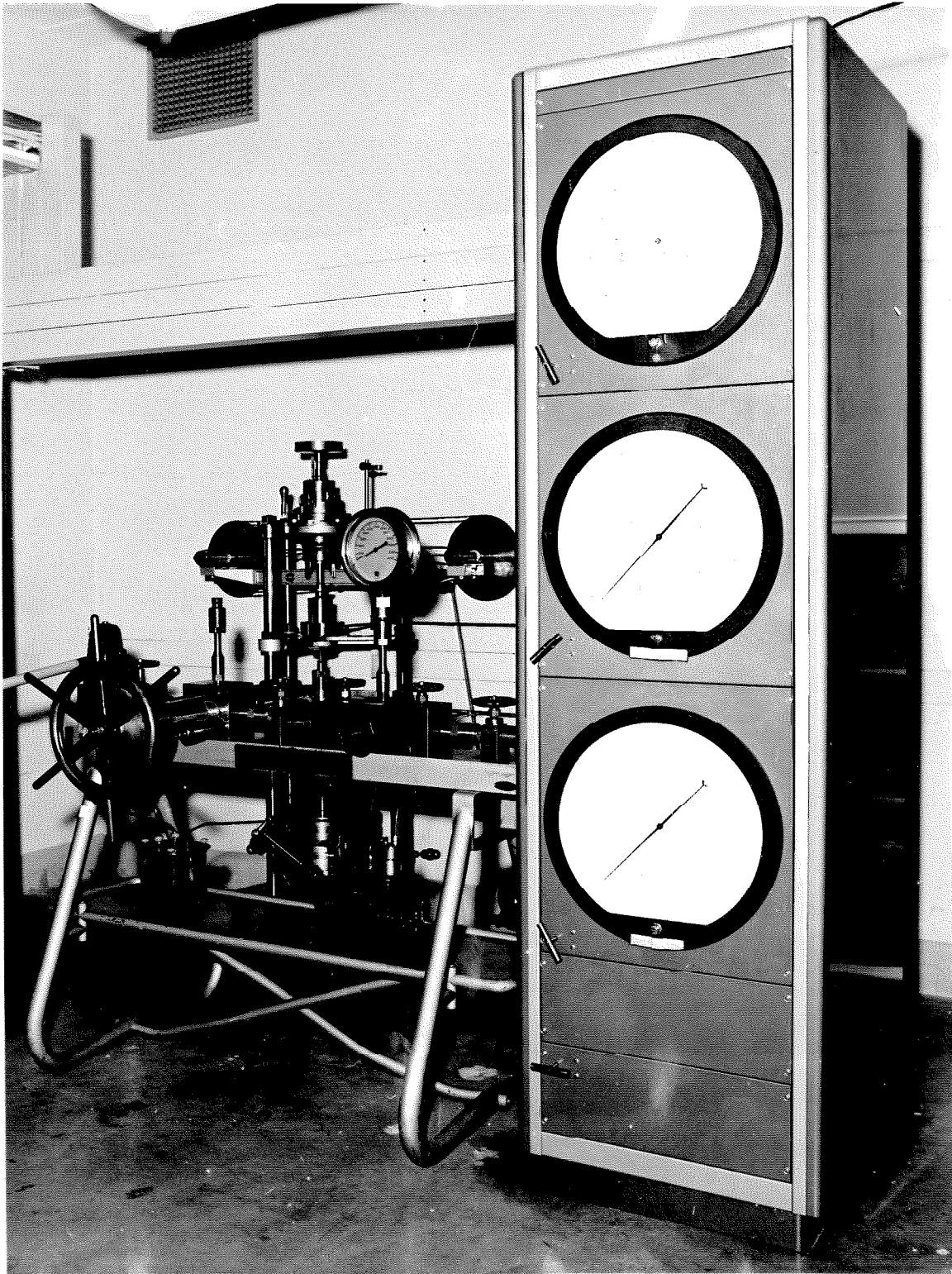
Figure 14. Illustration of Pressure Control System
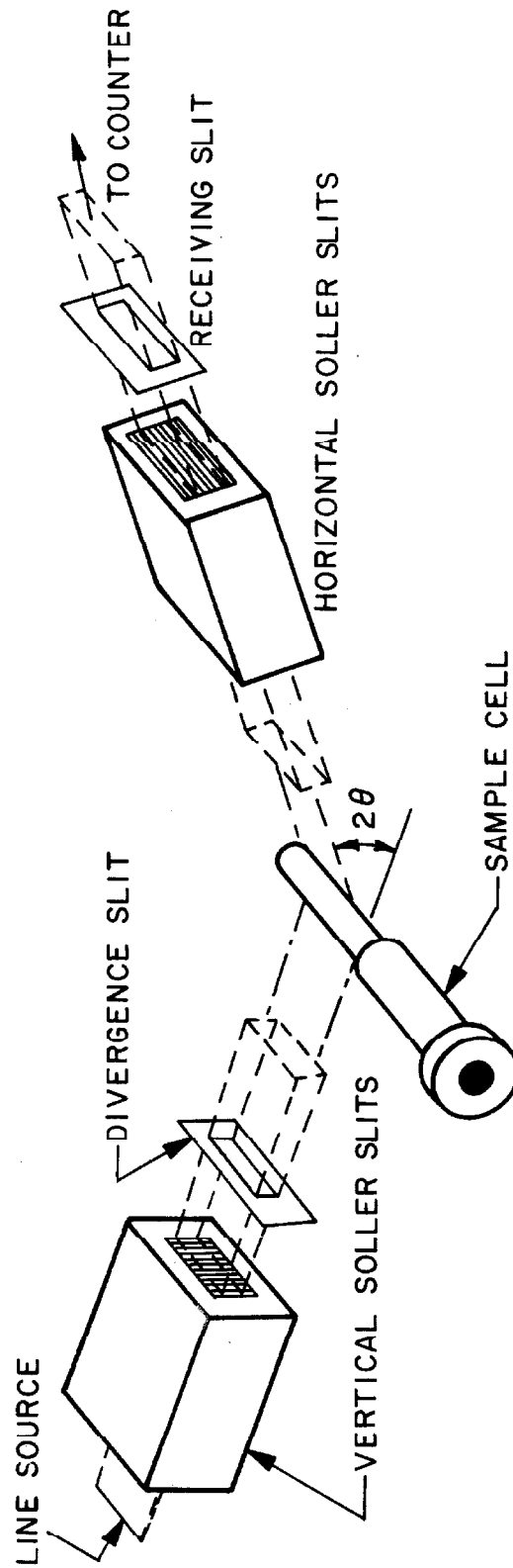
Figure 15. Pictorial Illustration of Collimation System

Figure 17. Horizontal Cell Alignment Data

Figure 16. Vertical Cell Alignment Data
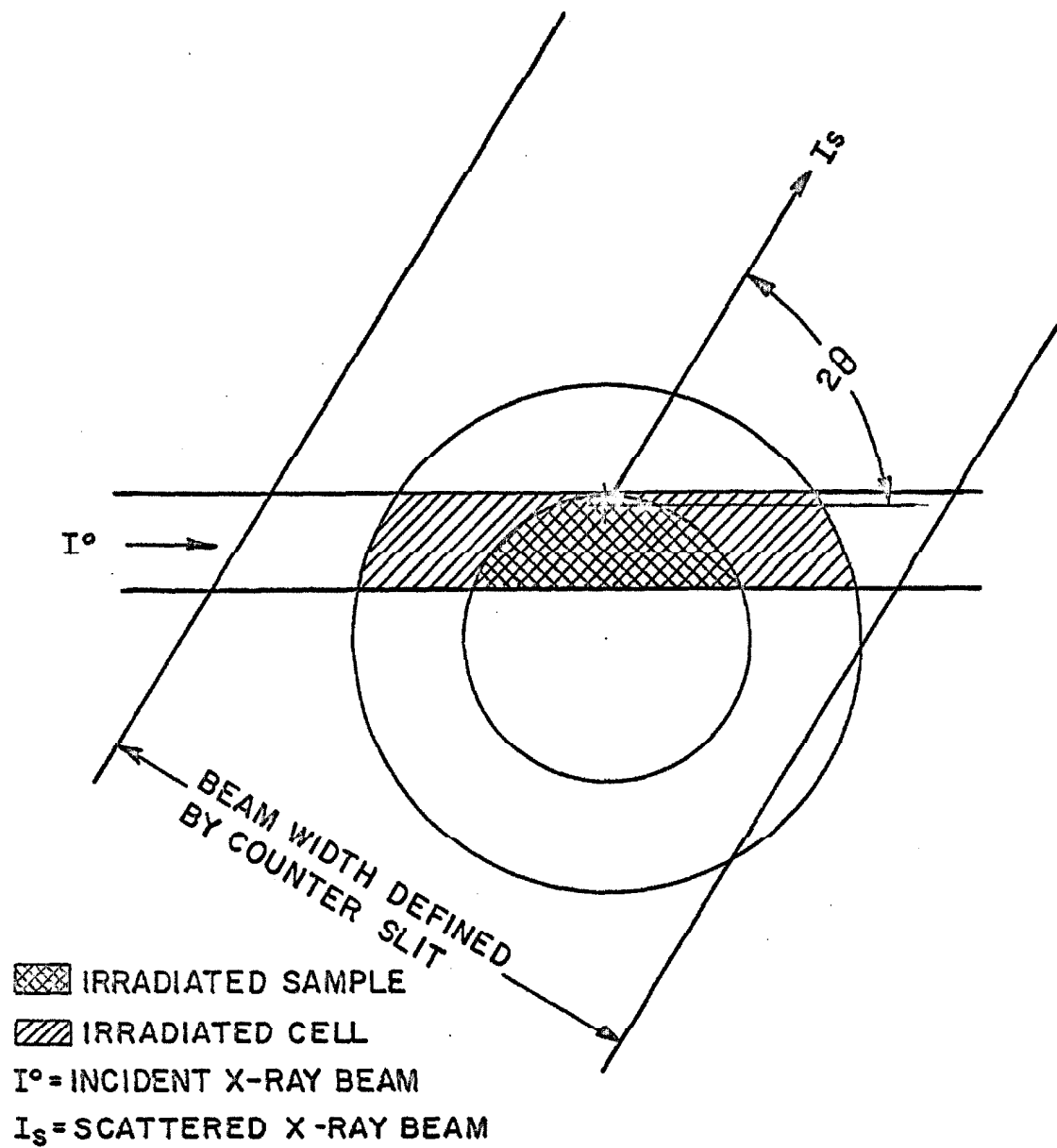
Figure 18. Scattering Geometry of Partially Exposed Cell

K

L

A

F

B

G

C

H

D

J

E

⊢1INCH⊣
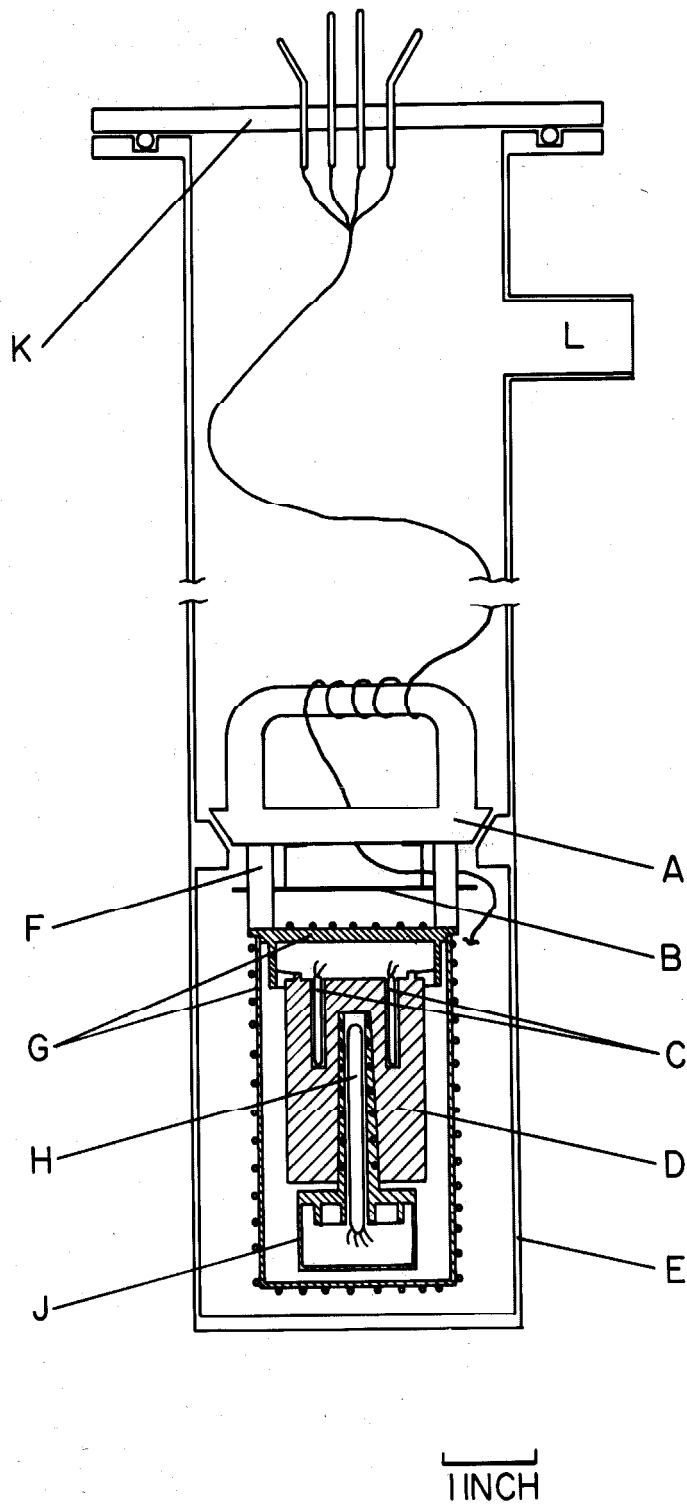
Figure 19. Cross Section of Thermometer Calibration Apparatus
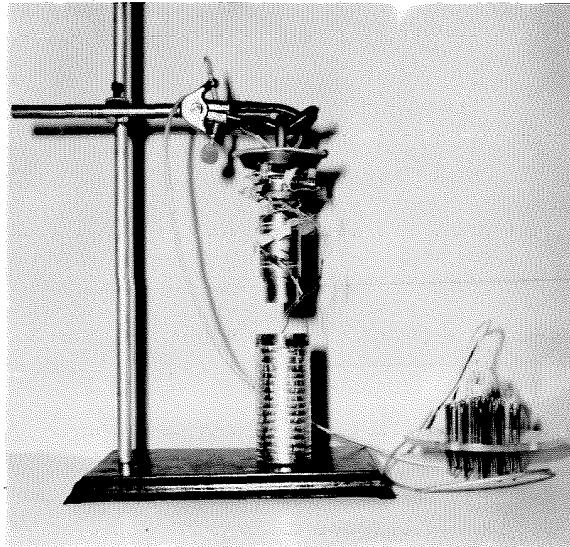
Figure 20. Illustration of Thermometer Calibration Apparatus
During Assembly
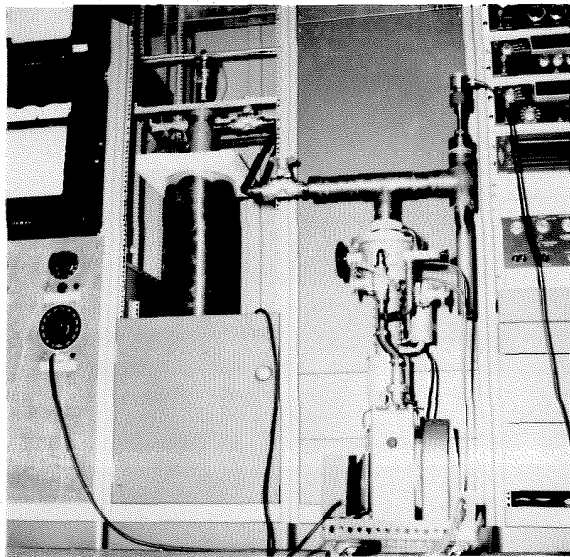
Figure 21. Illustration of Thermometer Calibration Apparatus
In Position
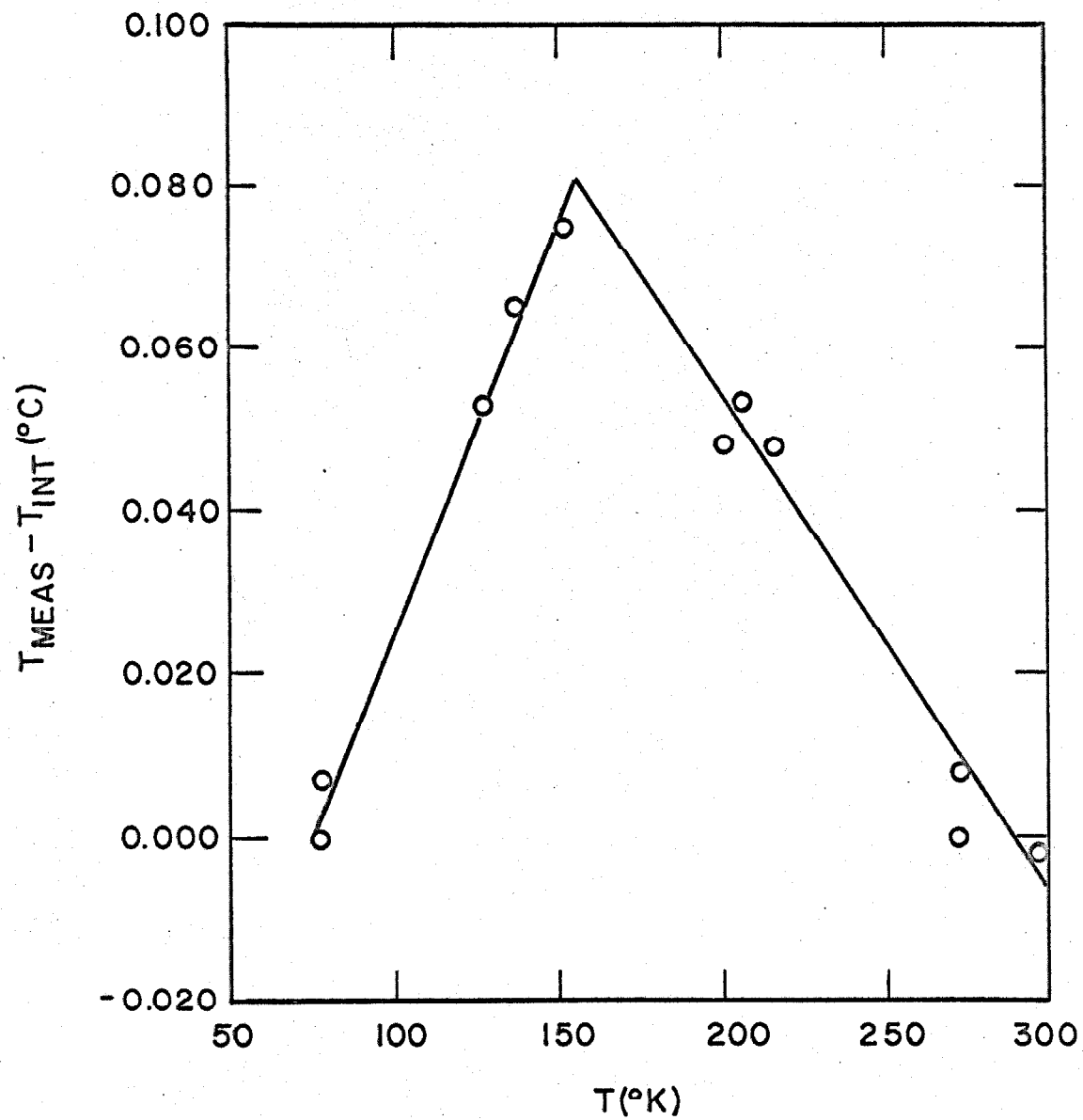
Figure 22. Deviation Plot for Thermometer No. 2
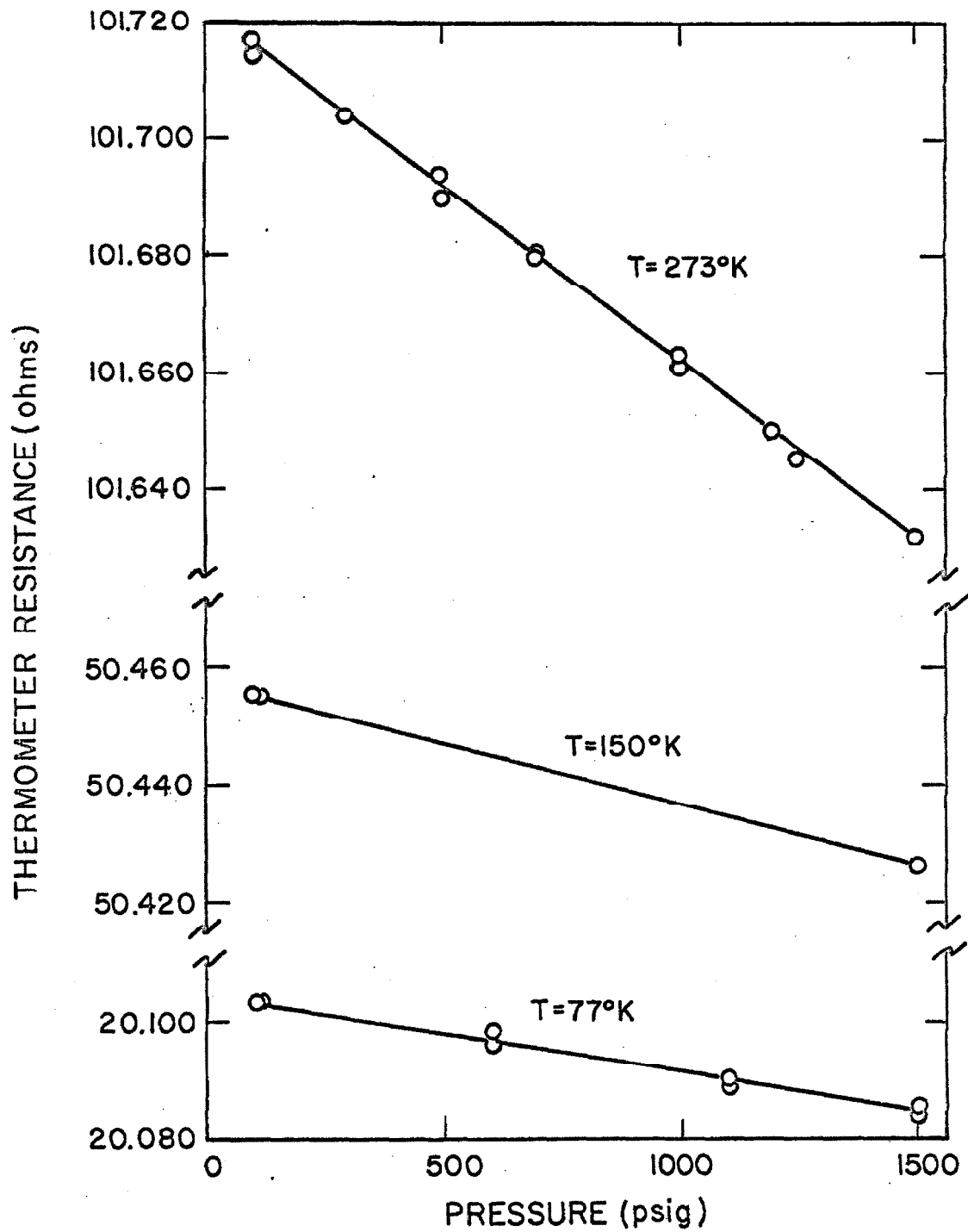
Figure 23. Thermometer Pressure Calibration at 77°, 150° and 273° K
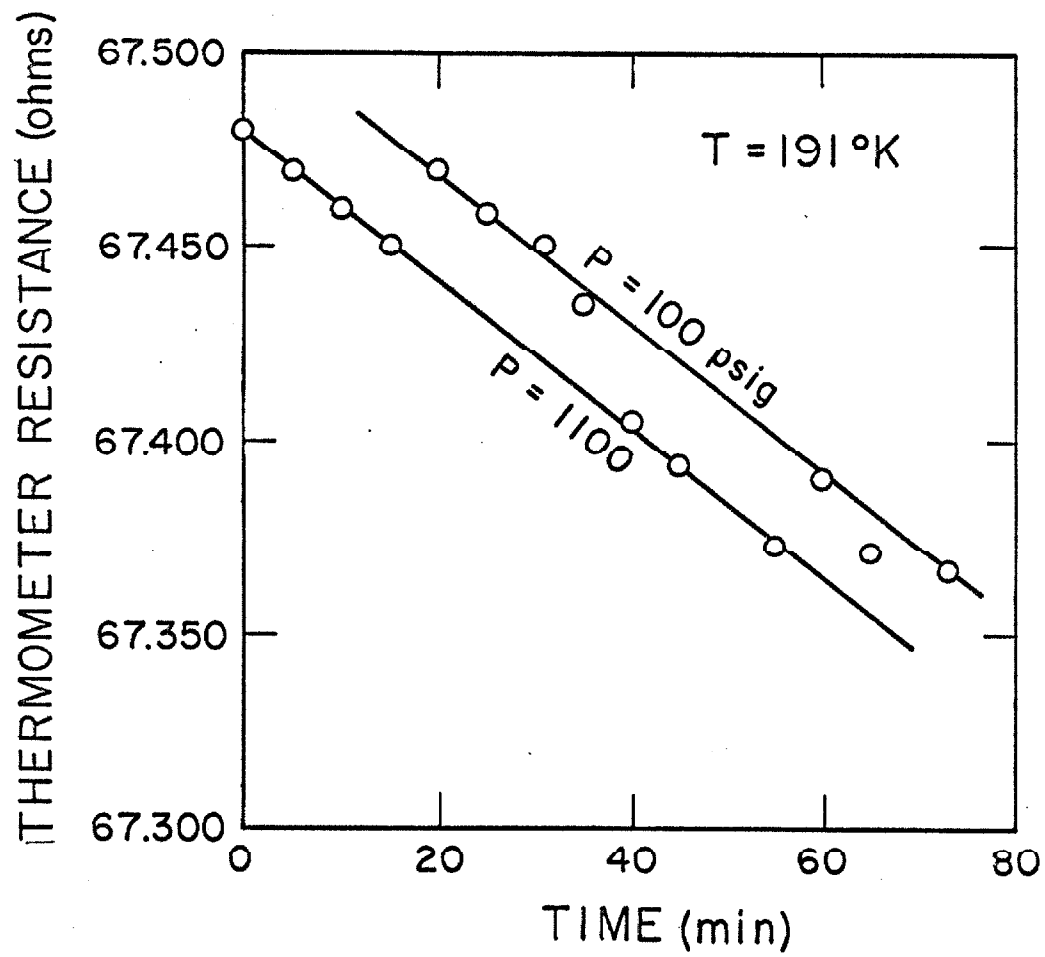
Figure 24. Thermometer Pressure Calibration at 191° K
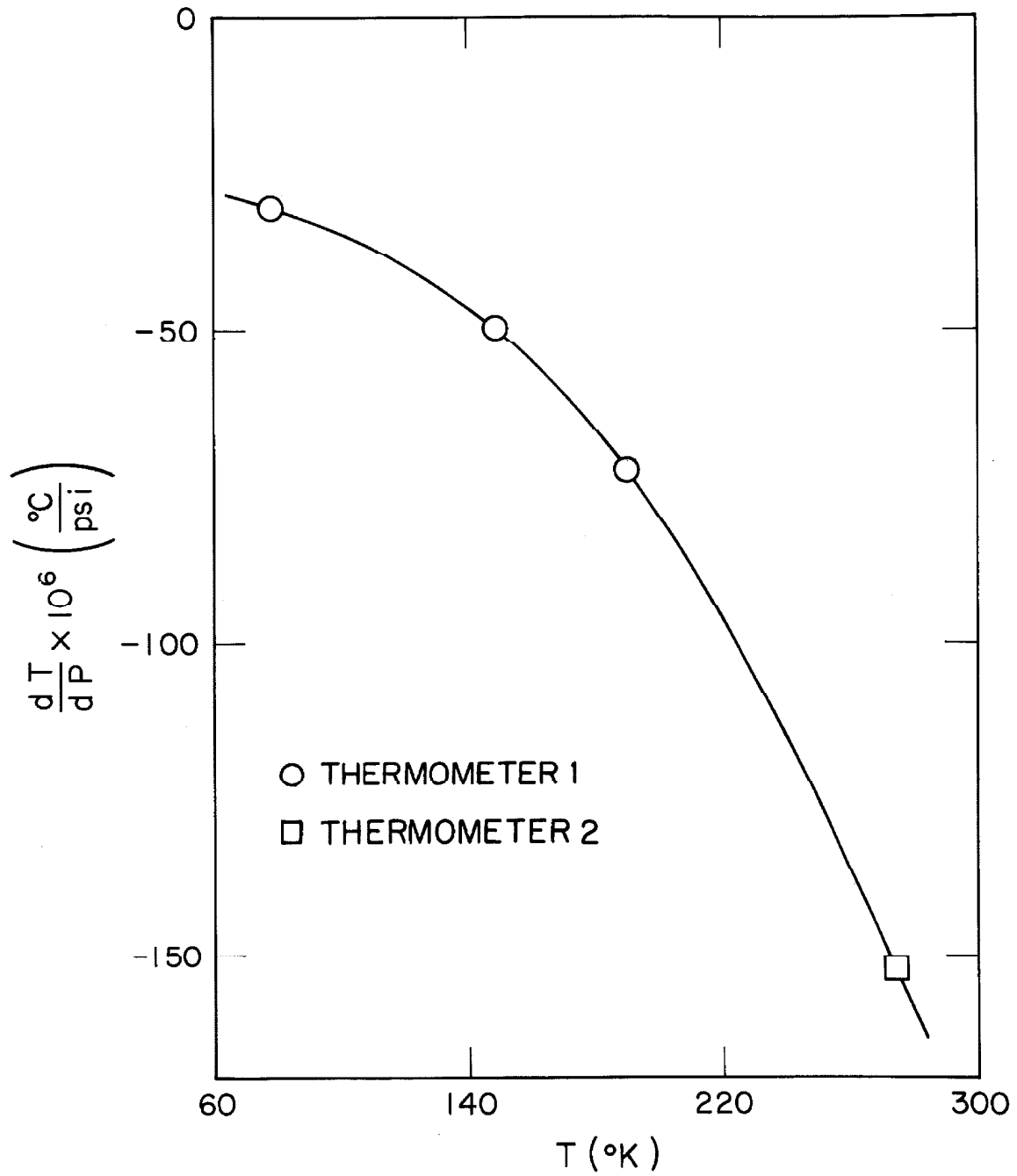
Figure 25. Thermometer Pressure Coefficient vs. Temperature
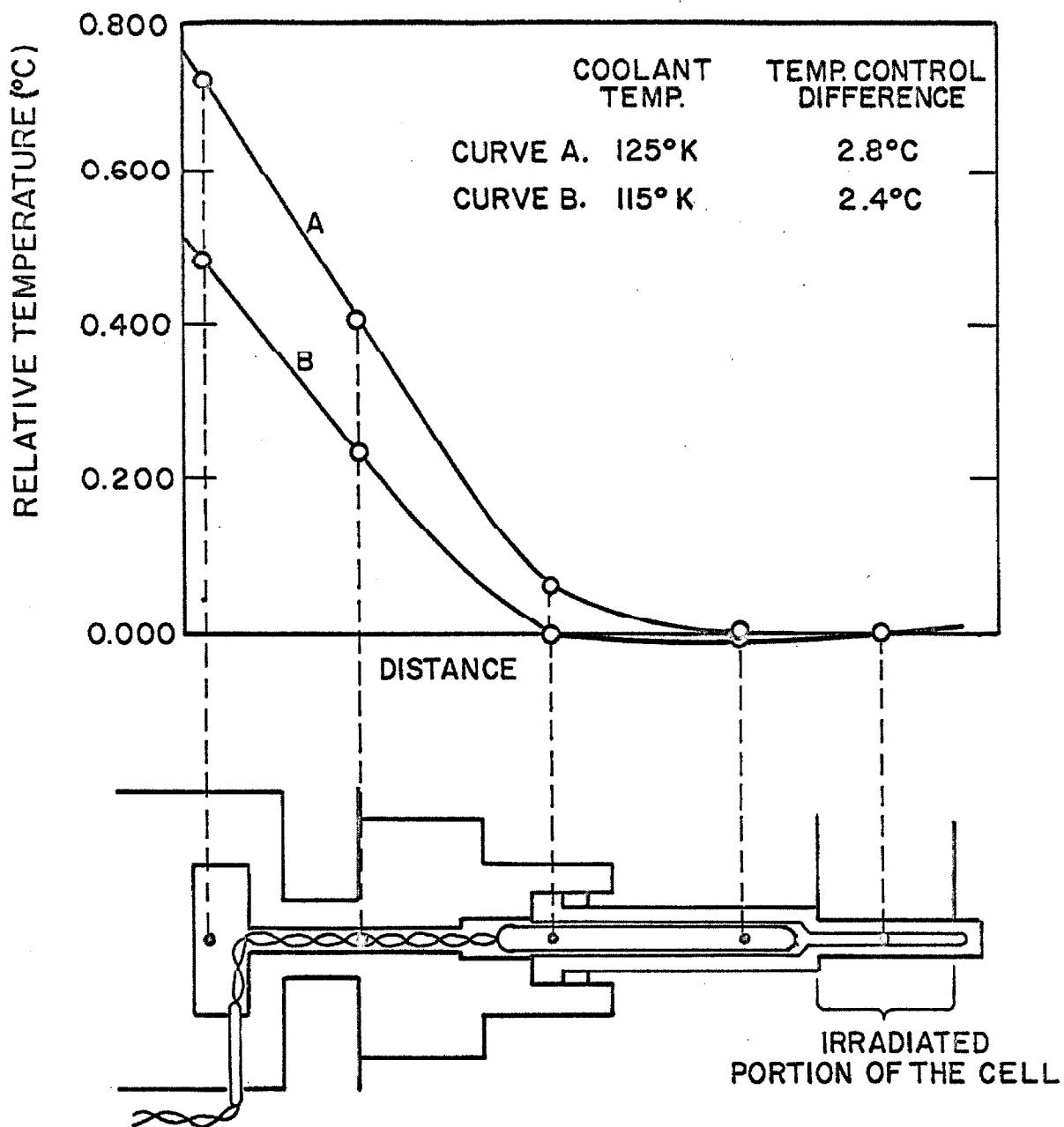
Figure 26. Sample Cell Temperature Profiles
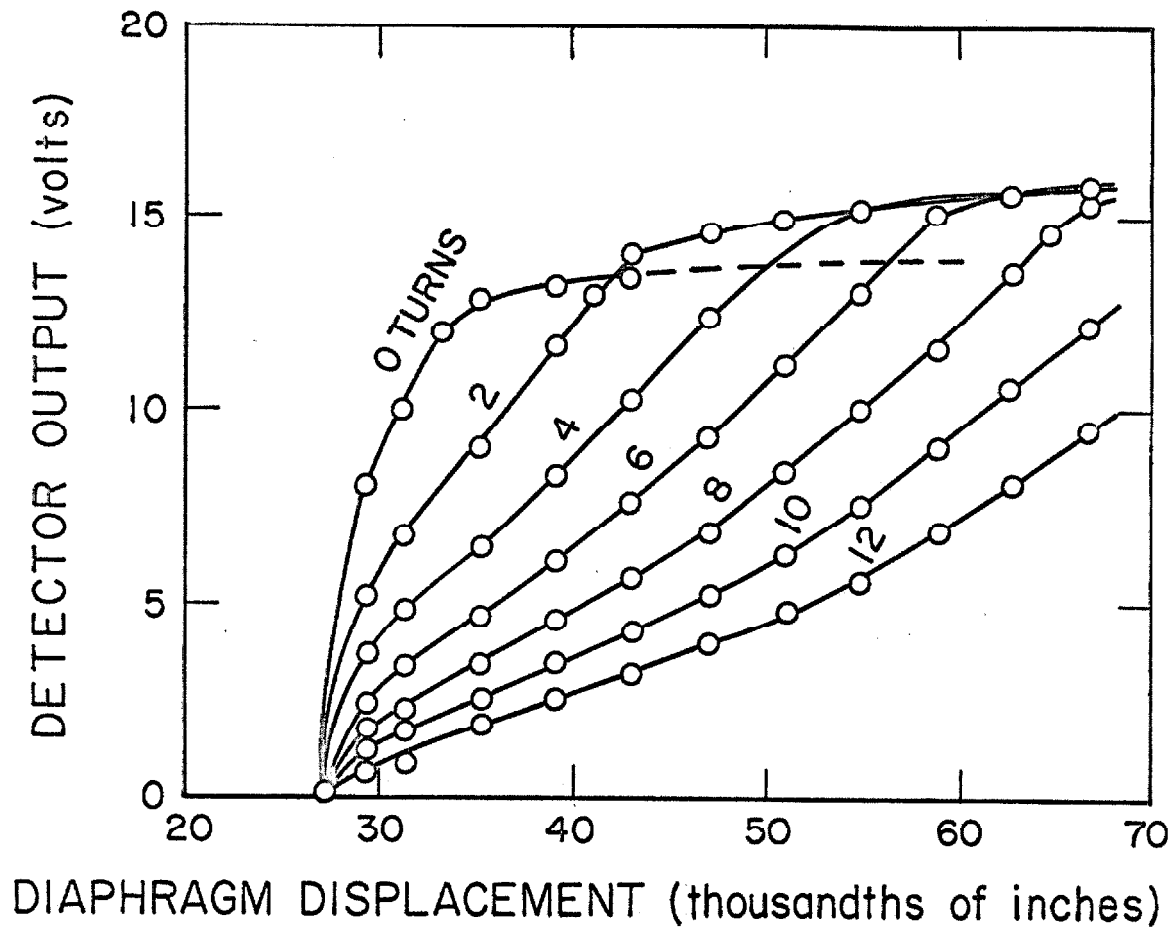
Figure 27. Distance Detector Voltage vs. Distance
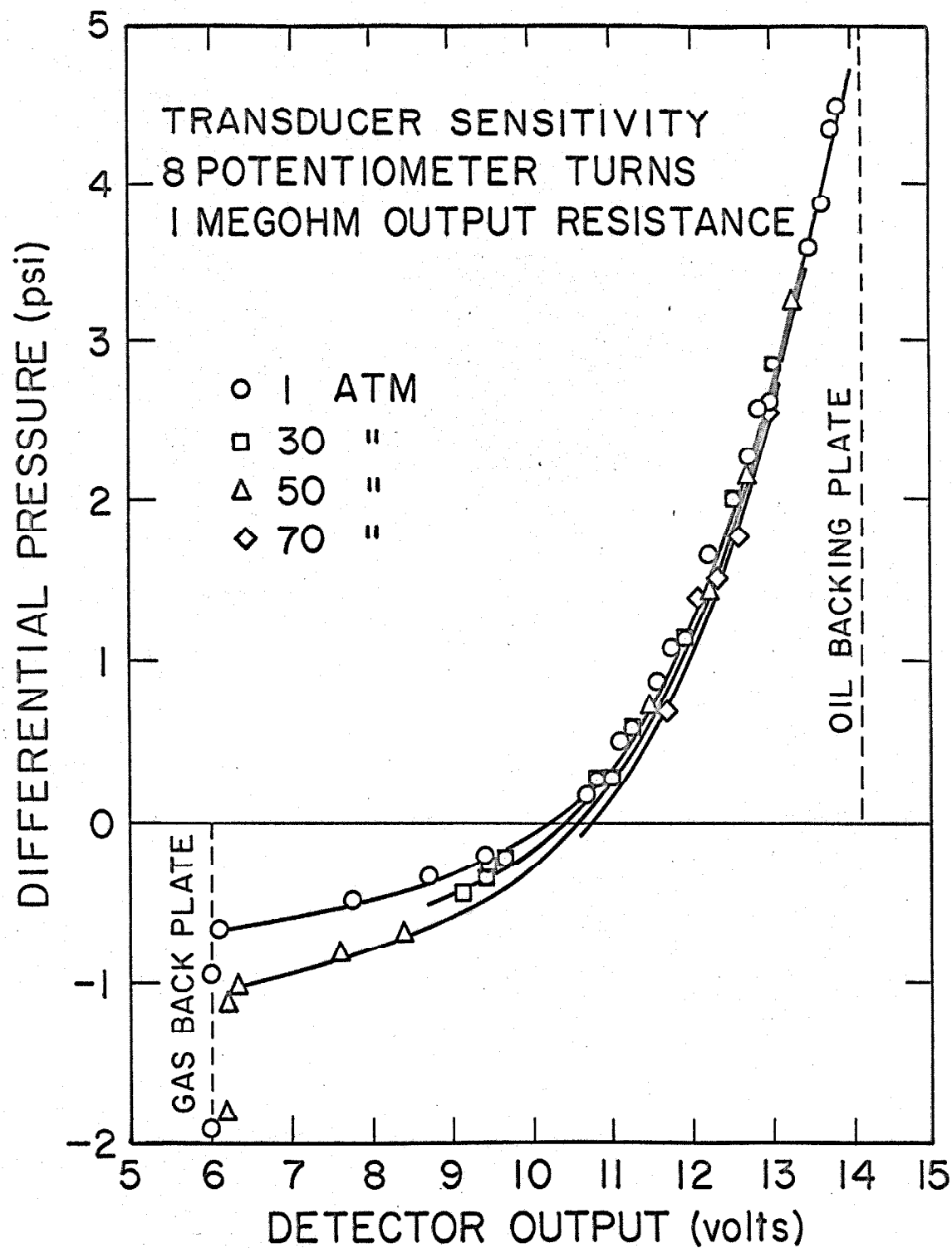
Figure 28. Pressure Transducer Voltage vs. Pressure
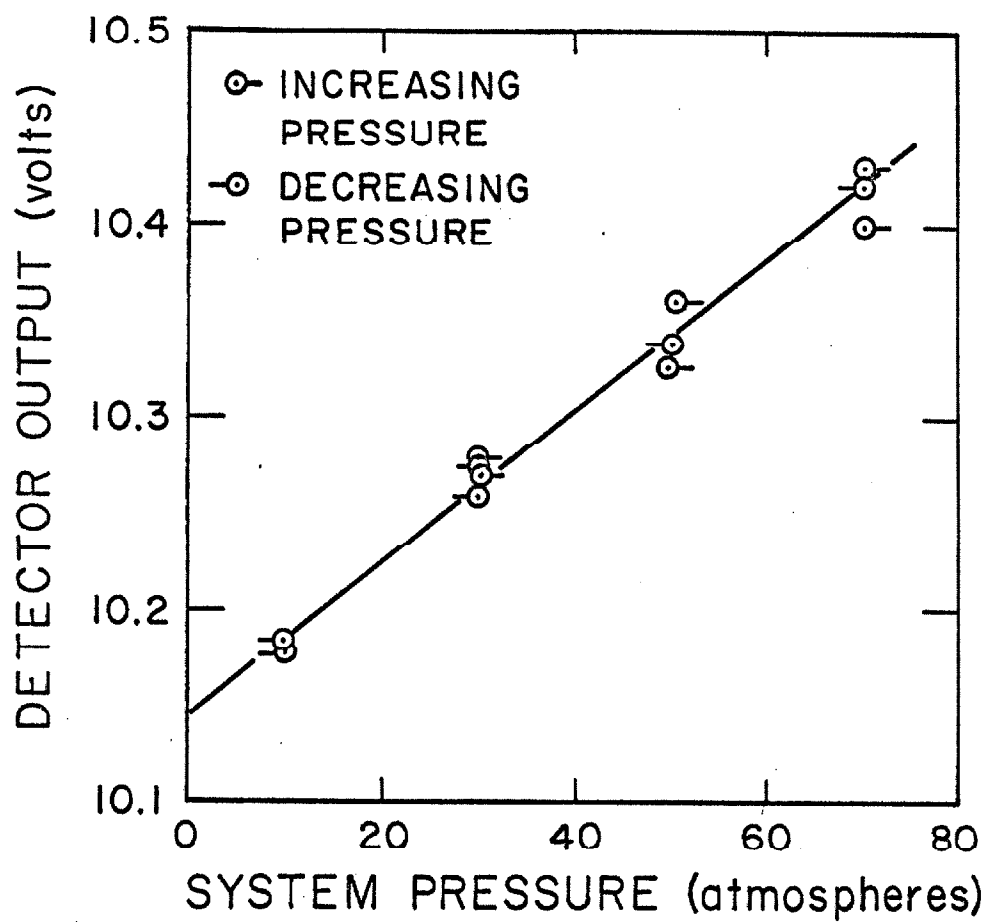
Figure 29. Diaphragm Null Position Voltage vs. Pressure
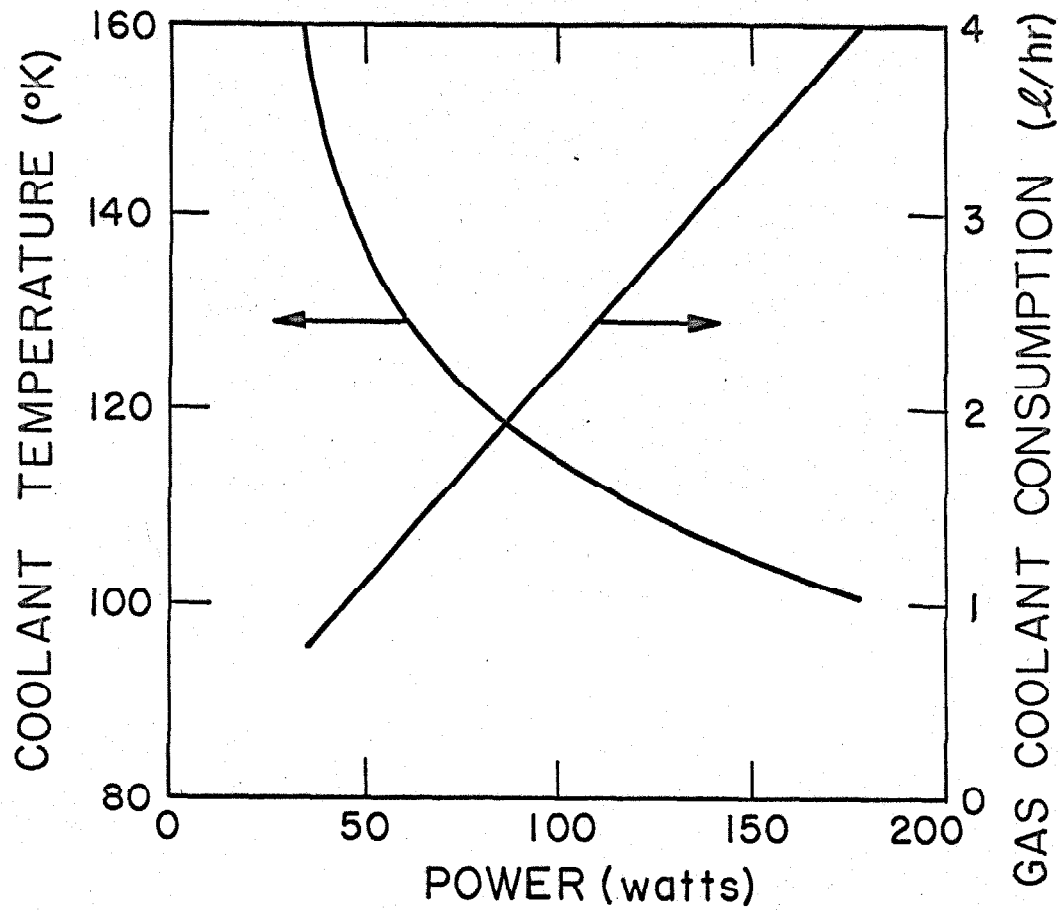
Figure 30. Coolant Temperature and Coolant Consumption
vs. Heater Power
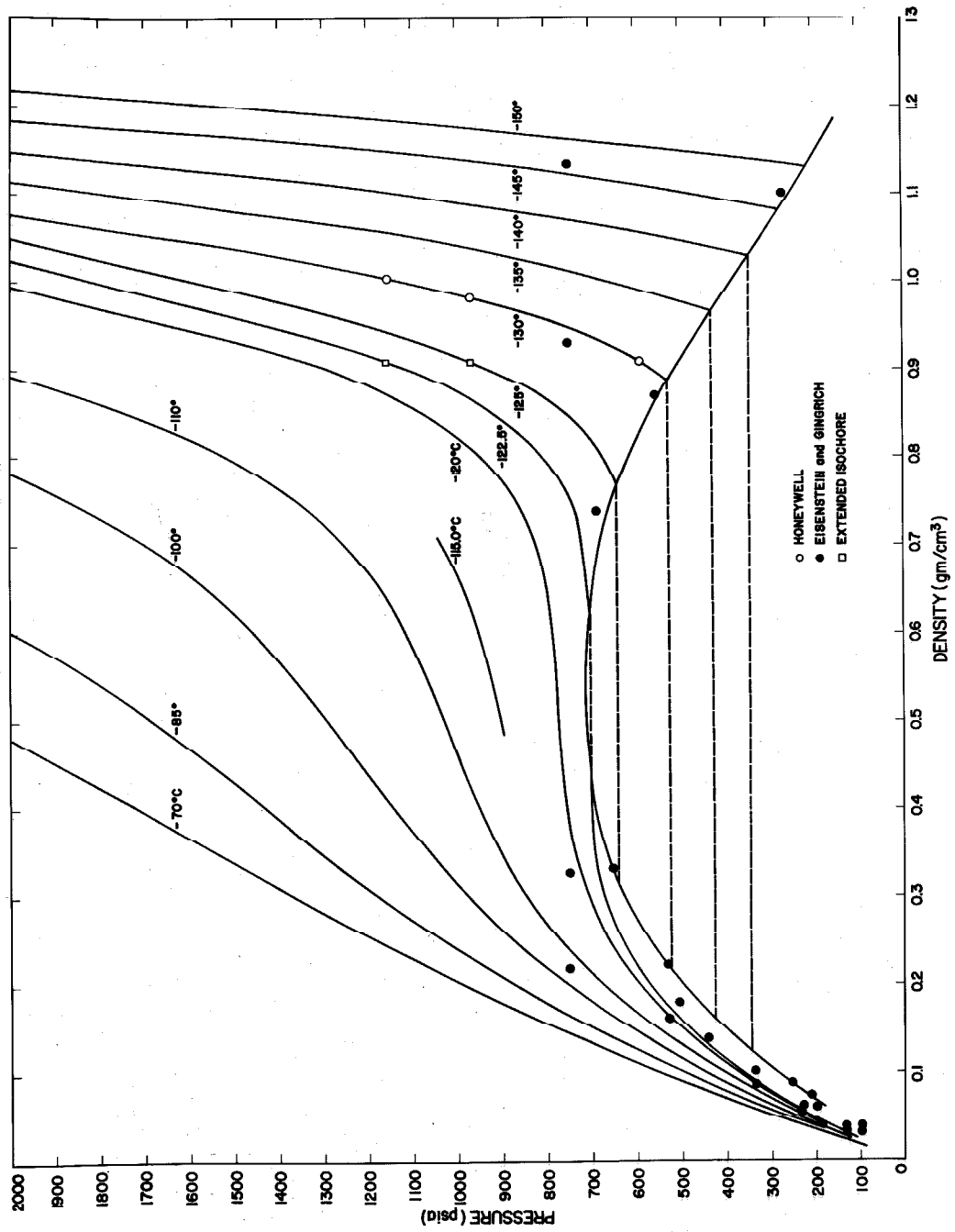
Figure 31. Argon Compressibility Data
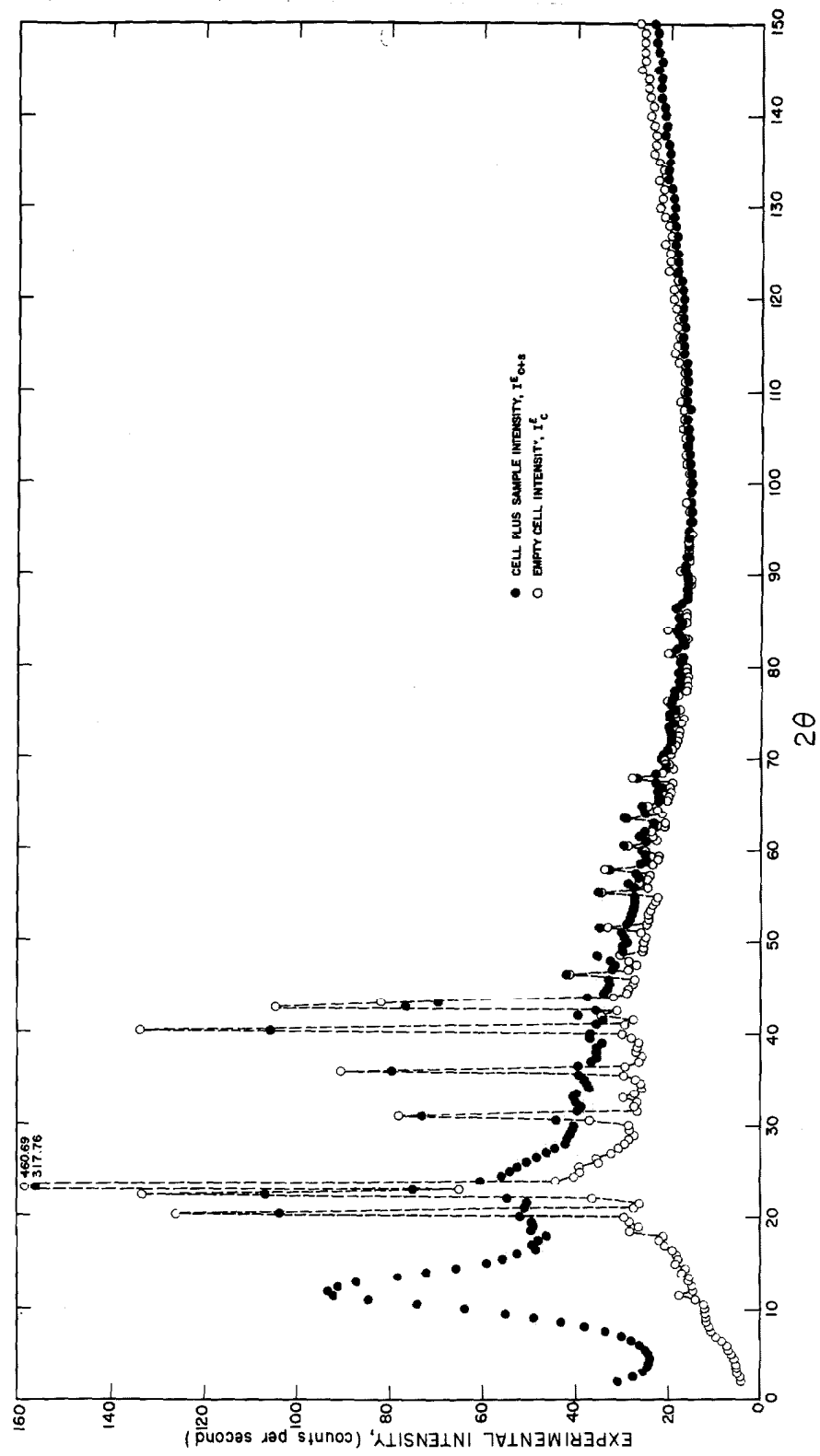
Figure 32. Experimental Intensity vs. Scattering Angle
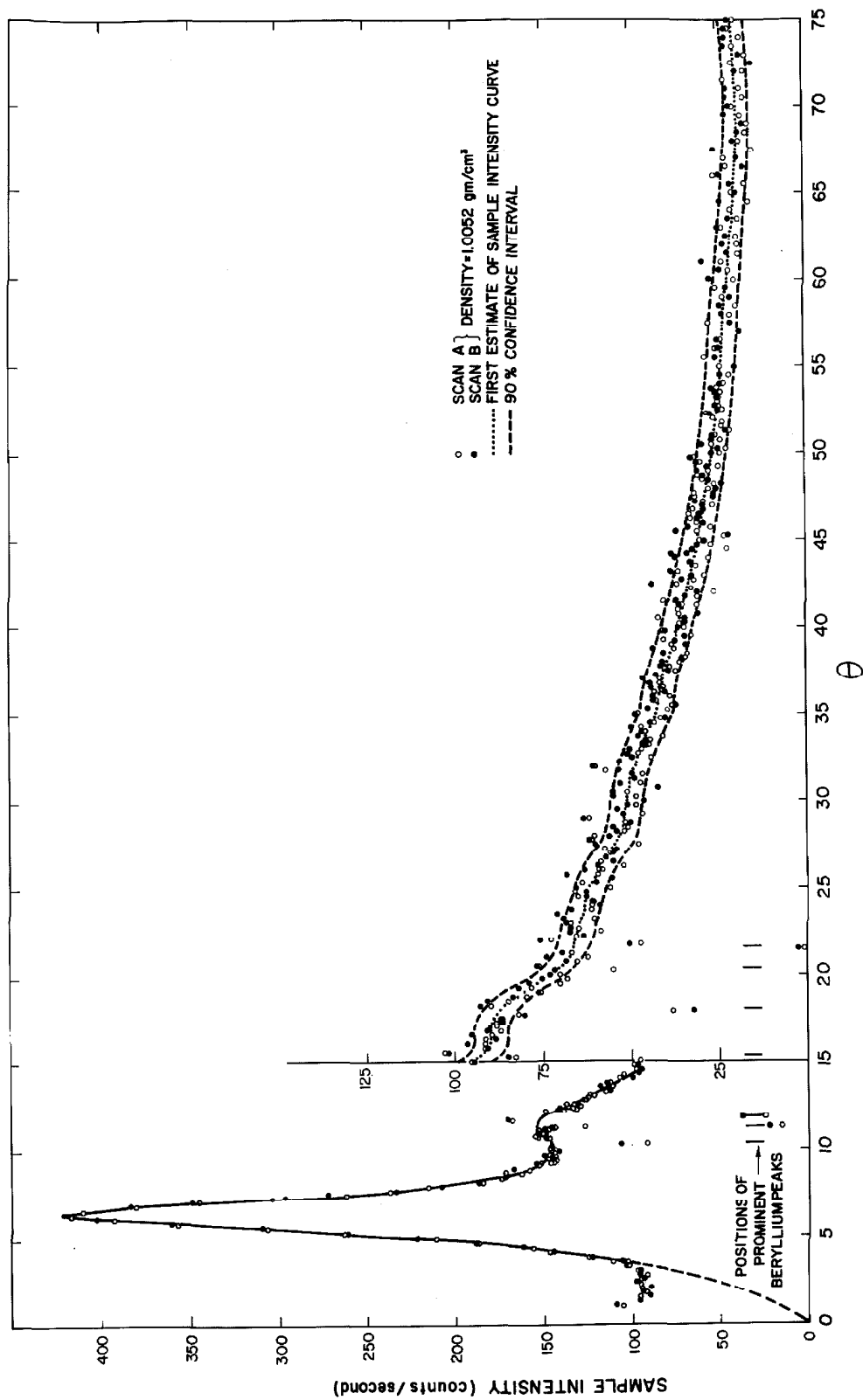
Figure 33. Corrected Sample Intensity vs. Scattering Angle
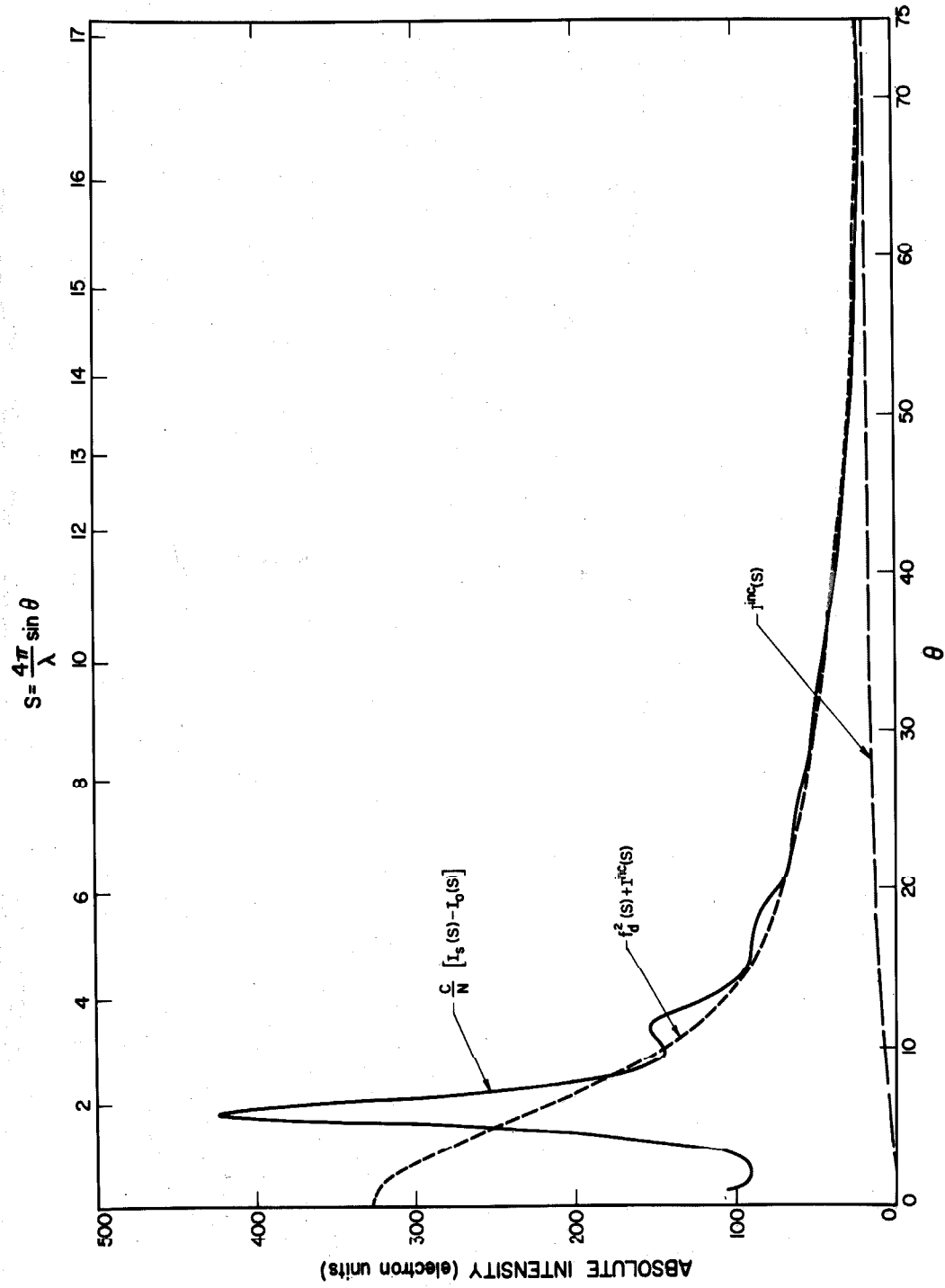
Figure 34. Smoothed Sample Intensities vs. θ
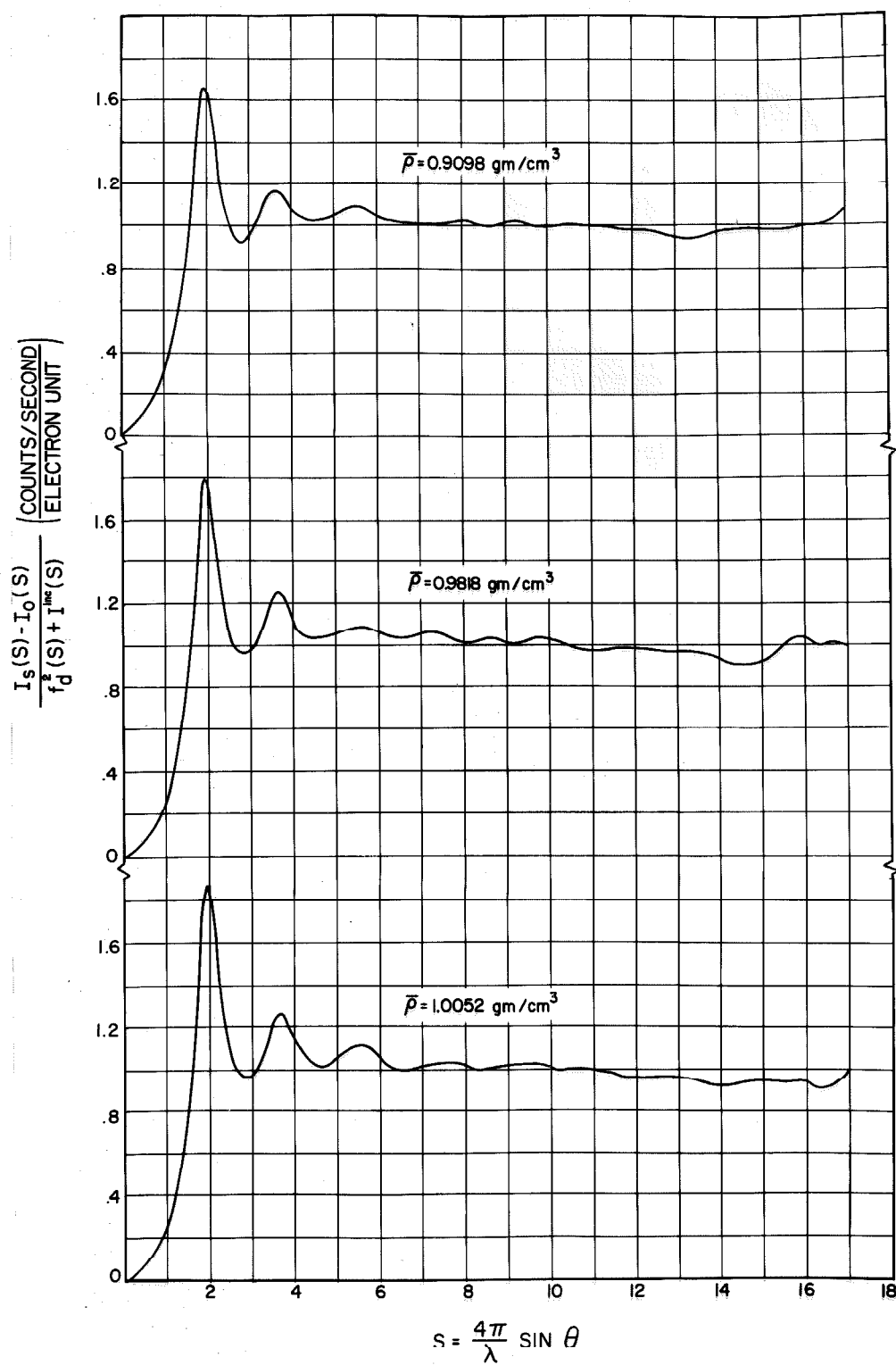
Figure 35. Ratio of Smoothed Sample Intensities to Independent Scattering vs. S
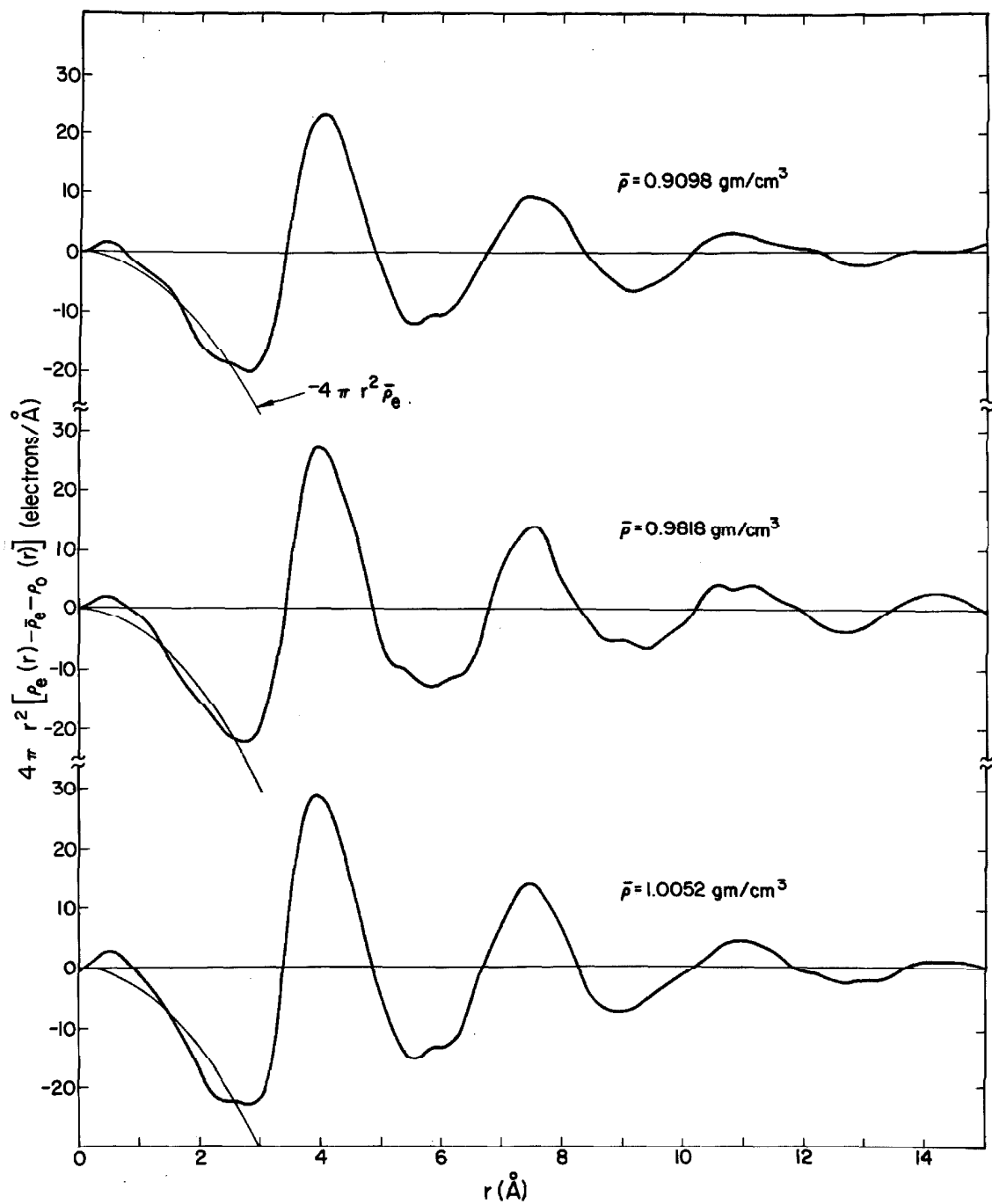
Figure 36. Electronic Radial Densities, Transforms Truncated at $9\,\text{Å}^{-1}$
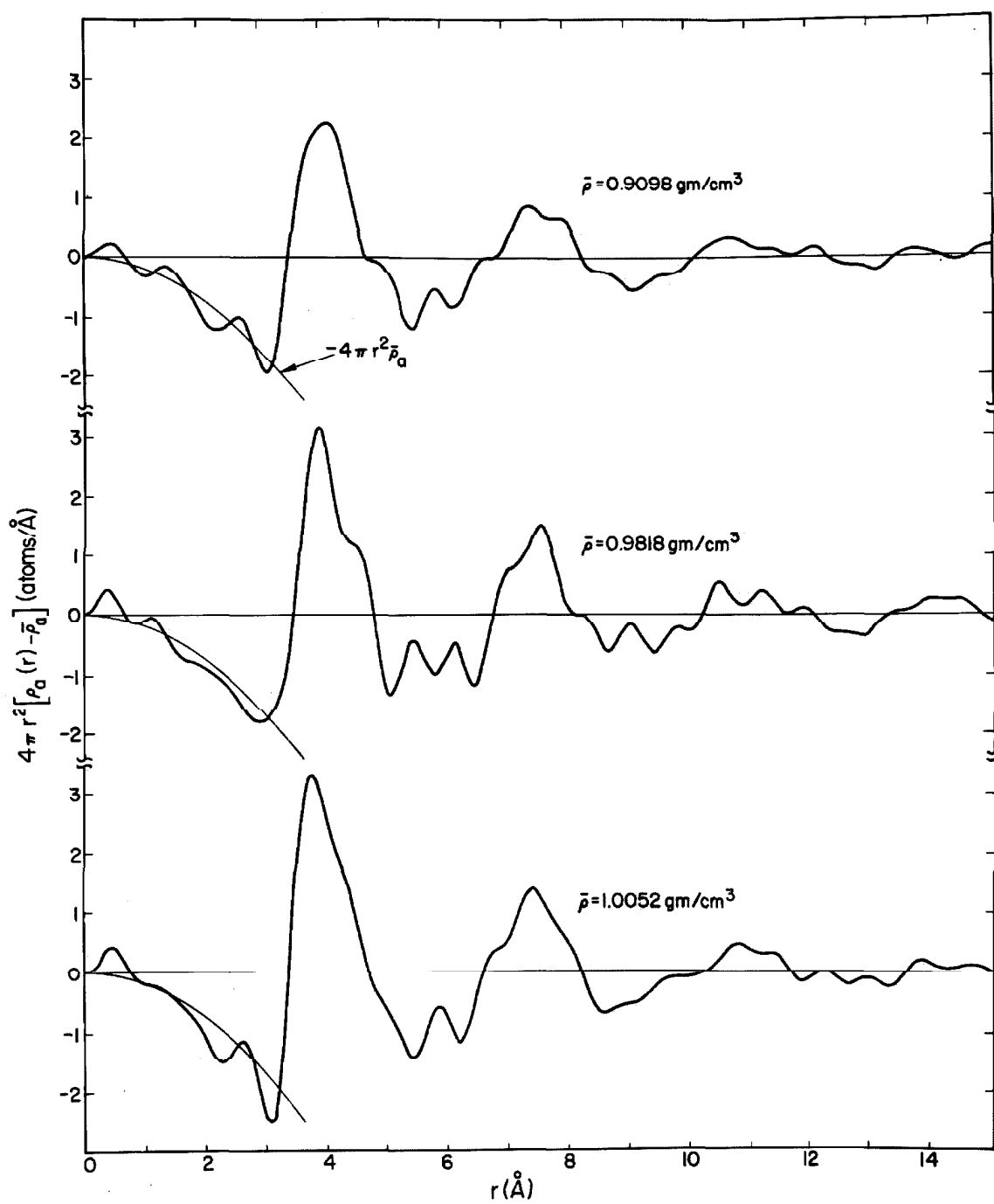
Figure 37. Atomic Radial Densities, Transforms Truncated at 9 $\overset{\circ}{A}^{-1}$
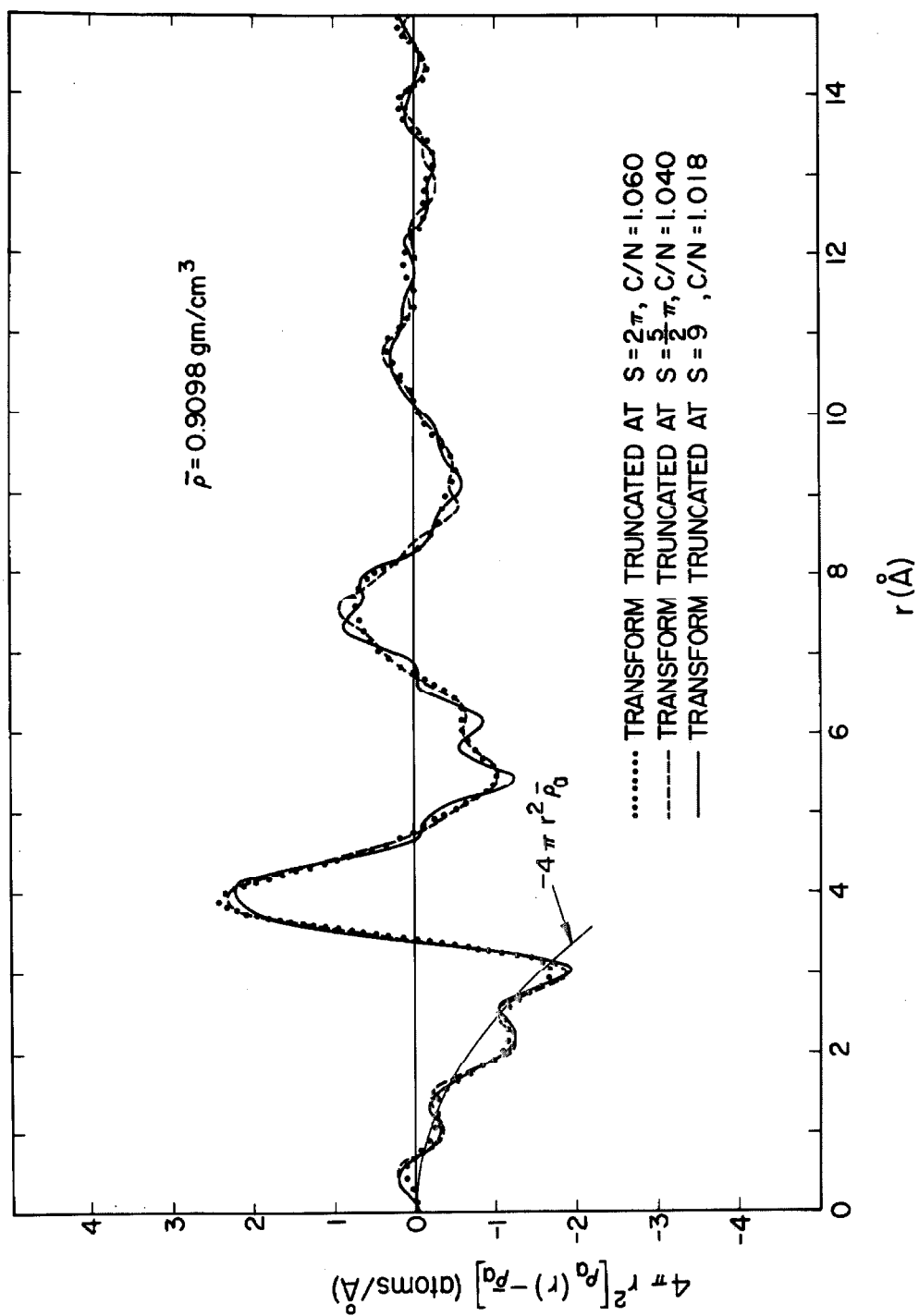
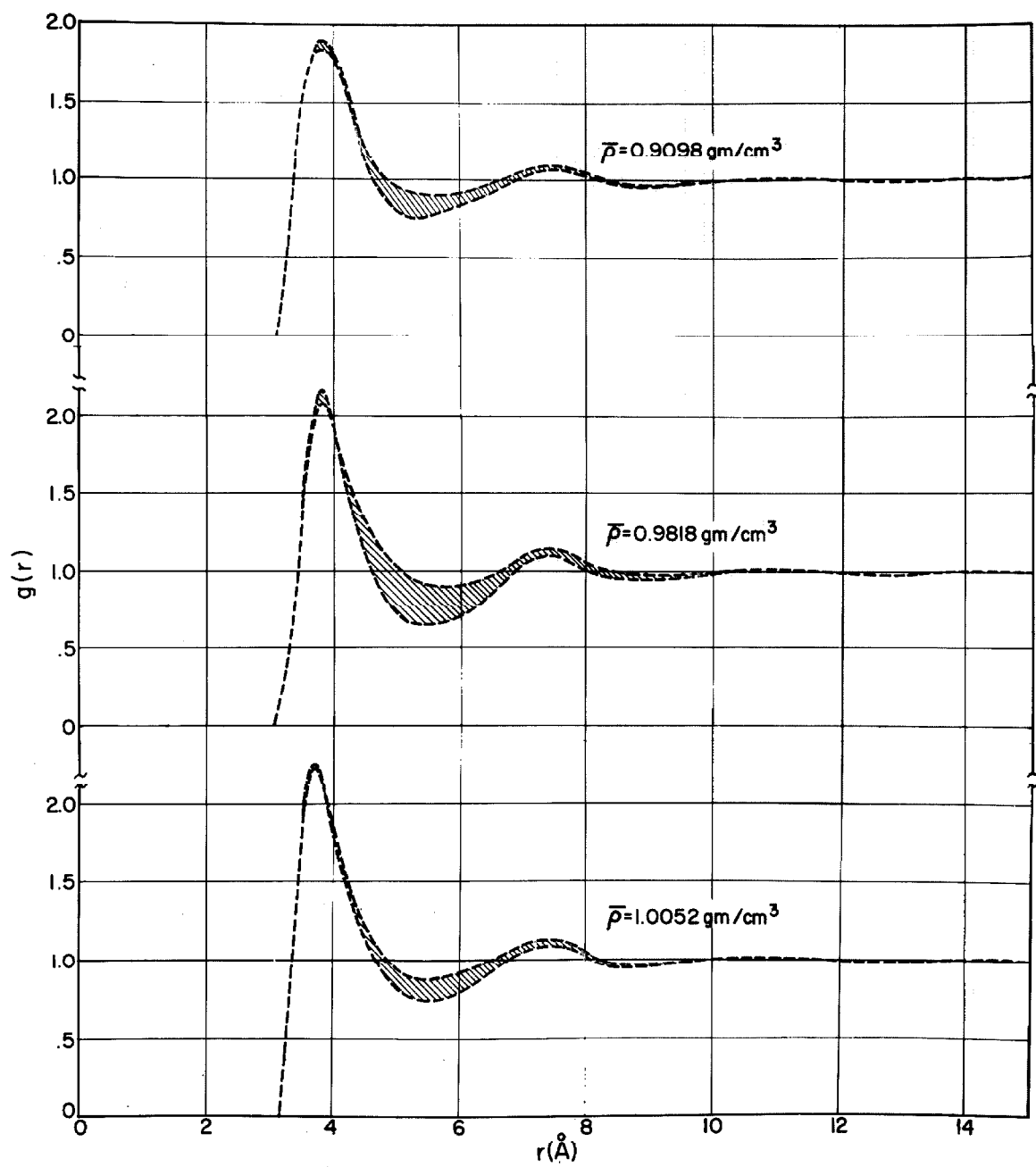Figure 38. Superposition of Atomic Radial Densities for $\bar{\rho} = 0.9098$ gm/cm^3

Figure 39. Estimates of Radial Distribution Functions

LIST OF REFERENCES

1. P. Debye, "Zerstreuung von Rontgenstrahlen," Ann. Physik, 46, 809 (1915).

2. P. Ehrenfest, "On Interference Phenomena to Be Expected when Rontgen Rays Pass through a Diatomic Gas," Proc. Amstr. Acad., 17, 1184 (1915).

3. P. Debye, "Uber die Zerstreuung von Rontgenstrahlen an Amorphes Korpern," Z. Physik, 28, 135 (1927).

4. F. Zernike and J. A. Prins, "Die Beubung von Rontgenstrahlen in Flussigkeiten als Effekt der Molekulanordnung," Z. Physik, 41, 184 (1927).

5. B. E. Warren and N. S. Gingrich, "Fourier Integral Analysis of X-Ray Powder Patterns," Phys. Rev., 46, 368 (1934).

6. V. N. Filipovich, "Theory of Scattering of X-Rays in Gases, Liquids, Amorphous Solid Bodies and Polycrystalline Materials, I & II," Zh. Tekhn. Fiz., 25, 1604, 1622, (1955); English translation, Soviet Phys. Tech. Phys., 1, 391, 409 (1956).

7. J. Waser and V. Schomaker, "The Fourier Inversion of Diffraction Data," Rev. Mod. Phys., 25, 671 (1953).

8. C. Finbak, "The Structure of Modern Liquids. II," Acta.Chem. Scand., 3, 1293 (1949).

9. C. J. Pings and H. H. Paalman, "Structure of Liquid Nitrogen," Mol. Phys., 5, 531 (1962).

10. H. H. Paalman and C. J. Pings, "Fourier Analysis of X-Ray Diffraction Data from Liquids," Rev. Mod. Phys., 35, No. 2, 389 (1963).

11. A. H. Compton and S. K. Allison, X-Rays in Theory and Experiment (Van Nostrand, New York, 1935), p. 117.

12. K. Furukawa, "The Radial Distribution Curves of Liquids by Diffraction Methods," Rept. Prog. Phys., 25, 395 (1962).

13. R. F. Kruh, "Diffraction Studies of the Structure of Liquids," Chem. Rev., 62, 319 (1962).

14. H. H. Paalman and C. J. Pings, "Beryllium Sample Cell for X-Ray Diffraction Study of Liquids," Rev. Sci. Instr., 33, 496 (1962).

LIST OF REFERENCES (Cont'd)

15. S. E. Rodriguez and C. J. Pings, "Cell for X-Ray Diffraction Studies of Absorbing Liquids," Rev. Sci. Instr., 33, 1469 (1962).

16. J. Taylor and W. Parrish, "Absorption and Counting-Efficiency Data for X-Ray Detectors," Rev. Sci. Instr., 26, 367 (1955).

17. W. Parrish and T. R. Kohler, "Use of Counter Tubes in X-Ray Analysis," Rev. Sci. Instr., 27, 795 (1956).

18. G. W. Brady and J. T. Krause, "Structure in Ionic Solutions. I," J. Chem. Phys., 27, 304 (1957).

19. W. L. Gordon, C. H. Shaw, and J. G. Daunt, "Radial Atomic Distribution in Liquid Helium-4 by X-Ray Scattering," J. Phys. Chem. Solids, 5, 117 (1958); also M. Sawada and C. H. Shaw, "Calculation of the Transmission Factor in X-Ray Scattering," J. Appl. Phys., 29, 1344 (1958).

20. H. H. Paalman, "An X-Ray Diffraction Study of Liquid Structure," doctoral thesis, Stanford University (1961).

21. J. Intrater and S. Hurwitt, "High Temperature, High Vacuum, Diffractometer Attachment," Rev. Sci. Instr., 32, 905 (1961).

22. L. K. Jetter, C. J. McHargue, P. O. Williams, and H. L. Yakel, Jr., "Low-Temperature Camera for X-Ray Diffractometer," Rev. Sci. Instr., 28, 1087 (1957).

23. C. A. Stochl and S. G. Ullman, "Liquid Helium Dewar Attachment for an X-Ray Diffractometer," Rev. Sci. Instr., 34, 1134 (1963).

24. J. H. Hoskins, "Universal Vacuum X-Ray Spectrograph," Norelco Reporter, VII, No. 4, 111 (1960).

25. E. W. Comings, High Pressure Technology (McGraw-Hill, New York, 1956), p. 95.

26. R. B. Scott, Cryogenic Engineering (Van Nostrand, Princeton, 1959), p. 254.

27. H. H. Reamer and B. H. Sage, "Manostat for High-Pressure Operations," Rev. Sci. Instr., 29, 709 (1958).

28. E. M. Butcher and M. Alsop, "Diaphragm-type Pressure Balance Detector," J. Sci. Instr., 39, 483 (1962).

LIST OF REFERENCES (Cont'd)

29. J. O. Cope, "Direct Reading Diaphragm-Type Pressure Transducer," Rev. Sci. Instr., 33, 980 (1962).

30. A. Michels, "Genauigkeit und Empfindlichkeit einer Druckwage mit einem Sogenannten Amagatzylinder," Ann. Physik, 73, 577 (1924).

31. H. Klug and L. Aleaxander, X-Ray Diffraction Procedures (John Wiley & Sons, Inc., New York, 1954), p. 446.

32. R. J. Corruccini, "Interpolation of Platinum Resistance Thermometers, 10° to 273.15^{o}K," Temperature, Its Measurement and Control in Science and Industry, Vol. 3, Part 1 (American Institute of Physics, Reinhold, New York, 1962), p. 329.

33. R. B. Scott, "The Calibration of Thermocouples at Low Temperatures," Temperature, Its Measurement and Control in Science and Industry, Vol. 1 (American Institute of Physics, Reinhold, New York, 1941), p. 206.

34. E. Gruneisen, "Die Anderung des Druckkoeffizienten des Metallischen Widerstands mit der Temperatur," Ann. Physik, 40, 543 (1941).

35. F. C. Blake, "On the Factors Affecting the Reflection Intensities of Crystal Structures by the Several Methods of X-Ray Analysis," Rev. Mod. Phys., 54, 169 (1933).

36. H. L. Ritter, R. L. Harris, and R. E. Wood, "On the X-Ray Absorption Correction for Encased Diffractors in the Debye-Scherrer Technique," J. Appl. Phys., 22, 169 (1951).

37. H. H. Paalman and C. J. Pings, "Numerical Evaluation of X-Ray Absorption Factors for Cylindrical Samples and Annular Sample Cells," J. Appl. Phys., 33, 2635 (1962).

38. A. P. Kendig and C. J. Pings, "X-Ray Absorption Factors for Partially Exposed Annular Sample Cells," in preparation.

39. Compton and Allison, op. cit., p. 206.

40. B. D. Cullity, Elements of X-Ray Diffraction (Addison-Wesley Pub. Co., Inc., Reading, Mass., 1956), p. 11.

41. Klug and Alexander, op. cit., p. 596.

LIST OF REFERENCES (Cont'd)

42. P. G. Mikolaj, doctoral thesis in preparation, California Institute of Technology.

43. Cullity, op. cit., p.466.

44. W. E. Milne, Numerical Calculus (Princeton University Press, 1949), p.68.

45. J. Krogh-Moe, "A Method for Converting Experimental X-Ray Intensities to an Absolute Scale," Acta. Cryst., 9, 951 (1956).

46. N. Norman, "The Fourier Transform Method for Normalizing Intensities," Acta. Cryst., 10, 370 (1957).

47. J. Berghuis, I. M. Haanappel, M. Potters, B. O. Loopstra, C. H. MacGillavry, and A. L. Veenendaal, "New Calculations of Atomic Scattering Factors," Acta. Cryst., 8, 478 (1955).

48. D. R. Chipman and L.D. Jennings, "Measurement of the Atomic Scattering Factor of Ne, Ar, Kr, and Xe," Phys. Rev., 132, No. 2, 728 (1963).

49. R. W. James, The Optical Principles of X-Rays (Bell & Sons, Ltd., London, 1958), p. 608.

50. A. J. Freeman, "A Study of the Compton Scattering of X-Rays. II," Acta. Cryst., 13, 190 (1960).

51. H. W. Furumoto, "Diffraction of X Rays by Liquids — Nitrogen, Oxygen, and Their Mixtures," doctoral thesis for Dept. of Physics, Ohio State University (1963), p. 58.

52. R. James and G. Grindley, "Some Numerical Calculations of Atomic Scattering Factors," Phil. Mag., 12, 81 (1931).

53. R. W. James, op. cit., p. 463.

54. Compton and Allison, op. cit., p. 234.

55. J. M. H. Levelt, "Measurements of the Compressibility of Argon in the Gaseous and Liquid Phase," doctoral thesis, Amsterdam (1958), p. 38; this work also reported in A. Michels, J. M. Levelt, and G. J. Wolkers, "Thermodynamic Properties of Argon at Temperatures between $0°$ and $-140°$C. and at Densities up to 640 Amagat (Pressures up to 1050 atm.)," Physica, 24, 769 (1958).

LIST OF REFERENCES (Cont'd)

56. A. Eisenstein and N. S. Gingrich, "The Diffraction of X-Rays by Argon in the Liquid, Vapor, and Critical Regions," Phys. Rev., 62, 261 (1942).

57. L. Holborn and J. Otto, "Uber die Isothermen von Helium, Stickstoff, und Argon unterhalb 0°," Zeit. f. Physik, 30, 320 (1924).

58. H. S. Pieser, H. P. Rooksby, and A. J. C. Witson, X-Ray Diffraction by Polycrystalline Materials (The Institute of Physics, London, 1955), p. 222.

59. P. G. Hoel, Introduction to Mathematical Statistics (John Wiley & Sons, Inc., New York, 1947), p. 101.

60. W. Parrish, "X-Ray Intensity Measurements with Counter Tubes," Philips Technical Review, 17, No. 7-8, 206 (1956).

61. C. A. Coulson and G. S. Rushbrooke, "On the Interpretation of Atomic Distribution Curves for Liquids," Phys. Rev., 56, 1216 (1939).

62. K. Furukawa, "A Structural Model for Monatomic Liquids Including Metallic Liquids," Nature, London, 184, 1209 (1959).

63. W. W. Wood and F. R. Parker, "Monte Carlo Equation of State Molecules Interacting with the Lennard-Jones Potential. I. A Supercritical Isotherm at About Twice the Critical Temperature," J. Chem. Phys., 27, 720 (1957).

64. J. D. Bernal, "Geometry of the Structure of Monatomic Liquids," Nature, London, 185, 68 (1960).

65. D. G. Henshaw, "Atomic Distribution in Liquid Argon by Neutron Diffraction and the Cross Sections of A36 and A40," Phys. Rev., 105, No. 3, 976 (1957).

66. Z. W. Wilchinsky, "Effect of Crystal Grain and Particle Size on X-Ray Power Diffracted from Powders," Acta. Cryst., 4, 1 (1951).

67. J. N. Eastabrook, "Effect of Vertical Divergence on the Displacement and Breadth of X-Ray Powder Diffraction Lines," Brit. J. Appl. Phys., 3, 349 (1952).

APPENDIX I

ELECTRONIC COMPONENTS ASSOCIATED WITH X-RAY
PRODUCTION AND DETECTION

The following is a list of the major electronic components which were used in the present experimental arrangement in connection with the production and detection of x rays. Their function is briefly described in Section II.

1. Norelco X-ray Generator, Type 12045; 10-60 kv-p fullwave rectified output: maximum output 2500 watts.

2. Norelco X-ray Diffraction Tube, Cat. No. 32113, Molybdenum target.

3. Scintillation Counter and Power Supply; 1/2 in. diameter crystal of thallium activated sodium iodide mounted on Type 6201V22 multiplier phototube; phototube power supply, Norelco D. C. Power Supply 0-1900V with Electronic Circuit Panel.

4. Franklin Electronics Preamplifier, Model 349; voltage gain 0.98, input noise (grounded grid) less than 25 microvolts.

5. Franklin Electronics Linear Amplifier, Model 348A DD-2; maximum gain 50,000; gain stability 1% for 10% line voltage change, input noise 50 microvolts maximum.

6. Nuclear Chicago Pulse Height Analyzer, Model 8300; integral and differential output, motor driven scanning base control, base range 5 v to 100 v, maximum count rate 250,000 pulses/sec, output 15 v negative, 1 μsec pulse pair resolution, ± 0.1% base line linearity over full range.

7. Franklin Electronics Precision Pulse Generator, Model 370; 10 volt maximum output, stability 0.02% per day.

8. Computer Measurements Corporation Dual Preset Controller, Model 326B; input sensitivity 0.05 volt runs for $10\text{-}10^4$ cps, absolute accuracy.

9. Computer Measurements Corporation Counter Timer, Model 226B; $0 - 1.2 \times 10^6$ cps ± 1 count $\pm$ stability, six digit readout, 0.1 volt rms input sensitivity.

10. Computer Measurements Corporation Digital Printer, Model 400C; six digit recording and indicating capacity, absolute accuracy of counting instrument.

APPENDIX II

DETAILED ALIGNMENT AND OPERATING PROCEDURE

The following set of instructions is included to assist those
who have not previously operated the equipment or to refresh the memory
of those who have.

1. Goniometer and Soller Slit Alignment

The goniometer must first be aligned. Either the suggestions in
the Norelco instruction manual or the improvised laboratory procedure
may be used for this purpose.

The vertical Soller slits and receiving slit can then be aligned.
The object is to place the slit plates parallel to a ray from the
center of the goniometer through the center of the receiving slit.
First, place the 2 to 1 gauge in the goniometer alignment jig. When
it is properly aligned, a very narrow pencil of x rays passes through it
and fixes the zero of the goniometer. Next, place the 0.006-in. receiv-
ing slit in the slit holder. With the Soller slits in place, rotate
the slits in their holder and adjust the angular setting of the counter
until the maximum intensity is obtained. The set screws holding the
Soller slit holder in place should not be strongly tightened. Now
remove the Soller slits and scan the main beam to find the true zero
for the 0.006-in. receiving slit.

Next, insert the 0.111-in. receiving slit, or whatever slit will
be used in the experiment runs. The center of this slit should corres-
pond roughly to the center of the 0.006-in. slit. To see if it does,

scan the main beam again without the Soller slits. If the two zeros agree reasonably well, the goniometer zero may be set and the Soller slits replaced. If the zeros do not agree, the entire procedure must be repeated allowing for the difference. Two iterations are usually sufficient.

2. Alignment of the Vacuum Chamber

The position of the vacuum chamber determines the cell alignment. The axis of the cell is parallel to the goniometer axis when the vacuum chamber end plate is parallel to the hub on the goniometer shaft. The vertical and horizontal alignment is accomplished by moving the chamber in the scattering plane with the adjustment screws on the base plate which holds the wooden support block.

The chamber is first roughly positioned against the hub with the goniometer shaft moved out about two inches. This permits access to the bolts holding the hub to the end plate. The base plate should be moved in toward the goniometer as far as possible. Position the chamber parallel to the hub by adjusting the alignment screws on the base plate. With the hub flush against the end plate, a 0.002-in. thickness gauge would not slip in around the edges of the hub.

Now back the hub off a short distance and check to see if the two alignment pins in the hub will fit into the holes in the end plate. They should not bind in the end plate holes when the hub is in place. If they do, the can must be repositioned, and the alignment process repeated. Once the chamber is near final alignment, a level should be placed on top of the pressure manifold housing. The top of the housing

must be horizontal in the direction of the goniometer axis; it should also be roughly horizontal in the scattering plane to permit proper alignment of the coolant transfer tubes.

The alignment procedure usually needs to be repeated several times before the chamber is properly positioned. When the alignment pins slide freely into place, the hub may be bolted lightly to the chamber. Slide the wooden block in along the runners until the center of the Mylar window coincides with the notch on the horizontal Soller slits; this notch indicates the center of the x-ray beam. Be very careful when sliding the wooden block not to disturb the goniometer or move the chamber on the block. When the chamber is properly positioned, the goniometer shaft should be locked into place with the clamp on the far side of the goniometer.

3. Preliminary Operations Before Beginning an Experimental Run

Several preliminary operations and checks are necessary before the beginning of a run. The x-ray counting equipment should be left in operation continuously to insure stability. Each component should be checked occasionally according to the appropriate calibration procedures. In particular, the alignment of the decades on the CMC equipment should be checked frequently.

The distance detector electronics must be turned on well in advance of their intended use. The operating characteristics are sensitive to temperature, and thermal steady state must be established.

The potentiometer batteries should be well charged. This check is an easy one to forget. But well-charged batteries are very important

to the proper functioning of the apparatus, especially when the plati-num resistance thermometer is used for temperature control. Since the batteries must be hooked up to the thermometer early to avoid discharge transients, they should be charged well in advance of the experimental run.

The coolant transfer tube is not evacuated continuously during a run; it must be pre-evacuated to the desired pressure. It was found that the simple inlet valve to the evacuated line held an adequate vacuum for several weeks.

The correct cylinder must be installed in the pressure balance well ahead of its use. Air must be bled from the lines for several hours after the cylinder is installed.

After all of the above operations have been performed, evacuation of the vacuum chamber and sample lines may be begun. When pumping the chamber down from atmospheric pressure, at least ten hours are required to reduce the pressure below one micron. The time requirement will vary, however, with the pumping system and the history of the chamber pressure. The sample lines should be evacuated (independently if pos-sible) and flushed several times with sample prior to the cooling-down procedure. The cell should be flushed with sample at pressures less than one atmosphere (absolute) to avoid overpressurizing the diaphragm.

4. Cooling Procedure

After a pressure less than one micron of Hg is reached in the vacuum chamber, the coolant transfer tube may be attached and cooling begun. There are two different methods available for coolant operation,

either gas or liquid flow. Liquid flow cooling is used for control temperatures between 80° and 110° K. For this mode of flow, the transfer tube extends to the bottom of the coolant supply Dewar.

For control temperatures above 110° K, gas flow cooling is used. The coolant transfer tube is inserted in the supply dewar until the end extends a short distance below the liquid level. With experience, the distance may be chosen so that liquid flow will occur during initial cooling; then near the control temperature gas cooling will begin.

The coolant flow rate is selected to give the optimum cell temperature profile for the desired control temperature (see Figure 26). The appropriate heater voltage for transfer of the coolant is selected from the gas coolant consumption curve (see Figure 30). Very small voltages are required to transfer the liquid coolant after the initial pressure has been established in the supply Dewar.

As the cell assembly cools, the vacuum in the chamber increases rapidly due to cryopumping. When the pressure falls below 10^{-4} mm Hg, the vacuum ion pump may be put into operation. The rough pumping lines are then shut off from the vacuum chamber and left pumping on the sample line. A warmup period of over one hour is sometimes required for the ion pump before it reaches its maximum pumping speed. During this time, the roughing line must remain connected to the chamber.

During the cooling operation, the temperature of the control annulus may be displayed on the recorder. The reference voltage must be included in the control circuit to make the thermocouple voltage compatible with the recorder range. The absolute temperature may be

checked by measuring the thermocouple potential with the potentiometer; the potential must be adjusted from the usual thermocouple tables since the reference junction is at room temperature.

An additional hour is usually required for the gas coolant flow rate to stabilize after the control temperature is reached. Since the adjustment is usually toward a higher temperature, the steady coolant temperature should be observed before automatic temperature control is begun.

5. Automatic Temperature Control

When the desired coolant temperature is steady, begin automatic temperature control. Connect the temperature control apparatus according to the schematic of Figure 10. The polarities should be checked with the plugboard wiring diagrams from control records for previous runs.

The control conditions are selected to give minimum cell temperature gradients at the control temperature. Establish the appropriate potentials on the reference voltages with the use of the potentiometer; then connect them into the automatic control circuit.

Before turning on any of the temperature control equipment, recheck the wiring connections. Also check the heaters for continuity; an open circuit may be an indication of a blown fuse.

The two control circuits are activated independently; the absolute thermocouple circuit (referred to as the primary) is activated first. Turn on the magnetic amplifier first, before turning on the Series 60 controller. This procedure is very essential to avoid switch-

-162-

ing transients which in the past have burned out the cell assembly heaters. Then, with the controller on the manual mode and zero current, switch the controllers on. With the manual control knob, increase the current to the primary heater slowly until the temperature record on the recorder indicates the control point has been reached. Maintain manual control until the control record is steady on the desired sensitivity range. Then, with the proper control settings established on the Series 60 controller, switch the control knob quickly from manual to automatic. The temperature should be quite steady and near the recorder control point before switching over.

When the automatic temperature control is satisfactorily steady, incorporate the secondary circuit into the control system in the same manner. The current to the secondary heater should be increased slowly enough to permit the automatic control of the primary heater to react evenly.

6. Final Cell Alignment and Empty Cell Check Points

After temperature control has been established and the cell is still evacuated, the final cell alignment is determined. The main beam is scanned at very low intensity in the absence of a divergence slit. The vertical position of the cell can be determined accurately from the absorption pattern (see Section III.D.3). The horizontal position of the cell should also be determined if it has not been done since previously moving the vacuum chamber into place.

The incident beam is then positioned by a trial and error process. The appropriate divergence slit is installed, and the incident beam is

scanned. If the beam is not in the desired position, the slit holder is rotated slightly, and the incident beam is scanned once again. The process is repeated until the beam is properly positioned.

Next, the pulse amplitude distribution of the diffracted beam is taken with the x rays at their desired operating intensity. After the distribution has been determined, the transmission window is established on the pulse height analyzer. Then the empty cell check point intensities are measured. If diffraction scans of the evacuated cell are to be taken, they may now be begun. If, however, the cell plus sample intensities are to be measured, the sample must first be loaded into the cell.

7. Sample Loading

The sample system has remained under vacuum during the initial cooling period and while temperature control was being established. Sample may now be loaded into the cell. The diaphragm position should be monitored during the filling operation to avoid overpressures. The output of the distance detector is displayed on the 0-10 millivolt range of the recorder by opposing the signal with an appropriate reference voltage. The reference voltage should be selected to put the null position voltage of the transducer near the center of the recorder scale.

Before bleeding sample into the cell, make certain that the valves connecting the oil side of the diaphragm to the pressure bench and Heise gauges are open, and that the oil lines to other systems are closed. The oil in the pressure bench should remain at atmospheric

pressure during the first part of the sample loading operation.

Now close the vacuum line to the cell both at the vacuum valve on the evacuation line and at the high-pressure valve on the pressure manifold. Then bleed a small amount of sample into the cell through the other high-pressure valve on the manifold. The pressure may be raised to approximately one atmosphere by balancing the oil pressure as indicated on the pressure transducer. The ion pump current should be watched closely at this time; any leaks into the vacuum chamber from the sample system will ruin the chamber vacuum.

If the platinum resistance element is to be used for temperature control, connect it now into the control system. Establish the desired control voltage on the potentiometer, and use this as the reference voltage for the thermometer circuit. Automatic temperature control is established with the thermometer in the same manner as was done earlier with the control thermocouple.

The sample pressure and oil pressure are now increased simultaneously while holding the diaphragm near the null position. Maintain a slight positive oil pressure as a precautionary measure during the pressurization of the sample. With one man operating the manual pump on the pressure bench and another controlling the bleed valve on the pressure manifold, the sample can be loaded smoothly and continuously. Do not operate the pressure bench injector wheel at low pressures.

The sample pressure is observed indirectly on the Heise gauges during the filling operation. When the pressure approaches the vapor pressure of the control temperature, switch the temperature control to

the manual mode. For most operating temperatures, the heaters should be shut off completely as the vapor condenses in the cell. The heat of condensation usually warms the cell assembly well above the control temperature. If the temperature rises too much, the liquid in the cell will evaporate and the pressure will rise rapidly. The oil pressure must then be increased to maintain the pressure balance across the diaphragm. When the pressure has stabilized and the major temperature fluctuations subsided, automatic temperature control can be resumed. The hardest part is now over!

The final sample pressure can be established by bleeding in more sample and balancing the diaphragm with the oil pressure. If the pressure in the sample supply cylinder is too low, isolate the cell system and condense sample into the loading bomb with a Dewar of liquid nitrogen placed around the bomb. The pressure in the filling line can then be brought to the desired value by lowering the Dewar by the right amount. The heat lag in the loading bomb is so large that the pressure changes quite slowly and may be closely controlled. The pressure should be increased to well above the current sample pressure before the filling process is resumed. Several condensations and fillings may be necessary before the final control pressure is reached.

8. Connecting the Pressure Balance

When the sample pressure is near, but still less than, the final control pressure, the pressure balance may be connected to the oil system. Extreme caution should be exercised during this operation. It is very easy to open the wrong valve or forget to open the right one.

First, isolate the pressure bench from the Heise gauges and oil line to the diaphragm; the Heise gauges should be left connected to the diaphragm to monitor the sample pressure. Then release the oil pressure in the bench, close the release valve, and repressurize the bench (with the valve to the pressure balance open) until the cylinder rotates freely. Add the appropriate weights to the balance, and then engage the belt and pulley system when the weights are rotating at the proper speed. Inject oil into the bench until the indicator on the pressure balance is above the zero mark.

Now check the pressure established on the pressure balance. First, close the valve between the Heise gauges and the oil line to the diaphragm. Keep the pressure constant while closing the valve by simultaneously opening another one which is already open in the system; note the sample pressure. When the diaphragm oil line is isolated, carefully connect the Heise gauges to the pressure bench and pressure balance. The pressure on the balance should read slightly higher on the Heise gauges than the sample pressure did. If it does not, close the valve to the pressure balance, adjust the pressure bench pressure to the sample pressure, and reopen the line to the diaphragm. Then adjust the sample pressure until it is slightly lower than the pressure of the balance as it was observed on the Heise gauges. When the adjustment is finished, the pressure balance may be connected to the system.

The oil side of the diaphragm will now be maintained at the constant pressure established on the pressure balance. Bleed in sample gas until the gas and oil pressures are balanced. If thermal steady state

has not yet been established in the liquid region of the sample, more gas must be continuously bled into the system. When steady state is approached, the bleed valve may be closed and the sample pressure adjusted manually with the trimmer injector.

9. Equipment Maintenance During the Diffraction Scans

After the sample pressure and temperature have been established, the cell plus sample check point intensities are measured and the diffraction scans begun. Several pieces of the control equipment require periodic attention during the runs. The time intervals between the checks will depend on the sample control conditions.

If the platinum resistance thermometer is being used as a temperature control element with the potentiometer as a reference voltage, the thermometer current should be checked, and the potentiometer should be standardized regularly. The current is determined by measuring the potential across the ten-ohm standard resistor in the thermometer circuit. In order not to disturb the temperature control, the potential should be measured with a potentiometer different from the one used as reference voltage. As the current changes, the reference voltage on the potentiometer must be correspondingly changed to maintain the same control temperature. To do this, first turn the switch on the linear amplifier from Recorder to Linear. Then note the control current, switch the Series 60 controller from automatic to manual control, and set the current at the correct value. Next, release the engagement button on the potentiometer, adjust the potentiometer to the desired setting, and depress and lock the button. Finally, switch the control knob on the

linear amplifier back from Linear to Recorder, and observe the recorder deflection from the control point. If this series of operations has been performed quickly, the temperature will not have changed much and the automatic control can be resumed immediately. If the temperature has drifted considerably, the current must be controlled manually until the control temperature is once again reached. The potentiometer setting should not be changed by more than two or three microvolts at a time without reestablishing automatic control. The same procedure is used to standardize the potentiometer.

Atmospheric pressure should be measured regularly, and the appropriate corrections should be made to the weights on the pressure balance. Small weights may be added to or removed from the weight pan without seriously disturbing the pressure control. Oil must be injected into the system regularly to keep the indicator near the proper zero mark. The Heise gauges and oil line to the diaphragm must be temporarily isolated while injecting oil into the system.

The coolant supply Dewar must be replenished regularly; the length of time a Dewar will last depends on the Dewar size and the rate of coolant consumption. The Dewar must not be allowed to become completely empty before changing over to another Dewar, especially when sample is in the cell at high pressure. As noted earlier, the sample pressure changes markedly with temperature in this closed system. Therefore, in order to maintain a positive pressure on the oil side of the diaphragm at all times, the control point temperature should not be exceeded. The most satisfactory way to accomplish this is to turn off the control

heaters just prior to exchanging the Dewars. The cell assembly is then allowed to cool several degrees. Then the rise in sample temperature caused by the interrupted coolant flow during the Dewar exchange will not be sufficient to exceed the control temperature.

When the coolant flow has been reestablished, the heaters may be switched on again and temperature and pressure control assumed. After the gas pressure in the Dewar is released, the Dewar can be removed and replaced by a full one in less than one minute. Since automatic temperature control is interrupted during this operation, x-ray data can not be taken. The total lapsed time between heater shutoff and resumption of steady control can be kept to less than five minutes.

10. Evacuating the Cell at the End of a Run

After the diffraction scans are completed and the cell plus sample check point intensities are measured, the sample is unloaded from the cell. First, close the valve to the pressure balance; the oil pressure is then controlled manually with the injector. A small amount of sample in the filling line is condensed in the sample loading bomb until the pressure falls to a low value. The pressure should be kept above atmospheric pressure at this time, however, to avoid any possible contamination by leaks into the system.

The sample is then bled out of the cell through the valve on the pressure manifold. The oil pressure, of course, must be reduced simultaneously. As the condensation pressure is approached, switch the temperature control to the manual method of control; and control at a temperature slightly lower than the control temperature.

When atmospheric pressure is reached, distill the remaining sample into the sample loading bomb and evacuate the cell. The pressure in the filling line should be brought quickly to its storage pressure to avoid sample contamination.

Now resume automatic temperature control with the control thermocouple circuits. When the control temperature is reached, the empty cell check point intensities are measured. And the run is completed.

11. Maintaining the Equipment Between Experimental Runs

Two procedures are available for maintaining the equipment between experimental runs. If the vacuum system is leak tight and no noticeable condensable vapors have accumulated on the aluminized Mylar radiation shield, the system may be left at low temperatures between runs. This procedure is most advantageous because it avoids any temperature cycling effects on any of the pressure seals and considerably shortens the initial cooling time for the next run. At the end of the diffraction scans, the temperature control circuits are turned off, and the coolant flow rate is set to maintain the desired temperature. If the temperature is sufficiently low, the only pumping needed is supplied by the ion pump.

If the cell assembly must be warmed to room temperature to pump out accumulated condensable vapors, the rough pumping line should first be connected to the chamber. The ion pump can then be shut off, and the coolant supply heater turned off. After disconnecting the coolant transfer tube, pass dry nitrogen gas through the coolant tubes until the

system has warmed to room temperature. This procedure prevents the accumulation of condensation in the coolant tubes which would later be very difficult to dry out.

APPENDIX III

METHODS FOR INCREASING THE PRESSURE TRANSDUCER
SENSITIVITY

The sensitivity of the pressure transducer may be increased without altering the physical dimensions of the diaphragm or re-machining any of the present components of the diaphragm assembly. The principal improvement would only increase the observable sensitivity by utilizing more of the relatively high output of the distance detector electronics. An actual increase in sensitivity can be gained by repositioning the distance detector. The details of these two methods are described below.

With the output resistance of the distance detector circuit at one megohm, the full travel of the diaphragm currently provides an output signal varying from six to fifteen volts over the full diaphragm movement. The diaphragm travel is approximately 0.010 in. in moving from the gas to the oil backing plate. A voltage divider is incorporated in the external circuit to reduce the output to the millivolt range for continuous display on a 0-10 millivolt recorder. The D. C. signal is opposed with a six-millivolt reference voltage to permit observation of the full diaphragm travel on the recorder table. Since the distance detector electronics has a null position output of 3.27 volts per psi, and the recorder scale can easily be read to 0.03 millivolts, the present null position of the diaphragm can be read to $0.03 \times 1000 / 3.27 \cong 0.01$ psi.

The observable sensitivity can be increased considerably by

using the relatively high output of the transducer more efficiently.
By opposing the null position output with a reference voltage of the
same magnitude, the observable diaphragm movement would be
limited only by the sensitivity of the voltage detector. For a ten-
volt null position output, a reference voltage of 9.995 volts will
permit a very small diaphragm displacement to be observed with
high sensitivity on the 0-10 millivolt recorder. With the present
diaphragm sensitivity, differential pressures of the order of 10^{-5}
psi could be detected. An additional factor of ten could be gained
by displaying the output on the 0-1 millivolt range of the Speedomax
G recorder.

The attainment of these observable sensitivities depends on
several conditions. The stability of the reference voltage and
electrical noise in the circuits would be the most serious limiting
factors. Also, the null position of the diaphragm would have to be
very reproducible for the transducer to perform its function properly.

A real gain in sensitivity can be achieved by repositioning the
distance detector more closely to the diaphragm. Figure 27 gives
the sensitivity curves of the distance detector. The detector is
currently positioned at 0.057 in. and operated at eight turns on the
potentiometer. The corresponding sensitivity is 460 volts per inch.
By moving the detector to 0.031 in. from the diaphragm, the distance
detector can be operated at zero potentiometer turns and approxi-
mately 1000 volts per inch sensitivity. The increase in sensitivity by
a factor of about two is gained at the expense of a shorter and less

linear operating range. The detector can be accurately and easily repositioned by changing the spacer thickness as described in Section III. C. 4 of the text.

APPENDIX IV

CALCULATION OF DIFFRACTOMETER ANGULAR RESOLUTION

The angular resolution of the diffractometer is given by the vertical and horizontal divergence[*] of the detected radiation. The maximum divergence is defined here as the largest difference between the nominal scattering angle, 2θ, and the diffraction angle of any detected ray.

The total vertical divergence is the sum of the divergences of the incident and scattered beams. For the scattering geometry of Figure 18, a ray scattered from one of the elements along the lower beam edge will have the maximum diffraction angle, and therefore the maximum divergence, of any of the detected rays. The geometry of the anode and divergence slit determine the position of that lower beam edge. The angle that a ray along this edge makes with a direct line from the center of the anode to the goniometer center line is the divergence of the incident beam. With horizontal slits of the type described in Section III. 4, the divergence of the scattered radiation is given by the arctangent of the plate spacing to length ratio. The parameters that were used to calculate the vertical divergence are given below:

---

[*]For convenience in description, the vertical and horizontal divergence are defined with respect to the physical geometry of Figure 15. This convention is opposite to that normally adopted in most textbooks.

Anode Width	0.0472 in.
Takeoff Angle	5.83°
Anode to Divergence Slit Distance	2.35 in.
Anode to Sample Distance	6.98 in.
Divergence Slit Width (1/6 degree slit)	0.0066 in.
Plate Spacing of Horizontal Soller Slits	0.005 in.
Plate Length of Horizontal Soller Slits	1.31 in.
Displacement of Incident Beam Below Goniometer Center Line	0.0096 in.

The incident and scattered beam divergences calculated from these parameters were 0.156 degrees and 0.219 degrees, respectively. The resulting total vertical divergence is therefore 0.375 degrees.

The horizontal divergence of the incident and scattered rays causes radiation to be detected from diffraction cones which have diffraction angles different from the nominal angle of observation, 2θ. The following formula,[*] similar to one given by Eastabrook,[67] was used to calculate the maximum diffraction angle:

$$\text{Maximum Diffraction Angle} = \cos^{-1}\left[\cos\alpha\,\cos\beta(\cos 2\theta - \tan\alpha\,\tan\beta)\right]$$

The angles α and β are horizontal divergences of the incident and scattered radiation, respectively; they are calculated from the parameters for the scattering geometry. The parameters for the

_____

[*]The formula and calculations for horizontal divergence were derived and performed by P. G. Mikolaj.

present geometry are

Plate Spacing of Vertical Soller Slits	0. 018 in.
Plate Length of Vertical Soller Slits	1. 250 in.
Sample to Receiving Slit Distance	5. 63 in.
Receiving Slit Height	0. 405 in.

From these parameters, $\alpha = 0.825$ degrees and $\beta = 4.13$ degrees. The horizontal divergence is the difference between the maximum diffraction angle and the scattering angle. A few of the calculated values are given below.

2θ	Horizontal Divergence
3. 0	2. 790
5. 0	2. 040
10. 0	1. 153
15. 0	0. 788
20. 0	0. 590
30. 0	0. 385
45. 0	0. 238
60. 0	0. 158
90. 0	0. 060
112. 59	0. 000
120. 0	-0. 020
135. 0	-0. 075
150. 0	-0. 148

PROPOSITION I

Proposition

Correction functions applied to x-ray diffraction data from fluids can be tested by a special application of the normalization conditions. The test can be performed without inverting the intensity data. If the functional form of the correction is known to be linear, an explicit expression for calculating the slope can be derived. This method avoids the trial and error selection of the slope by an iterative process.

Argument

Radial distribution analysis of x-ray diffraction data is beset with the problem of identifying the sources of error in the corrected intensity data and the Fourier transforms. Several methods are available[1] for identifying errors in the Fourier inverted intensity data. There is, however, no method for testing correction functions without inverting the data and checking for improvements in the distribution curves. The correction functions under consideration are those which are smoothly angular dependent. They may arise from incorrect application of absorption corrections or from systematic errors in the experiment.

One criterion for determining the validity of corrected and normalized intensities is that they must oscillate with ever diminishing amplitude about the scattering curve for independent particles. This is the basis on which the normalization constants are some-

times chosen. However, if the intensities are in error by a smoothly varying function, the normalization constant must be chosen at the point where the integral of the data is truncated; otherwise, normalization error will result. [2]

Erroneous data, then, may be treated as if it were incorrectly normalized except for a short section near the truncation limit. A correction function is sought which will properly normalize the data over its entire range.

Because of the strong oscillations of the sample intensities about the independent scattering curve, a graphical fit of the data is not helpful either in selecting or in testing a correction function. The integral method suggested by Krogh-Moe[3] and Norman[4] can, however, be adapted for these purposes. Let the true intensity curve, $I(S)$, be related to the observed sample intensity, $I_s(S)$, by a correction function, $B(S)$:

$$I(S) = [1 + B(S)] I_s(S) \tag{1}$$

When these true intensities are normalized by the integral method, the normalization constant is given by[*]

$$\frac{C}{N} = \frac{\int_0^{S_m} S^2 [f^2(S) + I^{inc}(S)] \, dS - 2\pi^2 \bar{\rho}_a}{\int_0^{S_m} S^2 [1 + B(S)][I_s(S) - I_o(S)] \, dS} \tag{2}$$

---

[*]The nomenclature is the same as that employed in the text of this thesis.

The normalization constant converges quickly to a constant value as the upper integration limit is increased. Rather than attempt to satisfy this condition by a trial and error selection of the correction function, consider an alternative procedure.

Except for a small error, the normalization constant calculated from equation (2) must agree with the constant given by the graphical procedure at large values of S. Designate this constant as the "true" normalization constant. Now the constant calculated by the integral method for the uncorrected data (for $B(S) = 0$) may be compared to the true constant by the ratio of the two integral method calculations. Rearranging the resulting expression yields an integral equation for the function $B(S)$:

$$\int_0^{S_m} S^2 B(S)[I_s(S) - I_o(S)] \, dS$$
$$= \left[\frac{C_{int}}{C_{true}} - 1\right]_{S_m} \int_0^{S_m} S^2 [I_s(S) - I_o(S)] \, dS \qquad (3)$$

Thus, if the true normalization constant can be estimated at only one value of S, and the integral method constant calculated for that same S value, the correction function can be obtained by solving this integral equation. The solution becomes particularly easy if the correction function is known to be linear in S. The slope is then given explicitly as

$$k = \left[\frac{C_{int}}{C_{true}} - 1\right]_{S_m} \frac{\int_0^{S_m} S^2 [I_s(S) - I_o(S)] \, dS}{\int_0^{S_m} S^3 [I_s(S) - I_o(S)] \, dS} \qquad (4)$$

without resort to satisfying equation (2) by trial and error methods. This simplification arises from the fact that the value of the constant at a particular point can be estimated much more accurately than the slope of the line through the point.

In practice, the integral method constant is quite different from the true value, even for quite small values of "k". Thus, even a fair estimate of C_{true} can provide a reasonable first guess of the slope. Since the ratio of the two integrals in equation (4) converges quite quickly, this method can be applied at relatively small values of S_m, where estimation of the slope is almost impossible. Other functional forms for $B(S)$ can be tested by application of equation (3). A catalogue of the behavior of C_{int}/C_{true} vs. S_m for various correction functions might be useful in identifying the type of error in improperly corrected data.

1. K. Furukawa, "The Radial Distribution Curves of Liquids by Diffraction Methods," Rep. Prog. Phys., <u>25</u>, 395 (1962).

2. H. H. Paalman and C. J. Pings, "Fourier Analysis of X-Ray Diffraction Data from Liquids," Rev. Mod. Phys., <u>35</u>, 389 (1963).

3. J. Krogh-Moe, "A Method for Converting Experimental X-Ray Intensities to an Absolute Scale," Acta. Cryst., <u>9</u>, 951 (1956).

4. N. Norman, "The Fourier Method for Converting Experimental X-Ray Intensities to an Absolute Scale," Acta. Cryst., <u>10</u>, 370 (1957).

PROPOSITION II

Proposition

Collimation of x-ray beams in both the horizontal and vertical planes can be accomplished with a single set of Soller slits by deliberately crimping each plate into a corrugated structure. The increased structural rigidity of the slits permits stacking them more closely together to achieve higher angular resolution. With this technique, thinner plate material can also be used to realize a higher degree of transmission than is presently obtainable.

Argument

Soller slits are conventionally used to collimate the incident and scattered x rays in spectrometers utilizing quantum detectors. The slits are employed in almost the same form as originally proposed by Soller in 1924.[1] A stack of thin metal plates spaced closely together divide the x-ray beam into a number of parallel slices. The plate length to spacing ratio is usually about thirty.[2] A typical arrangement employs one set of slits in the incident beam with plates parallel to the scattering plane to limit the horizontal divergence of the beam. Another set near the detector with plates normal to the scattering plane reduces the vertical divergence.

The limit to the angular resolution obtainable with Soller slits of a given length depends on how closely the plates may be spaced. The principal difficulty lies in keeping the plates parallel; they are so thin that they warp rather easily. Yet, their cross-sectional

area is relatively large so that when spaced closely together they block a sizeable portion of the incident x rays. A simple method for alleviating both these conditions is to crimp each plate into folds parallel to the x-ray beam path. Figure 1 shows a stack of crimped plates as viewed along the x-ray path. The corrugated shape of each plate gives it a much higher bending moment along its length; there will be little difficulty keeping the plate faces parallel to one another across the width of the beam. The plate spacing can therefore be considerably decreased. Also, the extra strength permits the use of thinner plate materials so that higher transmission can be obtained.

The main feature of these crimped Soller slits is that both horizontal and vertical collimation are effected in a single set of slits. Consider the plates shown in the figure. The rays of maximum divergence lie on planes almost parallel to the crimped faces of the plates. The horizontal and vertical components of these rays can be used to calculate the corresponding angular divergences of the slits. They are related to the design parameters of the slits in the following way.

The rays of maximum divergence are either of the "A" or "B" type shown in the figure. Their divergences depend on the design parameters listed below.

ζ = the crimping angle
v = half the peak to peak distance of the folds
d = the plate spacing
L = the plate length

The horizontal and vertical components for Case A are particularly easy to evaluate; they are

$$\text{Case A} \qquad X = v \qquad Y = d + v \tan \zeta$$

A straightforward application of trigonometric identities yields the components for Case B:

$$\text{Case B} \qquad X = v \left[1 + \frac{2d}{2v \tan \zeta - d} \right] \qquad Y = X \left[\tan \zeta - \frac{d}{v} \right]$$

When the plate separation, d, is small compared to $v \tan \zeta$, both cases approach the limiting form

$$X = v \qquad \text{and} \qquad Y = v \tan \zeta$$

The selection of the optimum design parameters depends on the particular application. For reducing the component of vertical divergence to a minimum, the crimping angle ζ should be made as small as possible consistent with the requirement that $d < v \tan \zeta$. This latter restriction is imposed to allow collimation in the horizontal plane.

The angular divergences calculated from the components of the rays of maximum divergence have a special meaning. Even though the minimum vertical component might be slightly larger than the plate spacing of conventional Soller slits, only a very small fraction of the scattered radiation is able to enter the slits along this oblique plane. The largest part of the detected radiation is collimated in the scattering plane by the vertical distance between

the plates.

The increased resolution and transmission of these slits can be most beneficially applied to x-ray intensity measurements on samples of low scattering power in the Debye-Scherrer geometry. The detector can be positioned much closer to the sample with the same ultimate angular resolution attainable with previous collimators. Since the scattered intensity decreases inversely with the sample to counter distance, the counting rates can be very favorably increased. Such an application not only permits higher accuracy in the intensity measurements (for a given counting time), it also increases considerably the signal to background noise ratio, an important advantage in any experiment.

1. W. Soller, "A New Precision X-Ray Spectrometer," Phys. Ref., 24, 158 (1924).

2. H. P. Klug and L. E. Alexander, X-Ray Diffraction Procedures (John Wiley and Sons, Inc., New York: 1954) p. 243.
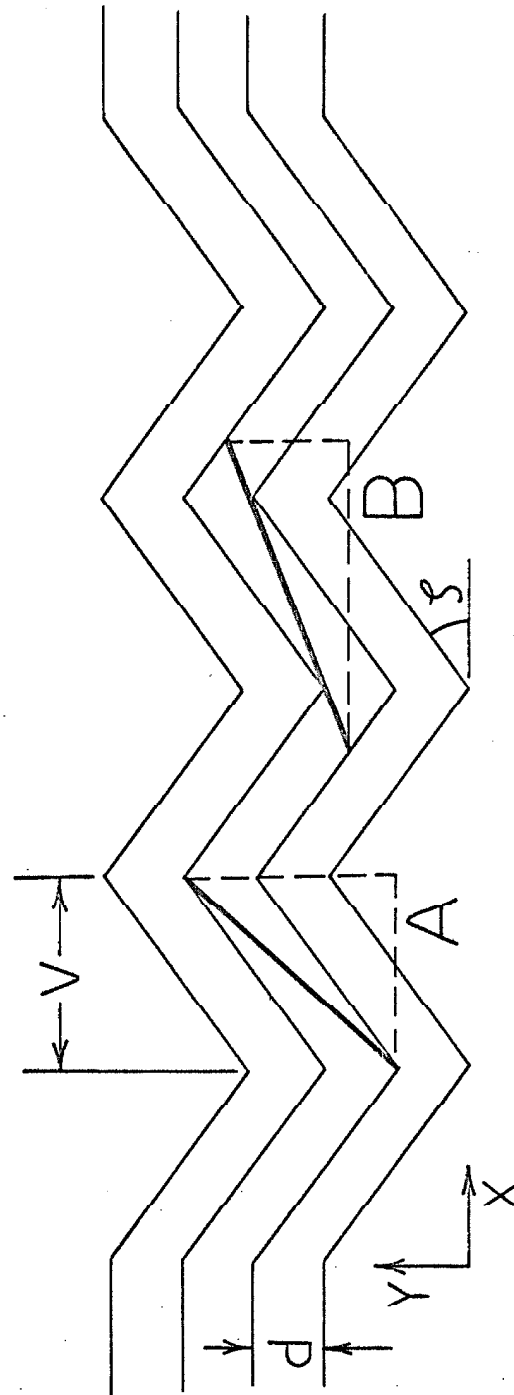
Figure 1. Design for Crimped Soller Slits

PROPOSITION III

Proposition

The thermodynamic work associated with the phenomenon of dielectrophoresis can be obtained from basic electrostatic theory. Simplification of the treatment for a cylindrical cell results in thermodynamic expressions of convenient form. For dilute solutions the concentration gradient is given as a function of the cell parameters. Although limited in applicability, this analysis should be useful in the design and operation of such a cell.

Argument

Uncharged particles of sizes large in comparison with atomic dimensions have been separated effectively from solution by the technique involving dielectrophoresis.[1, 2, 3] This phenomenon is defined as the motion of matter by polarization effects in non-uniform electric fields. A thermodynamic description of this effect can be made by obtaining an expression for the work associated with the introduction of a dielectric solution of variable concentration into a condenser.

The electrostatic work necessary to put isotropic solution of capacitivity $\epsilon(D)$ into a charged condenser is given by[4]

$$\Delta W = - \frac{1}{\epsilon_o} \int_v \int_0^D (1 - \frac{\epsilon_o}{\epsilon}) \vec{D} \cdot d\vec{D} \ dv \tag{1}$$

where v is the volume between the electrodes, $\vec{D}$ is the electric

displacement, and ϵ_o is the permittivity of free space. [*]

Consider now a condenser consisting of a pair of infinitely long, concentric cylinders, the inner carrying a charge Q per unit length and the outer carrying a charge -Q per unit length. The electric displacement, $\vec{D}$, of this system is directed radially outward and has the magnitude $Q/2\pi r$, where r is the distance from the central electrode.[5] If, now, we confine our attention to low fields (large r), the dielectric constant, $K \equiv \dfrac{\epsilon}{\epsilon_o}$, is a weak function of the electric displacement. The integration over D in equation (1) can then be performed directly. With D stated in terms of r, the result may be expressed in differential form as

$$dW = -\frac{Q^2}{4\pi\epsilon_o} \left(1 - \frac{1}{K}\right) d \ln r \qquad (2)$$

With the assumption that the condition of local equilibrium applies, equation (2) may be inserted into the first and second law expression for internal energy:

$$dE = T\, dS - P\, dV + \frac{Q^2}{4\pi\epsilon_o} \left(1 - \frac{1}{K}\right) d \ln r + \sum_i \mu_i\, dN_i \qquad (3)$$

The thermodynamic derivatives follow in a straightforward manner from the cross-differentiation identities and the definitions of the thermodynamic functions. Of particular qualitative interest is the derivative:

---

[*]The mks system of units is used in this discussion.

$$\left(\frac{\partial S}{\partial \ln r}\right)_{T, P, N} = -\frac{Q^2}{4\pi\epsilon_o K^2}\left(\frac{\partial K}{\partial T}\right)_{P, r, N} \tag{4}$$

This expression states that if K decreases with increasing T (as it does for most substances), the entropy decreases with decreasing r (increasing field strength). This agrees with the expectation that the stronger field will reduce the randomness of molecular orientation by more effectively polarizing the solution.

For a two-component system, the concentration gradient can be obtained by considering the chemical potential gradient at constant temperature, pressure, and total composition:

$$\left(\frac{\partial \mu_2}{\partial \ln r}\right)_{T, P, N} = \frac{Q^2}{4\pi\epsilon_o K^2}\left(\frac{\partial K}{\partial N_2}\right)_{T, P, N} \tag{5}$$

Since the chemical potential of component two must be the same throughout the solution, it follows after introducing the appropriate expressions for mole fractions in a binary solution that

$$\frac{d \ln x_2}{d \ln r} = -\left(\frac{\partial \mu_2}{\partial \ln x_2}\right)_r^{-1} \frac{Q^2 x_1}{4\pi\epsilon_o N K^2}\left(\frac{\partial K}{\partial x_2}\right)_{T, P, N} \tag{6}$$

where x_2 is the mole fraction of the solute.

As an estimate of the chemical potential gradient, the solution is assumed dilute enough for application of Henry's Law. The final expression for the concentration gradient is then

$$\frac{d \ln x_2}{d \ln r} = - \frac{Q^2}{4\pi\epsilon_0} \frac{x_1}{NRT\ K^2} \left(\frac{\partial K}{\partial x_2}\right)_{T,P,N} \tag{7}$$

This equation gives the concentration gradient as a function of the radial position in the cylindrical cell. It is only applicable in weak fields where the dielectric constant is not a function of the field strength. Also, it is limited to regions where the solution is dilute. However, both of these conditions are approached near the outer boundary of the cell. If the thermodynamic and electrostatic properties of the solution are known in this region, the concentration gradient can be determined. There are, of course, other effects occurring in the cell which have been neglected in this treatment (e. g., conduction, thermal convection, diffusion, and dipole interaction). This expression, however, should be useful in the design and analysis of experimental cells.

1. Pohl, H. A., "Some Effects of Nonuniform Fields on Dielectrics, " J. Appl. Phys. 29, 1182 (1958).

2. Debye, P., Debye, P. P., Eckstein, B. H., Barber, W. A., and Arquette, G. J., "Experiments on Polymer Solutions in Inhomogeneous Electric Fields, " J. Chem. Phys., 22, 152 (1954).

3. Pohl, H. A. and Schwab, J. P., "Factors Affecting Separations of Suspensions in Nonuniform Electric Fields, " J. Appl. Phys., 30, 69 (1959).

4. Lewis, G. N. and Randall, M., revised by K. S. Pitzer and L. Brewster, Thermodyanamics (New York: McGraw-Hill, 1961), p. 499.

5. Smythe, W. R., Static and Dynamic Electricity, (New York: McGraw-Hill, 1950). p. 28.

PROPOSITION IV

Proposition

Many experiments require the use of a thin membrane to separate fluids at the same or different pressures. Since the permeability of the membrane is usually a function of the *stresses* on it, it would be very desirable to be able to reproduce the stresses involved in making the seal. An O-ring in a beveled groove can effect the seal reproducibly. An approximate treatment of the forces involved in the seal can be made by decomposing a free body section of the O-ring into two equilibrium systems.

Argument

A groove of the type proposed is shown schematically in Figure 1. Treatment of the forces in such a system may be simplified by considering the O-ring as an incompressible torus which may, however, be stretched in an axial direction; it is further assumed that there is no change in cross sectional area of the O-ring upon extension. These approximations will be most applicable for O-rings of cross-sectional diameter small in comparison with their circumference.

A free body diagram of a unit length of the torus in tension is shown in Figure 2a. The forces shown are W, the force due to gravity; P_N, the force applied by a closure lid on the membrane; P_F, the frictional force of the membrane on the O-ring; S, the restoring force on the O-ring due to circumferential "hoop" stress;

and R, the reactive force. A force equal in magnitude and opposite in direction to P_F provides the radial stress on the membrane.

According to the "Theorem of Three Forces,"[1] the three resultant forces acting at A, O, and B must intersect in one point, this being point B.

For convenience in analysis, the force system is regarded as the superposition of two equilibrium systems, the forces due to hoop stresses (S, P_S, and R_S in Figure 2b) and those due to the applied force P_N and gravity force W (P_N, P_R and W in Figure 2c).

The work done during circumferential extension of the O-ring will be transformed into potential energy of strain. Assuming a simple linear relationship between stress and strain,* the force S may be shown[2] to be

$$S = AE\frac{2\pi Z \cot \alpha}{2\pi r_o^2} = \frac{AEZ \cot \alpha}{r_o^2}$$

where E is Young's modulus; A the cross sectional area of the torus; $2\pi r_o$ the initial circumferential length of the O-ring of radius r_o before extension; and $2\pi Z \cot \alpha$ the total elongation in terms of the Z displacement of the O-ring, i.e., in a direction parallel to P_N. Then, since $P_S = R_S \cos \alpha$, we may solve for P_S from a force balance on Figure 2b.

---

*At best this is only approximately true for most materials within certain stress limits. The appropriate stress-strain functional relationship must be used for those materials not obeying Hooke's Law.

$$P_S = \frac{EAZ \cot \alpha}{r_o^2} \left(\frac{\cos \alpha}{1 + \cos \alpha} \right)$$

The forces in Figure 2c may all be determined by specifying the values of α, P_N, and W. Thus, from a superposition of the two systems, we see that the entire system of forces is a function of the O-ring parameters E, A, r_o, and W; the operating parameters P_N and Z; and the design parameter α.

Restrictions must be imposed upon the stipulation of the aforementioned parameters to insure that the O-ring will not slip against either surface. Referring to Figure 2a, the following relations must be satisfied:

$$\tan \frac{\alpha}{2} < \mu_A$$

$$\tan \beta < \mu_B$$

where μ_A and μ_B are the coefficients of static friction of the O-ring against the membrane and groove surface, respectively.

It has been shown that an initial stress on a membrane vacuum seal may be effected by a beveled O-ring groove. The force parameters have been determined by approximate theoretical treatment. For systems deviating strongly from the stated assumptions, the details of the treatment cannot be expected to be valid.

1. Timoshenko, S. and Young, D. H., Engineering Mechanics (New York: McGraw-Hill, 1956), p. 32.

2. Timoshenko, S. and MacCullough, G. H., Elements of Strength of Materials (Princeton: D. VanNostrand Co., Inc., 1949), p. 27.
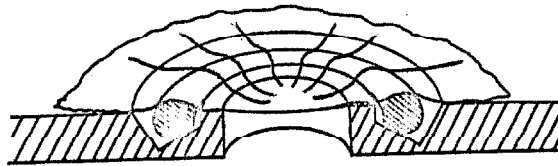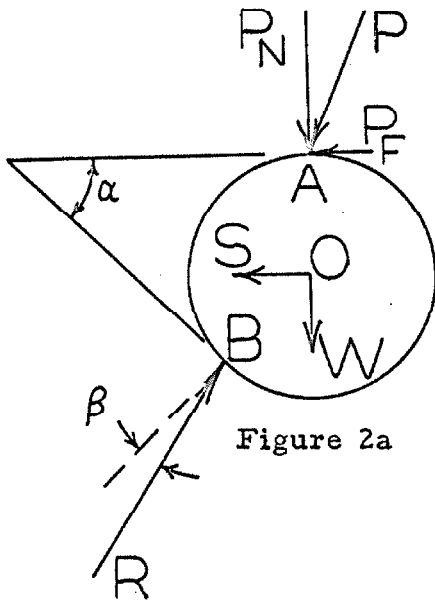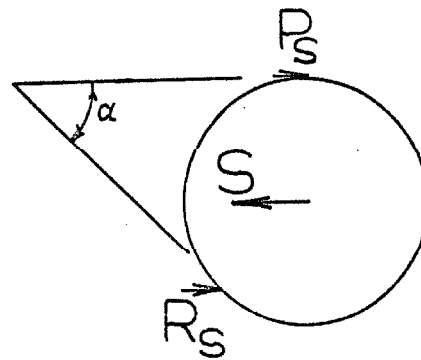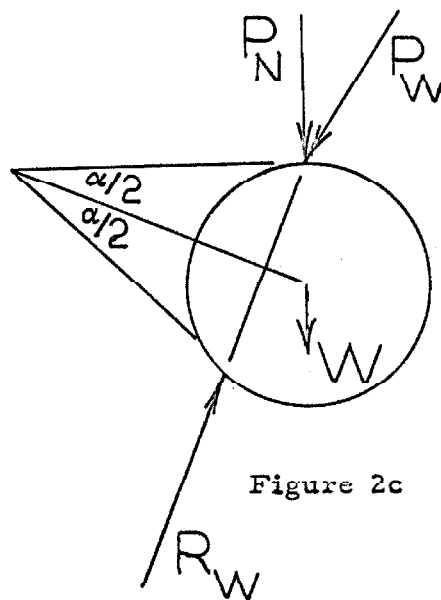
Figure 1

Figure 2a

Figure 2b

Figure 2c

PROPOSITION V

Proposition

An estimate of the relative probabilities of evaporation and surface diffusion for an ideal lattice gas can be made by comparing the residence times for the two competing processes. The extension of the approach to more sophisticated models would be useful in obtaining a semi-quantitative description of the role which the two processes play in heterogeneous catalysis.

Argument

The roles that surface diffusion and evaporation play in heterogeneous catalysis are not well understood. Some insight into their relative importance can be obtained by considering a monolayer of gas molecules adsorbed on a solid surface.

At sufficiently high temperatures, the adsorbed molecules will be completely mobile on the surface of the solid. By reducing collision space from three to two dimensions, the solid surface promotes the likelihood of chemical reaction. However, as the temperature is lowered, the transition from mobile to localized adsorption occurs. Somewhere between the extremes of completely mobile and completely localized adsorption, the presence of the solid surface as a promoting agent for chemical reaction ceases. This would occur when the gas is quite localized. The rate of diffusion with respect to evaporation provides a useful frame of

reference for describing the behavior of the gas. The relative rates provide a measure of the effectiveness of the solid surface in promoting chemical reaction.

An estimation of the relative rates of surface diffusion and evaporation can be obtained by application of an ultra-simplified model to the adsorbed monolayer. The model under consideration is an ideal lattice gas[1] at sufficiently low temperatures that the adsorbed molecules only occasionally escape from the potential wells which form the adsorption sites.

The Eyring rate theory[2] can be used to calculate an average residence time which the adsorbed molecule spends at a site before passing over the potential barrier to an adjacent site. For simplicity, consider a dilute monatomic gas adsorbed on a square lattice of sites. Within the assumptions of the theory, the residence time for surface diffusion, t_{sd}, will be given by[3]

$$\frac{1}{t_{sd}} = 2\nu_x e^{-V_o/kT} \tag{1}$$

where ν_x is the vibrational frequency in the "reaction coordinate" (direction of diffusion) and V_o is the height of the potential barrier above the minima of the potential wells. In the harmonic oscillator approximation, the vibrational frequency can be expressed in terms of V_o by estimating the shape of the minima in the potential surface. By representing the surface as a periodic function in the nearest-neighbor distances, the frequency can be calculated and inserted into equation (1) with the result:

$$t_{sd} = \left[\frac{ma^2}{2V_o}\right]^{1/2} \exp\left[V_o/kT\right] \qquad (2)$$

where m is the atomic mass and a is the nearest-neighbor

distance. Thus, if the height of the potential barrier can be esti-

mated--the quantum mechanical calculations are extremely com-

plicated--the residence time can be evaluated.

The residence time for desorption can be obtained by a

similar application of the rate theory. However, a more convenient

expression can be obtained in terms of the surface concentration,

N/A, and the gas phase pressure, P:

$$t_{ev} = \frac{(2\pi mkT)^{1/2}}{P} \; N/A \qquad (3)$$

All the quantities on the right side of the equation can be evaluated

experimentally for adsorption processes which can be represented

by Langmuir adsorption isotherms (derived from ideal lattice

gas theory).

A direct comparison of the two residence times for surface

diffusion and evaporation requires that the two competing processes

are completely independent. In other words, a single molecule

does not have the alternative of either desorbing or diffusing to an

adjacent site. The comparison applies to the bulk population of

adsorbed molecules, some of which are evaporating and others

diffusing. Those participating in diffusion are counted as part of

the equilibrium concentration of adsorbed molecules from the point

of view of evaporation.

An informative calculation can be made for argon gas adsorbed on carbon. The results of Chackett and Tuck[4] for argon at 0.01 mm Hg adsorbed on charcoal at 90° K indicate a surface concentration of 1.7×10^{15} atoms/square meter. These conditions give a residence time for evaporation of[*]

$$t_{ev} = 2.9 \times 10^{-8} \text{ seconds}$$

In order to calculate the residence time for surface diffusion, an estimation of the potential barrier height, V_o, has to be made. With the Van der Waals forces making up the potential surface, the barrier is of the order of 500 calories per mole. The vibrational frequencies calculated using this value are 4.5×10^{11} seconds^{-1}; the resulting residence time for surface diffusion is

$$t_{sd} = 1.8 \times 10^{-11} \text{ seconds}$$

If we assume that the probability of occurrence of either desorption or surface diffusion is inversely proportional to the corresponding residence time, the comparison states that for argon adsorbed on carbon at 90° K at a gas pressure of 0.01 mm Hg, the probability for diffusion is 1600 times the probability for evaporation.

Application of experimental data to such a simplified model cannot be expected to provide useful quantitative information. However, this simple calculation affords a little insight into the behavior

---

[*]The assumption of a square lattice does not apply to the carbon structure, of course. The effect on the calculation can be at most a factor of three.

of the adsorbed gas molecules. The general approach could be

extended to other simple systems if suitable estimates of V_o

can be obtained. The application of a more sophisticated adsorption

model would be useful in attempting an understanding of the roles

of evaporation and surface diffusion in chemical reactions on

solid surfaces.

1. T. L. Hill, An Introduction to Statistical Thermodynamics
      (Addison-Wesley, London: 1960), p. 124.

2. S. Glasstone, K. J. Laidler, and H. Eyring, The Theory of Rate
      Processes (McGraw-Hill, New York: 1941).

3. Hill, ibid., p. 199.

4. K. F. Chackett and D. G. Tuck, "The Heat of Adsorption of the
      Inert Gases on Charcoal at Low Pressures," Trans.
      Faraday Soc., 53, 1652 (1957).